LARGE-SCALE MOLECULAR DYNAMICS INVESTIGATIONS OF ION-INDUCED COMPOSITIONAL DYNAMICS LEADING TO NANOPATTERN FORMATION AT SEMICONDUCTOR SURFACES

BY

MICHAEL AARON LIVELY

THESIS

Submitted in partial fulfillment of the requirements
for the degree of Master of Science in Nuclear, Plasma, and Radiological Engineering
in the Graduate College of the
University of Illinois at Urbana-Champaign, 2017

Urbana, Illinois

Master's Committee:

Associate Professor Jean Paul Allain, Adviser
Assistant Professor Yang Zhang

ABSTRACT

Ion beam nanopatterning has been demonstrated to be a versatile method for obtaining a wide variety of surface features on a broad range of materials, with structures such as ripples, quantum dots, terraces, and ordered holes being obtained for various experimental conditions. However, theoretical modeling is well behind the experimental progress, and even for "simple" systems such as noble gas ion irradiation of silicon surfaces there exist several competing models proposing different pattern-forming mechanisms. For more complex systems, such as ion irradiation of binary alloys, the landscape of potential pattern-forming mechanisms remains very much a *terra incognita*, to the point where two models can predict the same surface morphologies while predicting diametrically-opposed surface compositional profiles.

This knowledge chasm between experiments and theories requires a fundamental understanding of the ion-induced mechanisms that can lead to surface instabilities, to eliminate the dependence on simplifying assumptions and tunable parameters of existing modeling approaches. To close this gap, atomistic computational modeling is needed to allow direct observation of the ion-surface interactions at smaller length and time scales than can be accessed by experimental characterization techniques. At the same time, atomistic simulations must be able to account for changes over time in the surface structure or composition, which will influence the nature of the ion-surface interactions. The results from these atomistic simulations and the physical understanding gained can then be used as the basis for or as parametric inputs to multiscale models of nanopattern formation. Such a model has previously been developed, which is a hybrid molecular dynamics/kinetic Monte Carlo (MD/kMC) atomistic simulation that uses so-called "crater functions" obtained from MD simulations of single-ion impacts, combined with an atomistic kMC model of surface diffusion, to provide a complete description of the ion-surface interaction and the

resulting surface nanopatterning without reliance on the assumptions and arbitrary parameters from other models. This simple computational model provides a well-tested starting point from which additional mechanisms can be implemented and used to study more complex material systems. Here, large-scale MD simulations are used to study the ion-induced compositional and phase dynamics, enabling the mechanisms that can cause patterning instabilities to be elucidated and characterized.

The compositional evolution of GaSb under low-energy ion irradiation is studied by massive-scale MD simulations, which have been carried out on the Blue Waters high-performance computing platform at the University of Illinois. The first set of simulations consist of 500 eV Kr^+ bombardment of a GaSb surface with a significantly-altered compositional profile designed to resemble experimental observations of the compositional depth profile at the onset of nanopattern formation. In regions of altered composition, thermodynamic phase separation is observed as the surface atoms rearrange themselves into clusters of the enriched component within 50/50 amorphous GaSb. Additionally, the pure Sb clusters in Sb-enriched regions self-organize into crystalline lattices, while the pure Ga clusters in Ga-enriched regions remain in an amorphous state. These results have demonstrated for the first time, using MD simulations, that the compositional depth variation observed from experiments can lead to a *lateral* compositional variation that may provide a potential pattern-forming instability. The second set of simulations consist of 500 eV ion irradiation of initially-pristine GaSb(110) by Ne^+, Ar^+, and Kr^+ ion species up to the experimentally-relevant fluence of 7.5×10^{15} cm^{-2} with the goal of discovering how the ion-induced mechanisms leading to the formation of a compositional depth profile. While the surface quickly becomes amorphous under sustained ion bombardment, no ion species led to the emergence of a compositional depth profile. However, smaller "protoclusters" of Sb were formed in the subsurface, even in the absence of the compositional change necessary to drive thermodynamic phase separation. These protoclusters are conjectured to be formed from Sb precipitation out of the GaSb

melt volume from ion-induced thermal spikes, and may function as the initial "seeds" that grow large enough to cause a compositional depth profile to form under the influence of additional mechanisms acting on timescales beyond the limits of MD simulations.

The effects of implanted noble gas ions in Si are also studied with the use of high-fluence molecular dynamics simulations to reach cumulative ion fluences of $\geq 3 \times 10^{15}$ cm^{-2}. Ion species of Ne^{+}, Ar^{+}, Kr^{+}, and Xe^{+} were studied with incident energies per ion ranging from 20 to 1000 eV and ion incidence angles ranging from 0° to 85°. The implanted ions tend to form clusters beneath the surface, which are formed purely by the kinetic motion of the ions and not due to diffusive processes. A cluster degassing mechanism is observed, which occurs when the Si surface above a cluster is eroded by ion sputtering and the gas atoms rapidly vacate the cluster. Immediately after the cluster has degassed, a rapid inflow of mass from the surrounding surface occurs to fill the resulting void. The combination of the cluster degassing and the resulting mass flow has a highly disruptive effect on the local surface morphology, which could destroy nanopattern "seeds" at the surface, which may be a missing mechanism from existing models of surface nanopatterning that can correct the quantitative inaccuracies of those models. Additionally, the shear stress distribution and elastic modulus were calculated for the ion-bombarded surfaces. While the shear stress distribution is in general agreement with expectation from previous computational studies, the strong variance in the stress depth profiles at different fluences suggests a highly-localized contribution from the implanted ion clusters which must be considered in stress-based models of ion beam nanopatterning. Comparing the elastic moduli for surfaces with and without ion clusters confirms that the presence of clusters within the surface has a significant influence on the mechanical properties of that surface.

TABLE OF CONTENTS

Chapter 1: Introduction

Canonically, the first direct observation of ion beam-induced nanopattern formation on a surface is attributed to Navez and coworkers in 1962 [1], although observations of characteristic grooves had been made previously [2]. Regardless of which authors claim the discovery, ion beam nanopatterning has seen widespread application in the intervening half-century, with periodic ripples, holes, dots, and other structures being obtained on metals, semiconductors, insulators, and amorphous surfaces [3]. Of particular technological relevance was the discovery of hexagonally-ordered quantum dot formation by ion beams at the surface of compound III-V semiconductors such as GaSb [4]. Not too long afterwards, it was established that similar quantum dots could be formed at Si surfaces with the additional co-deposition of metallic impurities [5], clarifying a number of discrepancies in experimental literature.

The modern era of ion beam nanopatterning is one of rather disparate progress between the wide range of experimental discoveries and the comparatively-limited ability of theories to explain any of those phenomena. Even for the "simple" or "representative" case of silicon bombarded by noble-gas ions, uncertainty still exists as to what fundamental mechanisms drive the nanopattern formation (to say nothing of the nonlinear evolution of those patterns at high beam fluences!). Predictably, the situation is no better for the cases of compositionally-complex systems where phase formation or separation can complicate the picture considerably. A key factor in the inability to develop comprehensive, predictive models is the large lack of characterization, by experimental or computational means, of surface morphological and compositional processes *in-situ* while nanopatterns evolve. In lieu of such information about driving physical mechanisms, modeling efforts instead rely on *a priori* assumptions – leading to mildly-humorous situations where two models based on distinct-opposite mechanisms [6,7] predict identical morphological evolutions with diametrically-opposed lateral compositional profiles!

The work presented in this thesis aims to address this knowledge gap by using atomistic simulation tools to elucidate fundamental ion-induced and ion-driven physics which can lead to compositional and morphological evolution of complex surfaces at the nanoscale. By addressing key hypotheses about the nature of the ion-surface interaction, this work will form the basis for computational and theoretical multiscale models addressing the formation and evolution of nanopatterns on ion-bombarded surfaces. Ultimately, by not only identifying driving mechanisms but by further functionalizing these with respect to *tunable experimental parameters*, the models developed will have the predictive power necessary to demonstrate relevance to the diverse experimental landscape of the field today.

1.1 Theoretical approaches to ion beam nanopatterning

The best-known model for ion beam-induced nanopattern formation is that of Bradley and Harper [8], which is still used even in current publications [9]. The basis of the model is the theory of ion-induced sputtering developed by Sigmund [10]. Bradley and Harper showed that this description of the sputtering leads to a curvature-dependent sputter yield which is greater at troughs (positive curvature) and lesser at crests (negative curvature), providing a pattern-forming instability for all angles of ion beam incidence as shown in **Figure 1.1**. With the inclusion of a fourth-order surface diffusion term, the complete Bradley-Harper description of the surface morphological evolution is

$$\frac{\partial h}{\partial t} = -v_0(\theta) + v_0'(\theta)\frac{\partial h}{\partial x} + \Gamma_1(\theta)\frac{\partial^2 h}{\partial x^2} + \Gamma_2(\theta)\frac{\partial^2 h}{\partial y^2} - B\nabla^2\nabla^2 h \qquad (1.1)$$

where, for an ion beam incident in the xz-plane: v_0 is the erosion rate (i.e. sputter yield) for a flat surface, v_0' captures the slope-dependence of the sputtering yield, Γ_1 and Γ_2 are the curvature coefficients derived from Sigmund's model, and B is a surface smoothening coefficient which was taken by Bradley and Harper to describe the activated surface diffusion of Mullins [11]. The surface is always destabilized under ion beam irradiation; thus, periodic ripples will appear on the surface with a wavevector oriented in the same direction as the most-negative curvature coefficient.

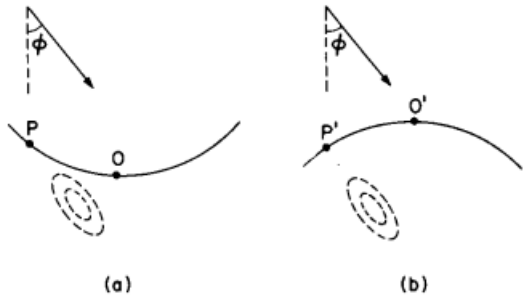

Figure 1.1: Schematic illustrating the Bradley-Harper mechanism [8]. For an ion impact at a point *P* located between a crest and a trough, the energy deposition is proportionally greater at the trough than at the crest, leading to greater sputtering from the trough and thus a pattern-forming surface instability.

While initially successful, the Bradley-Harper model suffers from several weaknesses, with the most fundamental of these being the assumption that ion-induced sputtering is the only active mechanism determining the surface instability. However, surfaces may remain or become flat under ion bombardment for some conditions, indicating that other mechanisms must be considered since the Bradley-Harper model cannot predict a flat, stable surface. To address this, Carter and Vishnyakov introduced a model [12] which included the ion-induced ballistic redistribution of mass along the surface, and showed that this contributed a stabilizing effect for small incidence angles which could dominate the Bradley-Harper instability and lead to flat surfaces under ion irradiation. The development of the "crater function" concept [13–15] eliminated the need to separate these effects by incorporating, in theory, a complete description of a single-ion impact on the target surface. This approach was applied (in conjunction with computational results described

in the following section) by Norris and coworkers [16] to not only describe ion beam nanopatterning of Si but also to identify *post-facto* which mechanisms were predominant in determining the surface morphology.

Not predicted by any model was the discovery of ordered quantum dot formation by normal-incidence ion beam irradiation, first on GaSb [4] and other III-V compound semiconductor surfaces, and later on silicon surfaces [17]. Initial explanations failed to account for any compositionally-dependent mechanisms [18,19], likely due to the discovery of patterns on "pure" Si suggesting a non-compositional effect. This was shown not to be the case, as Ozaydin and coworkers demonstrated that dot formation on Si only occurred in the presence of metallic impurities, which had previously been co-deposited with the ion beam inadvertently [5].

This of course brought to the forefront a very difficult question – what compositional mechanisms drive nanopatterning? This question has yet to receive a satisfactory answer, as theoretical models have presented numerous ideas with no clear consensus. Proposed compositional mechanisms have included: kinetic alloy decomposition [20], preferential redistribution [6,21,22], sputter shielding [23], Gibbsian phase segregation [7], preferential sputtering [24], impurity-induced surface stresses [25], compound formation [26], disparate ion-enhanced species diffusivities [27], and compositional alteration of the collision cascade [28].

To illustrate the difficulty of the problem, **Figure 1.2** shows a comparison of the predicted compositional modulation between the models of Bradley and Shipman [6,21,22] and Norris [7]. While both models predict the same surface morphology, the surface compositional distribution is predicted oppositely in each model. While experimental investigations of the compositional evolution are ongoing [29,30], the ability to probe the lateral compositional profile has yet to be demonstrated, so that theoretical efforts thus far produce little more than open questions.

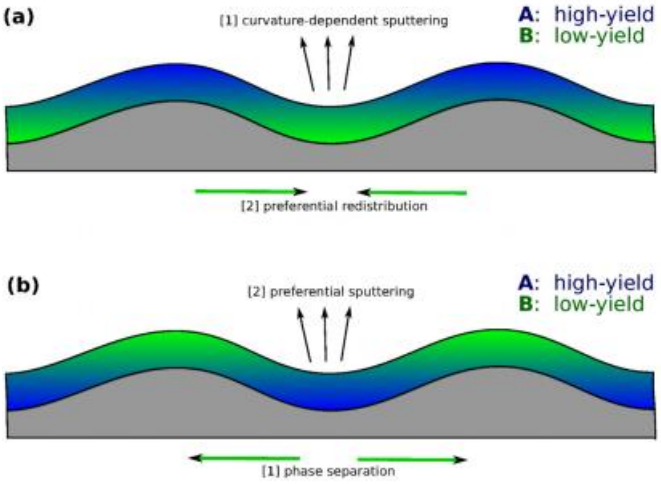

Figure 1.2: Comparative lateral compositional profiles from the models of Bradley and Shipman **(a)** and Norris **(b)** [7]. Both models predict the same type of surface morphology, but the predicted compositional distributions are diametric opposites.

More recently, a new class of so-called "hydrodynamic" models have been introduced which ascribe the surface evolution to stress-induced viscoelastic flow [31–33]. The development of these models has been motivated by experimental observations that ion-bombarded semiconductor surfaces form an amorphous layer [34,35], in which the combination of ion-induced stresses and viscosity reduction allow solid flow to occur. While these models still contain several flaws (including a continued reliance on tuned parameters [36]), this represents a significant step towards integration of experimental characterization with theoretical development.

The primary underlying weakness in nearly all of these models remains the reliance on *a priori* assumptions about the nature of the ion-surface interactions and their dominant contributions to nanopatterning. This is not to say that the models presented above are not physical, but rather that the physics of each model cannot be derived from direct experimental knowledge. Furthermore, it is difficult or impossible to relate the parameters of each model to experimental measurables, since the interaction between a single ion and the target (resulting in e.g. the distribution of deposited energy required by the Bradley-Harper model) occurs at time and length scales much smaller than

can be realized experimentally. Thus, the necessity exists for computational modeling which can connect atomistic physical mechanisms to the macroscopic surface evolution.

1.2 Computational modeling of ion-induced nanopatterning

Computational models have been used to study ion-surface interactions for more than three decades with varying amounts of success. The motivation for conducting these simulations is twofold: on one hand, the single-ion interactions with the surface are not accessible by experiments yet are necessary for theoretical development. Computational simulations are thus required to study these interactions. On the other hand, the development of fully-atomistic computational models reduces or eliminates the necessity for simplifying assumptions for the sake of analytical tractability.

1.2.1 Molecular dynamics investigations

Fundamentally, molecular dynamics (MD) is simply the numerical solution of Newton's laws of motion for a system of interacting particles, which interact according to one or more prescribed potentials [37]. While this approach allows for high physical accuracy, limited only by the correctness of the potential and the classical mechanics of the simulation, for large systems of interacting particles the computational requirements quickly become daunting. Thus, the earliest MD studies of ion-surface interactions were limited to single-ion impacts for fairly small cell sizes, while more recent advances in computational power have enabled increases in the size of the simulated spatial and temporal domains.

Within the single-impact paradigm of early MD studies, several mechanisms drew particular attention. In particular, much interest was devoted to understanding defect production during the collision cascade, particularly in silicon for which not only defect production but also

amorphization were topics of critical importance [38–40]. Besides this, much attention was also given to calculation and characterization of sputtering yields. From MD, the angular and energy distribution of sputtered particles could be collected and analyzed to assess the mechanisms by which particles were sputtered from a particular kind of impact [41]. On the other hand, early validation of MD simulations against experimental results relied on the sputtering yield as a point of comparison between the two approaches [42]. Within the limit of single-ion impacts, Rubio and coworkers were able to study the fluence dependence by constructing surfaces with various pre-existing concentrations of the ion species, finding that the sputtering yield would increase with fluence due to the influence of the implanted species [43].

In more recent years, MD studies have expanded to include the effects of *cumulative* ion bombardments, i.e. multiple successive ion impacts on the same surface cell. For these studies, silicon has been the critical material. Moore and coworkers studied low-energy Ar^+ implantation for cumulative ion fluences $<10^{15}$ cm^{-2}, claiming to have reached a steady-state ion concentration [44]. This study measured the implantation depth profile, the degree of surface damage and disordering, and the effect of the ion fluence on surface sputtering. However, the primary purpose of this work was to serve as a basis for following studies of surface mechanical properties by the same authors [45–47]. Tensile stress-strain testing was done with MD to determine the elastic modulus of the damaged surface as a function of depth and fluence. Additionally, the ion-induced compressive stresses in the surface were also measured and parameterized with respect to depth, ion fluence, and the implanted ion concentration. More recent MD measurements of the ion-induced structural modification and stress distribution in the surface have been carried out by a different set of authors in the context of the stress-induced viscoelastic flow models [33,48].

While Si is the most-studied of the semiconductor materials, ion irradiation of multicomponent systems such as III-V semiconductors has been studied with MD as well. However, in many cases the emphasis of these studies has been limited to defect production and its dependence on the composition [49–51] without considering how the ion impacts might change the surface composition in exchange. More recently, MD simulations of cumulative ion irradiation of III-V semiconductors have been conducted, and while the primary focus of this work was the sputtering behavior of the surface a compositional depth profile was observed due to preferential sputtering [52,53]. However, the compositional analysis in these studies remained very limited, and in particular no apparent effort was made to discern the potential existence of any lateral compositional variations.

Finally, in recent years it has become somewhat fashionable to carry out numerous simulations of individual ion impacts into the same initial surface, rather than carrying out cumulative bombardment of a single surface, and to then carry out statistical analysis of the changes induced in the surface by the single-ion impacts. These statistical results, which may include direct calculation of surface height profiles [14] or computation of statistical moments [16,54], are referred to as "crater functions". The use of crater functions to model surface evolution is treated at greater length in **Chapter 2** of this thesis.

1.2.2 Binary collision approximation approaches

Given the computational demands of MD codes, many researchers have desired a less computationally-expensive approach to modeling the ion-surface interactions. The most commonly-used type of simulations used for this purpose are codes built using the binary collision approximation (BCA) to model the particle interactions. In BCA models, all interactions involving energetic particles are treated as two-body collision interactions, as illustrated in **Figure 1.3**, with

moving particles traveling along straight lines between collisions. Collisions can occur at random locations, simulating an amorphous solid [55], or at precise locations corresponding to crystalline lattice sites [56], although the latter of these is computationally more expensive. In addition, an inelastic (i.e. electronic) energy loss is usually subtracted from the particle energy as it travels between collisions, which does not influence the particle trajectory.

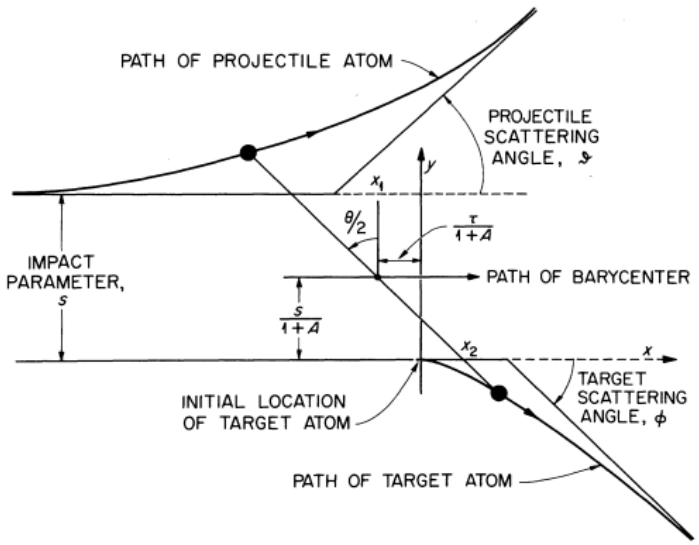

Figure 1.3: Schematic illustration of the two-body collision process used in the binary collision approximation [56].

Easily the most widely-used BCA code today is the SRIM (Stopping and Range of Ions in Matter) package [55,57–59], which is capable of generating data about sputtering yields, angular and energy distributions of sputtered particles, recoil generation, and defect production. Since SRIM generates recoils at random positions, it is unsuited for simulating effects from crystal lattices, and thus for some time the MARLOWE package [56] was an alternative to address this although it has not seen much significant use in recent years. In addition to these, there also exists a class of so-called “dynamic” BCA codes which can track changes in the composition of the target under successive ion impacts. The original dynamic BCA code is TRIDYN [60], which has seen significant use as the SDTrimSP package [61], which is derived from TRIDYN and includes additional features such as outgassing and chemical sputtering models. More recently, an upgraded

version called TRI3DYN has been introduced which is capable of simulating fully-3D compositional and structural changes, albeit while relying on highly stylized models of non-prompt (e.g. diffusive or viscoelastic) mass transfer [62].

Despite the benefits of its relative computational simplicity, the BCA models are not flawless. In particular, the BCA breaks down at low energies (usually for particle energies in the tens of eV), as many-body interactions become increasingly important [56]. In particular, this has been shown to lead to significant discrepancies between prediction of small (<5 Å) displacements for e.g. Ar^+ bombardment of Si [63], which was attributed to the generation of amorphous pockets in the MD simulation which BCA codes are incapable of modeling. Additionally, the BCA model does not include a mechanism for compound formation or other thermodynamic effects, as even the dynamic codes cited previously choose the types or elements of interacting particles in a random fashion. Thus, phenomena such as phase separation or clustering cannot be studied by BCA codes.

1.2.3 Multiscale modeling with kinetic Monte Carlo methods

Since both MD and BCA codes are limited in the timescale and mechanisms which can be included, it is desirable to use another approach which can incorporate the results from these simulations alongside longer-time effects such as surface diffusion or stress-driven flow. One approach to this is to develop a mathematical model, such as those described previously, and then to integrate the resulting partial differential equations numerically using simulation results to determine certain input parameters. There are several recent examples of this approach [16,33,64,65]. An alternative approach which does not rely on solving differential equations is to directly simulate surface evolution via multiple atomistic mechanisms coupled with a Monte Carlo (MC) or kinetic Monte Carlo (kMC) framework. This approach has two advantages over using continuum models: first, simplifying assumptions are not needed for the sake of a tractable model; second, such models can

be extended by modifying or adding specific mechanisms without necessitating a complete re-derivation from scratch.

Many MC/kMC models used to study ion-induced nanopatterning incorporate two primary mechanisms: physical sputtering and surface diffusion. In some early models, sputtering was treated by an analytical approximation relying on arbitrary parameters, along with simplified diffusion models which only accounted for changes in height between different locations [66,67]. On the other hand, Koponen and coworkers were the first group to combine the Monte Carlo method with BCA simulations for every individual ion impact [68–70]. Later work by multiple groups extended the diffusion models to more complex forms which relied on energy differences between sites to determine the energy barriers for different diffusion events [71,72]. This allowed for the rate of diffusion events to be determined, allowing the transition to *kinetic* Monte Carlo methods which incorporated the time dependence between sputtering and diffusion events. This in turn has allowed more sophisticated studies which account for additional energy barrier terms and contributions from multiple-defect sites [73]. As most of these models are based on Bradley-Harper-type mechanisms [8], it comes as little surprise that ripples are predicted to form under most conditions, although at least one instance exists for which an additional "ballistic" contribution from the ion impacts has been shown to produce flat, stable surfaces [69].

While kMC models at present are still relatively simple, recent work has shown that the complexity of these models can be increased to good effects. Kree et al have introduced a modified kMC model which includes a simplified form of compositional phase formation to consider the effect of impurity codeposition [74]. Liedke and Möller have developed a hybrid BCA/kMC code, called TRIDER, which uses BCA to simulate the ion impact including defect production, and then switches to a kMC model of subsurface defect diffusion along a crystalline lattice [75]. This model is suitable for simulating ion irradiation of metallic surfaces, but is not suited for considering

semiconductors since they become amorphous under ion bomabardment and lose their lattice order. Finally, a hybrid MD/kMC model has been introduced which relies on a combination of the crater function formalism with kMC surface diffusion [76–78]. This model is discussed in greater detail as the subject of **Chapter 2**.

1.3 Scope of research

The aim of the present work is to demonstrate the use of large-scale MD simulations, coupled with high-performance computing resources, to elucidate the fundamental atomistic mechanisms which originate in the ion-surface interaction and ultimately drive surface nanopatterning. This work is differentiated not only by the scale of the simulations, but also by a strong analysis focus on compositional and structural changes due to sustained ion bombardment, and how these changes are coupled to and modify the fundamental ion-surface interaction.

Chapter 2 summarizes previous work by the author and others to develop a hybrid MD/kMC computational model of ion-induced nanopatterning, which provides not only significant motivation for the present work but also provides an already-existing platform which can be adapted to include the mechanisms elucidated by this work. **Chapter 3** highlights massive-scale MD simulations of ion-irradiated GaSb surfaces carried out on the Blue Waters supercomputer. The results of this work constitute the first use of atomistic computational modeling to demonstrate a lateral surface compositional variation and instability, which arises due to thermodynamic and ion-induced forces. **Chapter 4** discusses high-fluence MD studies of ion implantation into Si surfaces, achieving a higher total fluence than previous studies [44,48] over a wider variety of irradiation conditions (including the ion energy, species, and incidence angle) than have previously been studied. Here, it is shown that the implanted ions form clusters which interact with the surface and can ultimately influence the formation of nanopatterns or the lack thereof. Finally, **Chapter 5**

offers concluding remarks and a summary of opportunities for future work continuing along these lines.

Chapter 2: The crater function theory model (CFTM): Review and extension[1]

While molecular dynamics (MD) simulations are the fundamental computational technique of the present work, as will be discussed at length in following chapters, the cornerstone which motivates these efforts is the Crater Function Theory Model (CFTM). CFTM is a hybrid kinetic Monte Carlo/molecular dynamics (kMC/MD) simulation which is fully atomistic yet enables multiscale simulation of ion beam patterning at surfaces. This is enabled by the eponymous crater functions, which can be obtained by MD or other techniques discussed previously such as BCA and which allows a complete description of a single-ion impact to be used to simulate the surface evolution. This means, for example, that the effects of sputtering, mass-redistribution, and ion implantation, which have traditionally been considered separately in the literature, can be encapsulated in the crater function and effectively combined to predict the surface evolution due to all of these effects simultaneously. Thus, on the one hand, the crater function approach represents a substantial improvement in the physical realism of computational models for ion-induced patterning.

On the other hand, the fully-atomistic nature of CFTM allows, in theory, for any physical process to be incorporated into the model with no reliance on estimated coefficients or oversimplified functional forms which are used in continuum models and numerical simulators. While the process may not necessarily be simple, CFTM can readily be extended to include effects of compositional phases, crystal structures, or stress-strain interactions given sufficient information from more-detailed atomistic simulation techniques such as MD. Besides this, the model can easily treat complex experimental setups, such as multiple-beam irradiation, which have proven difficult to

[1] This chapter is mostly derived from: Z. Yang, M. A. Lively, and J. P. Allain, "Atomistic simulation of ion beam patterning with crater functions", *Nucl. Instrum. Meth. B* **307** (2013), 189-193 and Z. Yang, M. A. Lively, and J. P. Allain, "Kinetic Monte Carlo simulation of self-organized pattern formation induced by ion beam sputtering using crater functions", *Phys. Rev. B* **91** (2015), 075427. Unless cited otherwise all figures in this chapter were created by the author of this thesis. Z. Yang and the author contributed equally to obtaining the simulation results shown in these figures.

study with more limited continuum models. The latter advantage has already been realized and is discussed below, while the former advantages remain as potential extensions which have motivated the work presented in the rest of this thesis.

Here, the theoretical underpinnings of CFTM are presented to motivate its development, along with a summary of the code implementation. Results of simulations carried out with CFTM are presented alongside experimental data, not only validating the model but also demonstrating its predictive ability. Finally, the potential directions for extension mentioned above are discussed, providing the core motivation for the remainder of the present work. As the presentation here aims chiefly to motivate following chapters, this last point is the most central.

2.1 Theoretical basis for the crater function formalism

Experimental observations of crater formation due to single-ion impacts have been known for quite some time [79–81], but usually could only be observed at high energies since the impact of a single low-energy ion into a surface was too small to be observed in experiments. The idea of a "crater" with a defined rim-and-pit geometry to describe single-ion impacts in this context was introduced by Davidovitch and coworkers [13], as a generalization of the Sigmund model of sputtering to include other potential ion-induced mechanisms such as mass redistribution. In parallel, MD simulations by other researchers [14] not only provided detailed, physically-accurate results for single-ion impacts but also generated sufficient volumes of data to carry out a statistical analysis. Remarkably, the statistically-averaged change in the surface height due to a single-ion impact turned out to have a distinct pit-and-rim crater geometry, as shown in **Figure 2.1**. The same authors also provided the first demonstration of crater functions in a model of surface nanopatterning [64], although this model was a hybrid MD/continuum approach which suffered from using fitted coefficients (one critical coefficient was varied by a factor of 10^{30} to obtain the published results!).

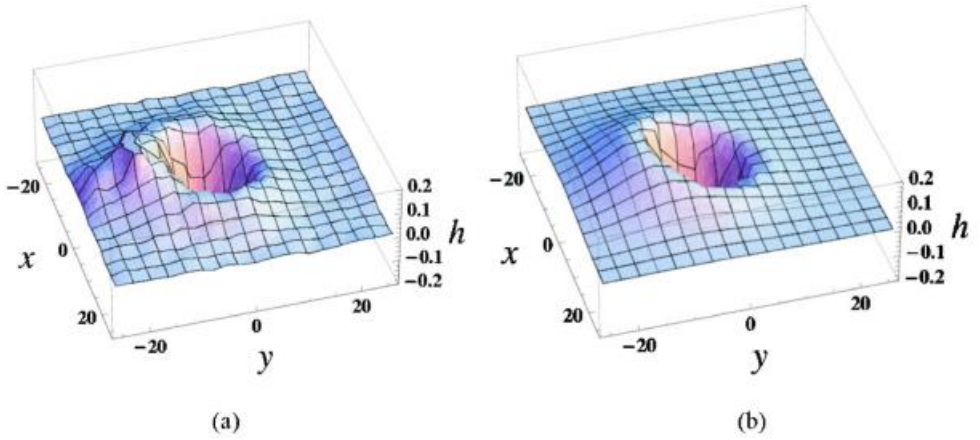

Figure 2.1: (a) statistical average of the surface height change due to a single-ion impact for 500 eV Ar^+ into Si at 28° incidence from ~1000 impacts, projected along the $+x$ direction, showing a distinct crater geometry with a pit and rim. (b) the crater shown in (a) approximated by a difference-of-two-Gaussians functional fit to the data [14].

Norris and coworkers developed [15] and implemented [16] a BH-like continuum model which used crater functions to determine the curvature coefficients. More precisely, this model used the statistical moments of the crater functions rather than the craters themselves, which are easier to calculate and require fewer simulations to be run for coefficients to be determined. While not without criticisms [82,83], this continuum model has since been more widely adopted as the so-called crater function formalism [65], albeit most authors prefer to obtain crater functions from BCA rather than MD for ease of use.

As shown in **Figure 2.1(b)**, the crater function can be modeled with a functional form, such as the difference of two Gaussians given by

$$\Delta h(x,y) = A_1 \exp\{-B_1[D_1 x^2 + (y - C_1)^2]\} - A_2 \exp\{-B_2[D_2 x^2 + (y - C_2)^2]\} \quad (2.1)$$

The subscripts 1 and 2 indicate the positive (rim) and negative (pit) contributions, respectively. The coefficients have the following effects, relative to a single-ion impact projected along the y-direction: The A_i determine the height/depth of the rim/pit; the B_i determine the radius of the rim

and pit; the C_i determine how far the rim and pit project along the y-direction; the D_i determine the "roundness" of the rim and pit, i.e. the ratio of the extent in each lateral dimension. This form was used in early versions of CFTM but is currently abandoned in favor of using accurate "raw" MD data, which may not always fit the functional form very closely. However, one advantage of the functional form of Equation (2.1) is that the sputtering yield is readily estimated (if changes in density are neglected) from integration over the whole domain as

$$Y_{sp} = \pi\left(\frac{A_1}{B_1\sqrt{D_1}} - \frac{A_2}{B_2\sqrt{D_2}}\right) \quad (2.2)$$

although it should be noted that this neglects the implantation of the impacted ion, which if not accounted for can cause irregularities in the crater function.

2.2 Implementation of CFTM

2.2.1 Obtaining crater functions from MD simulations

It should be noted that, while the MD simulation methodology described here is tailored specifically for obtaining crater functions, it represents a prototypical simulation of ion impacts into a surface and therefore the methods used in the following chapters will be nearly identical except for minor changes in the simulation settings or different surface preparation methods. Thus, the methodology given here will be referenced throughout. In all procedures, the LAMMPS (Large-scale atomic/molecular massively parallel simulator) code package is used to run MD simulations [84].

The MD procedure to obtain craters consists of two stages: the surface preparation, and the single-ion impacts. The surface to be bombarded consists of amorphous silicon, representing the ion-

damaged near-surface layer which is present almost immediately once bombardment begins. This layer is formed by heating a simulation cell of "bulk" silicon (i.e. periodic boundaries in all dimensions) to a high temperature well beyond the melting point (4000 K). After being given some time (~15 ps) for the atoms to move about, the hot Si cell is rapidly quenched to 1 K to "freeze" the amorphous structure in place. The cool Si is equilibrated for an additional ~15 ps before the boundary condition in the *z*-direction is changed to a fixed boundary. By holding the bottom of the surface fixed and extending the top of the simulation box by a few nm, a free surface is created which is then equilibrated for another ~15 ps.

The setup for the single-ion impact simulations is shown in **Figure 2.2** and, again, forms the basis for nearly all simulations in following sections. The bottom layer(s) of the surface is (are) held fixed to represent the immobile interface between the surface layers which interact with the incident ions and the bulk Si material. Above this is a thermostat layer which serves to maintain the NVE ensemble by removing excess energy from the system after the ion impact and collision cascade occur. Ions are generated at random (*x*,*y*) coordinates above the surface and given a downwards trajectory calculated from the prescribed incidence angle and energy. Near the top of the simulation box within the vacuum region, sputtered or reflected particles are collected and removed from the simulation box. In many (but not all) simulations, a reflecting wall and/or additional removal region may be located below the fixed layer(s), which serve the purpose of containing incident ions which may rarely make it through the fixed bottom layer. These latter features are not strictly physical, but serve to keep the simulation from crashing due to loss-of-particle errors.

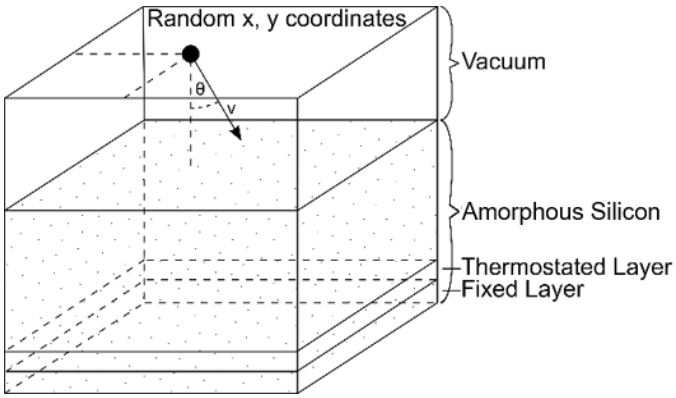

Figure 2.2: Schematic of the MD simulation setup used for studying ion impacts on surfaces, including for obtaining crater functions. The bottom fixed layer represents the "immobile" interface between bulk Si and the near-surface region. Boundary conditions are periodic in the lateral dimensions. Not shown in the vacuum layer is a region from which sputtered or reflected particles are collected and/or removed from the simulation.

To obtain the crater functions, the post-impact surface is compared to the initial surface. Each surface is divided into a 2D grid in the lateral dimensions, with the grid spacing approximately the diameter of a Si atom (about 0.27 nm) in length. Within each square, the atom with the highest *z*-coordinate is found, and the resulting collection of atoms defines the 2D-projected surface height map of the simulation cell. The initial and final surface height maps are then compared; the cumulative result of this comparison over a large number (~1000) impacts then gives the crater function as the statistical average of the surface height change due to a single-ion impact at a given incidence energy, angle, etc. **Figure 2.3** gives several representative examples of these crater functions.

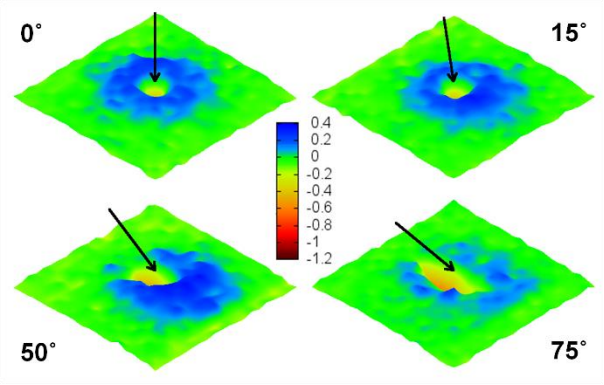

Figure 2.3: Selected crater functions for 500 eV Ar^+ impacts onto Si surfaces at various incidence angles, indicated by the black arrows. The pit-and-rim geometry is clearly visible, with the forward projection of the rim increasing with the incidence angle.

Recalling from earlier discussion that many authors prefer to use BCA rather than MD to obtain crater functions, it is worth briefly comparing the craters obtained by each method. BCA simulations are much quicker and thus more convenient than MD simulations, and if high-quality craters can be obtained by the former method then the latter should necessarily fall out of favor. For the purpose of comparison, several crater functions obtained from BCA simulations [85] are shown in **Figure 2.4**.

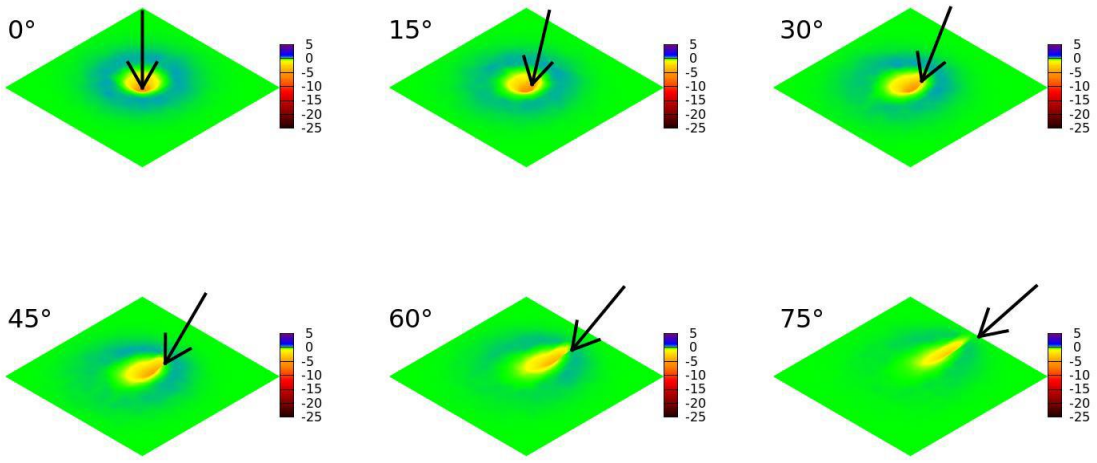

Figure 2.4: Sample crater functions obtained from BCA simulations using the DYNAMIX code [85]. Among the several differences visible when compared to the MD results, the most physically-unrealistic is the depth of the pits, which can be the equivalent of 5-10 atoms deep at most angles, an impossible change in the surface from a low-energy single-ion impact.

The crater functions from BCA clearly compare very poorly to those obtained from MD simulations. Most importantly, the scale of the crater features is very unrealistic – the pits are up to ten atoms deep, and the rims can be equivalent in height to a two-atom stack. For a single-ion event, these dimensions are next to impossible. While some of these issues can be solved with refinements of BCA codes, other issues are intrinsic to BCA due to known weaknesses of that modeling technique, such as a lack of many-body interactions which affects the final position of displaced atoms in the lattice.

2.2.2 Structure of the code for CFTM

To model the evolution of the irradiated surface, the crater functions are used to model single-ion impacts and are combined with a kinetic Monte Carlo approach to include surface diffusion. The surface itself is treated as a square *xy*-grid representing the height at each point, with periodic boundary conditions in the lateral dimensions. The initial surface is atomically rough. In order to connect the rate of ion arrivals at the surface (i.e. the beam flux or current), to the changing surface diffusion rate, two "clocks" are run in parallel. One clock is updated by a constant dt_{ion} after each impact, while the other is updated by a variable dt_{diff} after every surface diffusion event, with the clock having a lower total accumulated time determining which type of event occurs next. In this way, the simulation can be considered to take place in "real time". This is an improvement over previous kMC models [72] which would use sweeps over the entire surface at periodic intervals to model diffusion processes instead of representing the physical diffusion rate.

When an ion impact occurs, the incident ion is generated a few nm above the surface and approaches along a trajectory based on the incidence and azimuthal angles of the simulated beam. This allows for effects such as shadowing to be included, which may be relevant at higher length scales [86]. The ion is considered to have impacted the surface at the point where its *z*-coordinate

is lower than the surface height at the same (x,y) coordinate. The local incidence angle is calculated based on the global incidence angle of the ion beam and the slope of the surface in the region near the impact point, and a crater function is chosen to represent the impact using this local incidence angle. This allows the effects of surface slope, curvature, and so forth to be included as well. To apply the crater function, the heights of nearby grid points are adjusted up or down based on their position relative to the impact point. Once this is done, the instantaneous diffusion rates for all affected grid points are recalculated to reflect the new surface geometry.

To track the total diffusion rate, the simulation calculates the diffusion rates for all possible events at the beginning of the simulation and updates these for coordinates which are modified during the simulation. From this, the total diffusion rate can be calculated as the sum of all individual diffusion rates. The diffusion rate for an individual atom to hop from one site to another is determined by the activation energy, ΔE_a, which is based on the difference in coordination between the atom's initial and final positions and can be given as:

$$\Delta E_a = E_s + E_{\Delta nn} + E_{ES} \quad (2.3)$$

The first term, E_s, represents a minimum substrate energy barrier which is always present. The second term is defined as $E_{\Delta nn} = E_b \times \max(n_i - n_f, 0)$ with E_b as a binding energy term and (n_i, n_f) being the coordination number of the initial and final sites, so the overall term represents a contribution from the net difference in bonding between two locations – which, however, cannot reduce the energy below the minimum value, E_s. The third term, E_{ES}, represents an energy barrier preventing atoms from approaching step edges known as the Ehrlich-Schwoebel barrier [87–89]. This latter term is only applicable to crystalline surfaces, and thus is usually set to zero here because the surface is considered as amorphous Si in the following studies.

The diffusion rate is then given as

$$\nu = \left(\frac{2k_B T}{h}\right) \exp\left(-\frac{\Delta E_a}{k_B T}\right) \quad (2.4)$$

which is the well-known Arrhenius relation with T as the surface temperature. Summing the diffusion rates gives the total surface diffusion rate, U, the inverse of which is the mean time between diffusion events. The time for a single event to happen is then determined by generating a random number, r, in the range [0,1), and calculating

$$dt_{diff} = \frac{1}{U} \ln\left(\frac{1}{r}\right) \quad (2.5)$$

In this manner, the clock associated with surface diffusion is incremented until it exceeds the value of the impact clock, and the simulation carries on until the desired ion fluence is reached.

2.3 Comparison of simulation results to experiments: Validation and prediction

2.3.1 Model validation against experimental results for Ar ion irradiation of Si

For validation of the model, low-energy Ar^+ irradiation of Si was chosen as the test case due to an abundance of experimental work on this system. In particular, the surface morphology for this system had recently been functionalized with respect to the ion beam energy and incidence angle [90,91], leading to the construction of the nanopatterning phase diagram for Ar-on-Si, as seen in **Figure 2.5**. From this and the other wealth of studies on this system, CFTM could be validated at three progressive levels:

1. Pattern formation: Does the model generate patterns at all?
2. Patterning regimes: Do the simulations predict the same types of patterns under the same conditions as the experiments?
3. Pattern characteristics: Do the simulation results agree with experimental measurements of ripple wavelengths, amplitudes, etc. and their dependence on various key parameters?

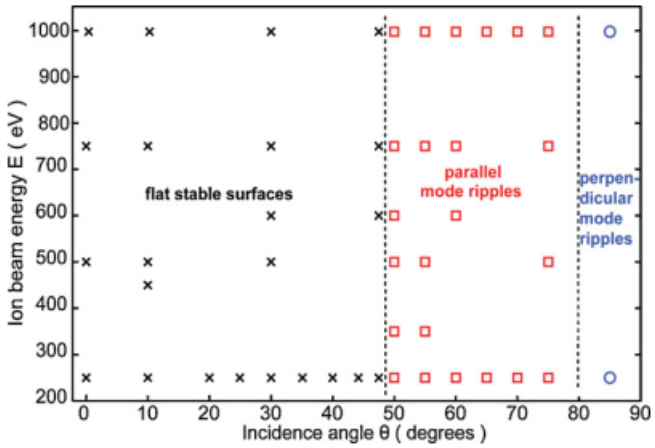

Figure 2.5: Ripple formation phase diagram for low-energy Ar^+ irradiation of Si(001) [91]. For normal or near-normal incidence angles, the surface remains flat, but as the incidence angle increases the surface is destabilized and ripple nanopatterns form. At grazing incidence angles, the orientation of the ripples relative to the ion beam is rotated by 90°. The trend is the same for all energies shown, although the quantitative characteristics of these ripples can vary with energy as well.

Examples of simulated pattern morphologies are given in **Figure 2.6** for a few different incidence angles of the ion beam. For low incidence angles near normal incidence, the surface is mostly flat with no patterning or other notable features aside from some residual roughness from the most recent ion impacts. As the beam incidence angle approaches 40° a new morphology arises, which has previously been described as a "transition" type but is probably more-correctly classified as parallel-mode ripples. These patterns occur for a wide range of incidence angles up to about 70-75°, with some dependence of the pattern characteristics on the incidence angle. For example, by comparing the results for 40° and 60° incidence in **Figure 2.6**, it can be seen that the ripple wavelength decreases slightly with the higher incidence angle, the ripple amplitude increases with the same, and the overall ripple quality improves (suggesting a more-rapid self-organization

process). All of these observations indicate that the patterning instability becomes stronger as the incidence angle increases. Finally, at grazing incidence angles the rippled patterns break down into isolated structures with no ordering. Overall, CFTM is demonstrably capable of predicting a rich variety of nanopatterns which depend on easily-accessible experimental parameters.

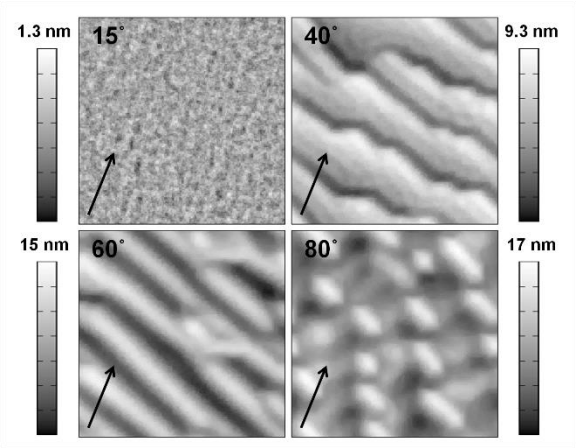

Figure 2.6: Snapshots of the simulated Si surface for 500 eV Ar^+ irradiation to a fluence of 2×10^{17} cm^{-2}. The bean direction is indicated by the arrows, along with the incidence angle for each result. Each snapshot is 54.4×54.4 nm^2.

The next important question, then, is whether these predicted morphologies have any basis in experimentally-determined reality. To assess this, a phase diagram was created analogous to the one in **Figure 2.5** for experimental data, which represents the results of the simulations for various incidence angles and energies, which is shown as **Figure 2.7** below. In general, the simulated results in this phase diagram show good agreement with those presented in **Figure 2.5**, but some discrepancies do exist. In particular, the transition angle for the flat-to-rippled transition is questionable, since the so-called "transition" ripples should probably be considered part of the parallel-mode regime and the transition angle considered between 35-40°, which is somewhat lower than the experimental value of about 48°, even though predicting the transition is still an improvement over the Bradley-Harper-type approaches [8]. It is worth noting that this issue also arises for the model of Norris and coworkers, who also use the crater function concept to derive their model and similarly predict a lower-than-experiment transition angle of around 35° [16],

which suggests that there is still some important mechanism influencing pattern formation which is not well-incorporated by crater functions.

A further discrepancy between the simulations and experiments is the pattern type at grazing incidence angles. While experimental observations indicate the formation of perpendicular-mode ripples, the simulations only predict the formation of disordered stripes, although a transition is still predicted which is an improvement over some other models, e.g. the so-called "hydrodynamic" models of Castro, Cuerno, and coworkers [31,33]. This is attributed to the fairly poor quality of the crater functions obtained at grazing (>80°) incidence angles, which are obscured or dominated by statistical noise and may not rely on an accurate determination of the ion impact point. In fact, when only erosive effects are included, the amount of noise is reduced substantially and simulations at high incidence angles do in fact predict the formation of perpendicular-mode ripples, as indicated in **Figure 2.8**. This suggests that CFTM would be capable of predicting the same morphology with higher-quality craters at these angles, so that the erosive effects were not obscured by noise.

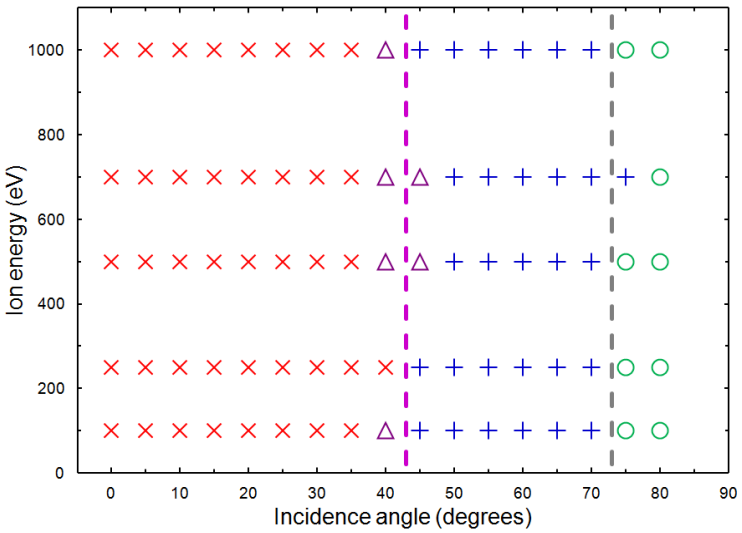

Figure 2.7: Phase diagram of simulated pattern morphologies for various ion beam energies and incidence angles. The symbols each represent a different morphology: × flat surfaces; Δ "transition" ripples; + parallel-mode ripples; and ○ disordered stripes. Dashed lines mark approximate transition angles between different morphology regimes.

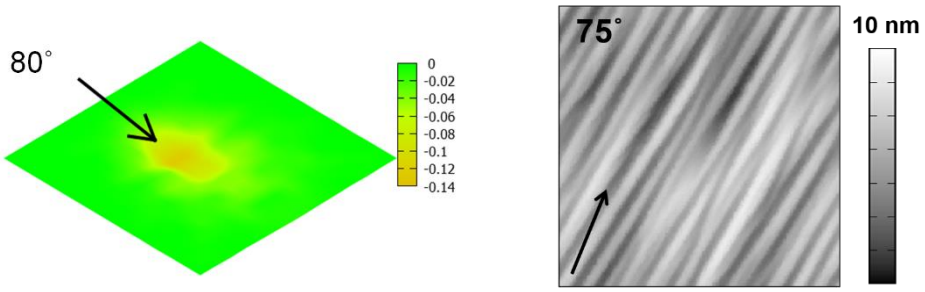

Figure 2.8: (left) Example of an erosion-only crater at grazing incidence, in which the lack of minor height variations leads to nearly no noise, since only sputtered atoms (or more precisely, the removal thereof) are included. (right) Example of simulation results at high incidence angles when erosion-only crater functions are used, showing that perpendicular-mode ripples can be generated by CFTM with the appropriate crater function input.

Finally, knowing that CFTM is capable of making reasonably-good predictions of ion-induced surface morphology types, it is important to assess its capability to predict the quantitative characteristics of those patterns as well. For most purposes, the pattern amplitude and wavelength are the important measurements, and experimentally these tend to be on the order of a few nm and a few 10s of nm, respectively, in the energy range of interest [90,92]. By comparison, the ripples obtained from the simulation and shown in **Figure 2.6b** have amplitudes on the order of ~10 nm, which is noticeably larger than the experimental results, and wavelengths of around ~10 nm as well, which is somewhat smaller but reasonably close to the values measured experimentally. Since the formation of the patterns is determined by the nature of the destabilizing mechanisms, which in CFTM are incorporated by the crater functions, this suggests that the stabilizing contribution (thermally-activated surface diffusion here) is insufficiently-strong to mediate the pattern-driving forces enough to obtain the longer-wavelength, lower-amplitude structures. It is not clear if this is because the diffusion inputs such as energy barriers are incorrect, or if surface diffusion itself is an insufficient mechanism to model the surface evolution accurately.

Further quantitative assessment can consider the trends for how these key values vary with simulation parameters. **Figure 2.9** shows an example of this analysis, comparing the ripple wavelength from experiments and from simulations. The experimental data shows a strong linear

relationship between the ripple wavelength and the incident ion energy. Meanwhile, the simulation results do show a linear relationship between wavelength and energy, but the dependence is much weaker in contrast with the experimental analysis. This again suggests that the mechanisms included to model surface relaxation are insufficient to fully describe the surface evolution, and some additional gradual response term representing e.g. stress-driven viscoelastic or plastic flow must be included for future studies with CFTM.

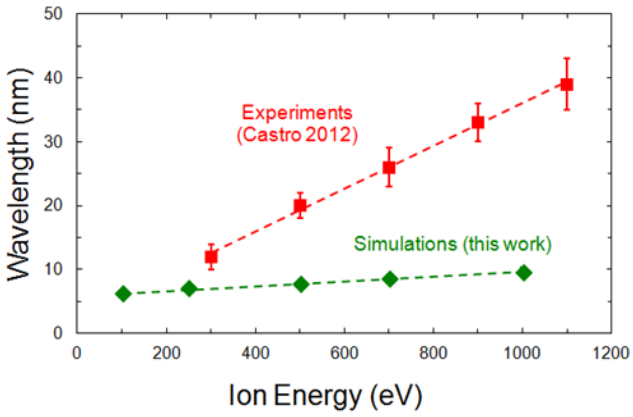

Figure 2.9: Comparison plot of parallel-mode ripple wavelengths dependent on the incident ion energy for experimental data [92] and simulation results from CFTM, showing linear relationships for both cases but with quite disparate magnitudes.

2.3.2 Testing model predictive ability for Kr irradiation of Si

Since CFTM is demonstrably capable of simulating a well-studied system and achieving reasonable agreement with experimental results, it is worth also testing the ability to use the model to make predictions which can be confirmed by experiments. To carry this out, low-energy ion irradiation of Si with Kr^+ ions was selected as a target system, since in contrast to Ar-on-Si the Kr-on-Si system is not well-studied in the literature, surprisingly. Crater functions were obtained, and simulations carried out, for 100 and 500 eV cases. These two energies were chosen because 100 eV is very near to the sputtering threshold energy for Kr^+ from Si surfaces (below which the sputtering yield per

incident ion is effectively zero). Thus, a key hypothesis to be tested was that the near-threshold energy would lead to a significant difference in the patterning regime.

For 500 eV irradiations, simulations were carried out and compared with experimental results for the same conditions obtained at the Ion-Gas-Neutral Interactions with Surfaces (IGNIS) facility at the University of Illinois. The results indicate good agreement between the simulation predictions shown in **Figure 2.10** and the surfaces obtained from experiments shown in **Figure 2.11**. The prediction of whether or not patterns formed was confirmed by the experimental data, and the measured wavelengths in each case were in close agreement, with the simulation prediction of $\lambda \approx$ 15 nm agreeing well with the experimental result of $\lambda \approx$ 18 nm. The greatest disagreement was the amplitude, predicted to be ~32 nm but only measured to be ~3 nm experimentally. This may be partially attributable to the fluence difference, however, particularly due to native oxide formation on the Si surfaces in the experiments prior to irradiation, which can delay pattern formation for a non-negligible amount of time.

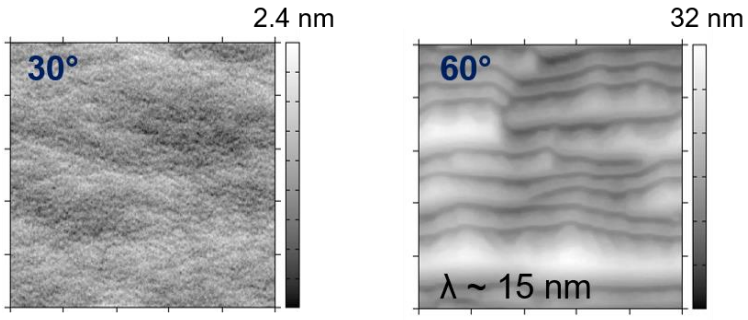

Figure 2.10: Snapshots of simulated Si surfaces after bombardment by 500 eV Kr^+ to a fluence of 10^{18} cm^{-2}. Snapshots are 135 × 135 nm^2.

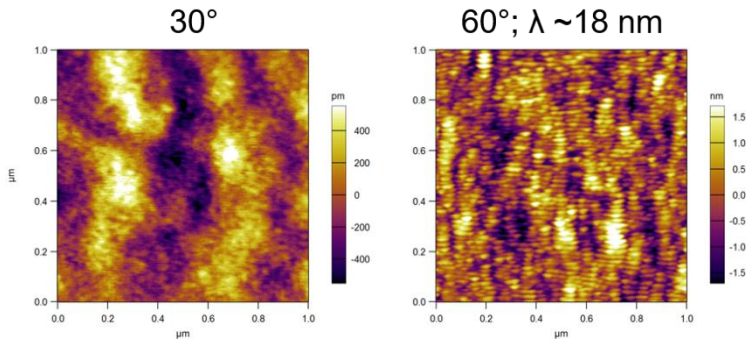

Figure 2.11: AFM scans of Si surfaces irradiated with 500 eV Kr^+ to a fluence of 2×10^{17} cm^{-2}.

The comparison between simulated results for the 500-eV case above and the 100-eV near-threshold case confirmed the hypothesis of a pronounced difference in morphologies due to the near-threshold energy of the latter. As shown in **Figure 2.12**, several changes in morphology occur between the two energies:

- The flat-to-rippled transition occurs much earlier for the 100-eV case. However, the ripple wavelength and amplitude are both much smaller than the values at the (higher-angle) transition for the 500-eV case, which is not expected from conventional understanding i.e. bifurcation theory [90,93].
- The shapes of the ripples obtained at higher angles for 100 eV bombardment distinct from those obtained at higher energies, being very sharp and angular rather than smooth and rolling.
- The ripple wavelength for 100 eV actually *increases* for higher incidence angles, which is the opposite of conventional expectations.
- These results have not yet been corroborated experimentally by any work done at IGNIS or any other facilities, and should be a subject of future experimental investigations, particularly since near-threshold effects in general have received very little attention in the broader literature.

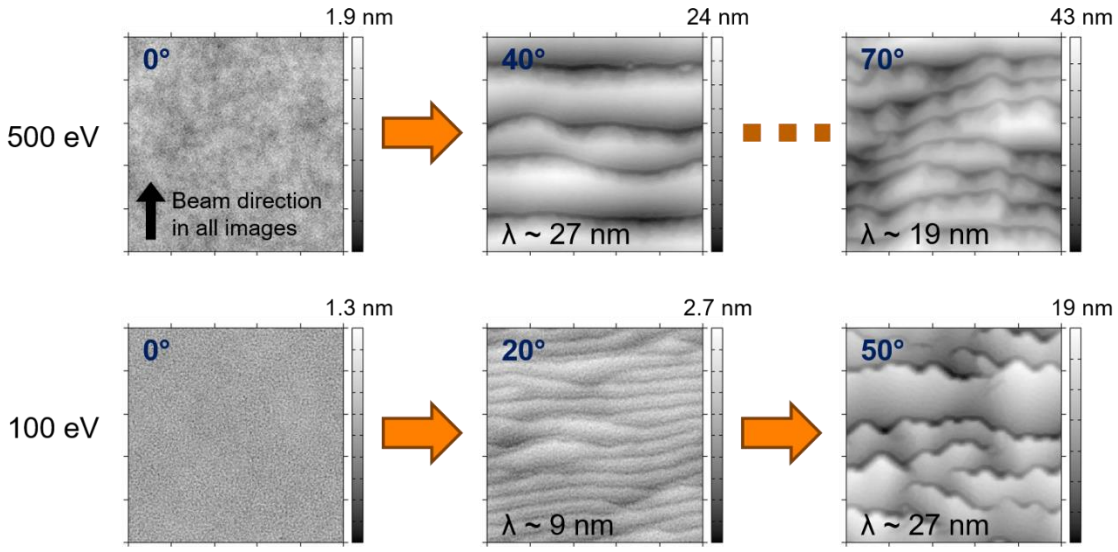

Figure 2.12: Snapshots of simulated Si surfaces under Kr^+ bombardment to a fluence of 10^{18} cm^{-2} for various incidence angles at both 500 eV and the near-threshold "special case" of 100 eV. Snapshots have dimensions of 135 × 135 nm^2 and are selected as representative of the various morphological transitions as a function of the ion beam incidence angle.

An additional point to consider to assess the effects of the near-threshold energy is the contrast between morphologies obtained on for Kr^+ versus those obtained previously for Ar^+. **Figure 2.13(a)** shows that the sputtering yield for Ar^+ ions incident on Si surfaces is at least ~0.1 atoms/ion for any incidence angle except for grazing incidence, while for Kr^+ ions the yield is nearly-zero for a large subset of possible incidence angles, so a comparison between these two species highlights the effects of the near-threshold energy quite well (since 100 eV is not near the threshold for Ar^+ sputtering). From the comparison of morphologies shown in **Figure 2.13(b)**, a few key differences are apparent. At 60° incidence, both species generate the same general pattern type (parallel-mode ripples), but the topographies are quite different as the Ar-induced ripples are quite rough while the Kr-induced ripples are fairly smooth. At 70° incidence, however, there is a major contrast between the pattern types obtained as Kr^+ ions continue to generate parallel-mode ripples while the morphology for Ar^+ irradiation undergoes a transition to the short stripes observed previously. For Kr^+, in fact, no ripple orientation change was observed for the highest angle studied (80°), which is consistent with observations from simulations of Ar-on-Si that the perpendicular-mode ripples

are induced primarily due to erosive effects [65]. Since for 100 eV Kr^+ the sputtering from Si is negligible, it reasonable to expect that erosion-induced perpendicular-mode ripples will not form, and thus no transition of ripple orientation will be observed. Again, this should provide motivation for experimental studies to confirm this near-threshold effect, which would also provide significant insight into the questions about which fundamental mechanisms drive nanopatterning, which are still debated in the present day.

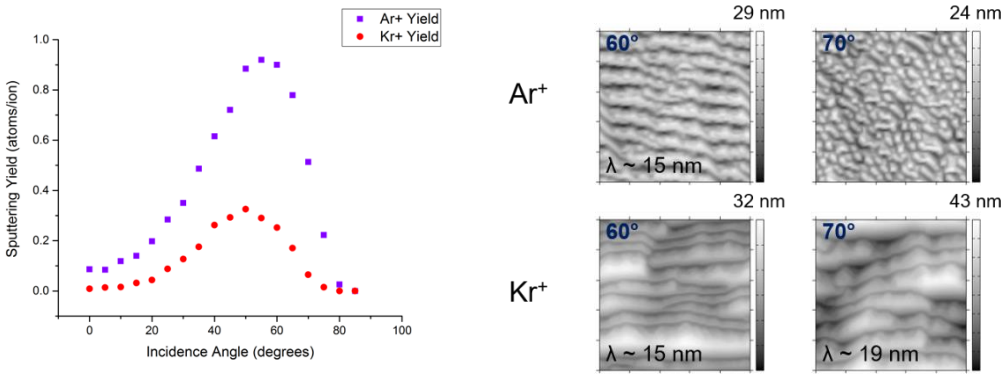

Figure 2.13: (left) Sputtering yields at 100 eV for varying incidence angles of Ar^+ and Kr^+ ions incident into Si, showing that the sputtering yield for argon ions remains significant while the yield is near-zero for much of the incidence angle range for krypton ions. (right) Snapshots of simulated Si surfaces for 100 eV bombardment by both ion species to a fluence of 10^{18} cm^{-2}, showing the differences in pattern morphologies obtained with each ion species.

In summary, CFTM is an effective modeling tool which can not only validate and expand on experimental results, but has predictive abilities to drive experimental investigations into new or understudied systems and to elucidate new mechanisms (such as near-threshold effects). The use of the crater functions to describe the ion-surface interaction offers a *complete and intuitive* description of the relevant physics, which is a significant advantage over the majority of other models currently being studied in the broader community. These characteristics make it a strong platform for extension and expansion to consider new, more-complex classes of materials, such as multicomponent systems or those which retain a crystalline structure under sustained ion bombardment. Potential avenues for these extensions, which motivate the bulk of the remainder of this thesis, are discussed in more detail at the end of this chapter in **Section 2.4**.

2.3.3 Demonstrating model capability for unique experimental conditions

One of the critical advantages of CFTM (and atomistic computational modeling in general) is the ability to readily include novel experimental setups such as multiple ion beams [94,95] or rotating/oscillating samples [9,96,97]. The variety of patterns such setups can access is quite rich and a sample of these is shown in **Figure 2.14** for a visual reference.

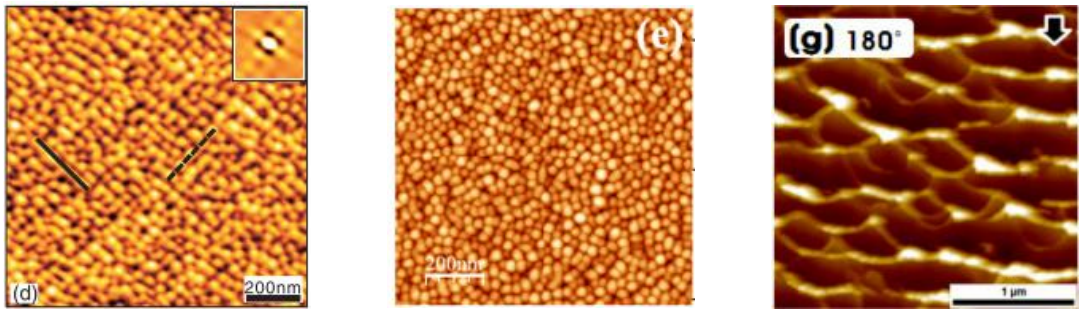

Figure 2.14: Example of nanopatterns obtained from complex experimental configurations. (left) Square-ordered dots obtained on the Au(001) surface for 2 keV Ar^+ simultaneous dual-beam irradiation along the directions indicated by the solid and dotted lines [95]. (middle) Disordered dots obtained on silicon for 500 eV Ar^+ irradiation with concurrent sample rotation at 15 rpm [9]. (right) Steep ridges formed on HOPG by 2 keV Ar^+ bombardment with concurrent sample oscillation through a swinging angle of 180° [97].

Conventional continuum theories are limited, at best, when trying to understand the pattern formation and growth under these conditions. An early model by Bradley [98] incorporates a "rotating" ion beam[2] by considering the ions to come from random directions, allowing the "beam" to be simplified as a completely-isotropic distribution of ions. However, this model is not able to handle finite rotational speeds (although a more-complex formulation is given for this case, it is not analyzed in detail and may not be tractable for intermediate rotation rates – for very slow rotation an approximation is readily done). Models for multiple ion beams, on the other hand, cannot correctly predict the patterning instability within the linear regime [94,99], and while

[2] Note that sample rotation in the laboratory frame can equivalently be considered in the sample frame of reference, as the sample being held fixed with an ion beam rotating around it. This "transformation" of coordinates is used in all approaches, both mathematical and computational, and should be considered automatic for all models discussed here, including CFTM.

alternative mechanisms have been proposed no satisfactory model based on those mechanisms has yet been presented in the existing body of work.

In contrast, CFTM has demonstrated a capability to consider these systems. For example, **Figure 2.15** shows the results obtained for dual-beam simulations of Ar-on-Si bombardment. For low incidence angles, the surface remains relatively featureless, just as in the single-beam case. However, at higher incidence angles the surface instability becomes significant and square-ordered dots evolve, becoming more apparent as the incidence angle increases. While not directly relatable to the experimental results for the same setup for irradiation of Au(001), due to the difference in materials, the qualitative results are in good agreement.

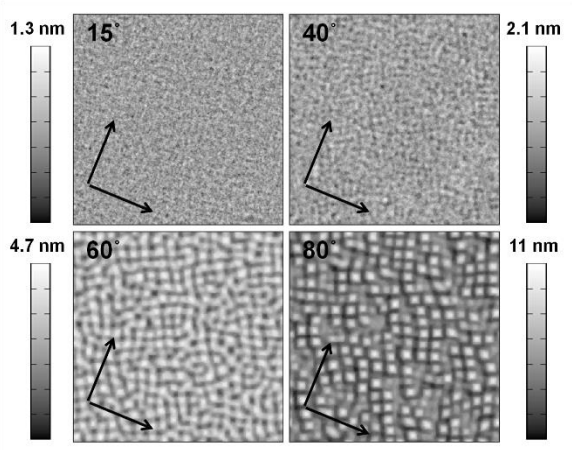

Figure 2.15: Snapshots from simulations of 500 eV Ar^+ dual-beam irradiation of Si for various incidence angles. Each snapshot is 108 × 108 nm^2 and the fluence in each case is 2.5×10^{16} cm^{-2}.

Finally, results for simulations of rotated surfaces are shown in **Figures 2.16 and 2.17**. The snapshots for rotation in **Figure 2.16** are representative of a relatively high rate of rotation, corresponding to about 12 rpm, and show a clear correlation to the morphologies obtained under the same conditions (**Figure 2.6**), with a general trend from featureless, mostly-flat surfaces to arrays of disordered dots or holes. In a significant improvement over the continuum models, the rate of rotation can be varied easily rather than considered to be effectively infinite, allowing the study of morphological changes as the rotation rate is slowed down. In fact, for a sufficiently slow

rotation rate as for the results shown in **Figure 2.17**, a morphology occurs which consists of poorly-ordered ripples that rotate in orientation as the beam direction changes relative to the surface. Continuing in this vein, studies to account for the effects of sample oscillation, a seemingly-similar technique which has been shown to produce dramatically-different morphologies on graphitic surfaces [97], are the subject of ongoing work.

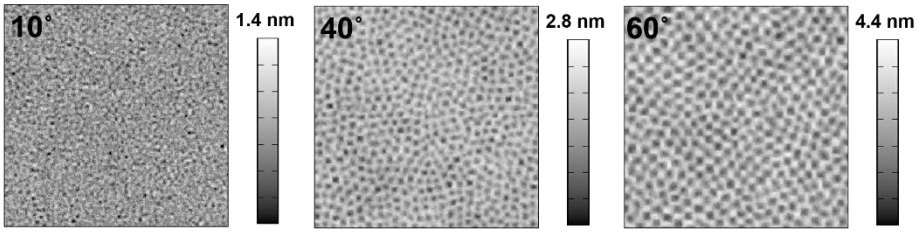

Figure 2.16: Snapshots of simulated surfaces for 500 eV Ar^+ irradiation of Si with concurrent sample (beam) rotation at a fixed rate of 1.257 rad/s for several incidence angles. Each snapshot is 70 × 70 nm^2 and shows the surface after a fluence of 10^{17} cm^{-2}.

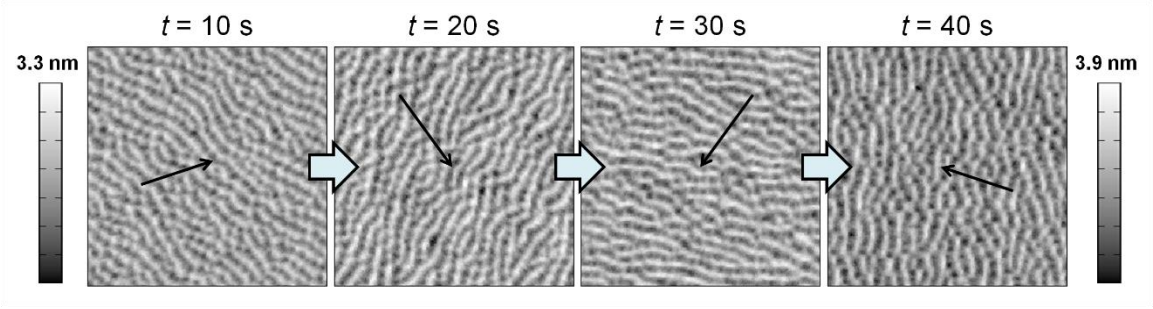

Figure 2.17: Surface snapshots for simulations of 500 eV Ar^+ irradiation of Si with concurrent sample (beam) rotation at 0.126 rad/s (about 1.2 rpm) for various times, with the instantaneous beam angle indicated by the arrows. Each snapshot is 70 × 70 nm^2 and the angle of incidence is 60°.

2.4 Extensions to multi-component complex systems

In order to improve CFTM to a point where it can be considered technologically relevant, it is necessary to extend the mechanisms so that it is able to model complex materials under ion irradiation. This necessarily means that CFTM must be able to consider, in particular, multicomponent surfaces, as nearly all technologically-important materials consist of more than one element. This is true even for Si, which can have numerous dopant species incorporated in

addition to the implanted ions themselves which can in fact also play a significant role in the surface evolution, such as the formation of bubbles or clusters in the subsurface [43,100] which could be treated e.g. as secondary phases within the bulk Si matrix. To consider this requires modifications to CFTM itself and also to the underlying concept of the crater functions and the procedure for obtaining them.

As the compositional mechanisms which may be activated by ion irradiation are manifold and often quite complex in their own right, a strong fundamental understanding of their underlying physics is essential to proceed. This is true not only when considering the mechanisms to be incorporated into CFTM itself, but also when considering the parameterization of the crater functions. For example, Norris and coworkers have adapted the crater function formalism for consideration of III-V semiconductors such as GaSb [54]. However, this work was initially only done for homogeneous target surfaces, with linear interpolation between a few selected compositions. Experimental work, however, has clearly indicated that not only does the surface composition change during ion irradiation, but that a nonlinear compositional depth profile evolves which varies with the incident ion mass and fluence [30]. Thus, the crater functions must consider a fully-3D compositional profile; neither homogeneous targets of varying composition [29] nor homogeneous targets with an enriched surface layer only [101] are sufficient parameter spaces for the crater functions to completely model the surface evolution, particularly if sub-surface effects of the ion impact are also incorporated.

Therefore, before crater functions can be obtained, CFTM can be extended, or any other major multiscale modeling effort can be undertaken, a solid understanding of the fundamental ion-surface interactions in multicomponent materials must be gained. The ideal modeling approach to address this need is a combination of MD simulations and high-performance computing platforms. The former of these provides an atomistic view of how the ion impacts modify the surface with detailed

(classical) physics, while the latter grants the computational resources necessary to access the large length scales and high cumulative ion fluences necessary to observe not only how the surface evolves in response to many ion impacts, but also how these changes in turn influence how the ion-surface interactions play out, allowing for coupling of disparate length and time scales within the limits of the MD paradigm. The remainder of this thesis details the process and results of implementing this approach.

To define the scope of this work, two distinct material systems are considered:

1. Ion irradiation of III-V semiconductors, principally GaSb, which is known from experiments to lead to the formation of quantum dots [4]. As the principal surface components are usually present in equal concentrations, from a scientific standpoint this system provides a testbed to study phenomena such as ion-induced phase separation and the effects of surface segregation.
2. Ion implantation and cluster formation in Si. While the previously-mentioned cluster formation is well-established in the field, the actual effects of these clusters on morphology are not understood. This system serves as an initial foray into more general systems with impurities present.

Chapter 3: Massive-scale molecular dynamics simulations of ion beam nanopatterning on III-V semiconductor surfaces[3,4]

Compared to the relatively simple single-component surfaces such as elemental Si, ion beam nanopatterning of multicomponent surfaces such as III-V semiconductors has shown a much greater diversity and complexity of morphologies. In addition to ripples similar to those obtained on Si [102], irradiation of III-V surfaces at normal incidence may lead to the formation of quantum dots at the surface, where the existence of these structures as well as characteristics such as size and shape depend strongly on the elemental ion-target combination [29]. These patterns are inherently stochastic in nature, due to the inherent randomness of the ion impacts, and result from a combination of athermal mechanisms (e.g. ion sputtering, ion-induced defect formation and amorphization) and thermal mechanisms (e.g. thermodynamic phase separation, asymmetric diffusion). These mechanisms remain poorly understood despite significant experimental and computational investigations. In this chapter, results are presented for molecular dynamics investigations of ion-surface interactions and pattern-forming instabilities on GaSb surfaces. These simulations have been carried out on a massive scale in both length and time (fluence), which is unprecedented in magnitude for the ion beam nanopatterning field. By performing atomistic simulations on such a large scale, it is possible to connect the ion-induced structural changes and compositional depth profile to the emergence of lateral compositional variations which can form the basis for a pattern-forming morphological instability to develop.

[3] This research is part of the Blue Waters sustained-petascale computing project, which is supported by the National Science Foundation (awards OCI-0725070 and ACI-1238993) and the state of Illinois. Blue Waters is a joint effort of the University of Illinois at Urbana-Champaign and its National Center for Supercomputing Applications.

[4] Parts of this chapter are derived from the following article-in-press: M.A. Lively et al., "Massive-scale molecular dynamics of ion-irradiated III-V compound semiconductors at the onset of nanopatterning", *Nucl. Instrum. Meth. B* (2017). No direct contribution to the figures, tables, or data taken from this publication for use in this chapter was made by the other authors of this publication.

3.1 Motivation

Since the first experimental discovery of ion-induced quantum dots created on GaSb surfaces [4], significant experimental and theoretical work has been dedicated to understanding the formation of these nanostructures. Initially, the mathematical models used to explain the pattern formation did not include compositional changes, attributing pattern formation to a nonlinear damping term originating in redeposited material [103]. More recent experiments have indicated the importance of compositional changes, such the presence of a Ga-enriched surface layer [104,105] which becomes Sb-enriched under further irradiation [106], a change attributed to ion-induced thermodynamic phase segregation at the surface [107]. It has been postulated, but not confirmed experimentally, that the phase separation may be caused by an ion-enhanced mobility due to the energy deposited by the collision cascade [29].

Very recently, angle-resolved Auger electron spectroscopy has been used to show that not only does the first layer of atoms become altered, but in fact that a compositional depth profile develops in ion-bombarded GaSb which has a complex form that evolves over time (i.e. with fluence) [30]. The form of these depth profiles are shown in **Figure 3.1**. Initially, the first layer of atoms is entirely composed of Ga, while the near-surface layers within 1-2 nm depth are enriched in Sb, similarly to the expected compositional profile from Gibbsian phase segregation at the surface [108]. As bombardment proceeds, the first layer gains an increasing amount of Sb, while the degree of subsurface Sb enrichment decreases. This suggests that Sb is being driven to the surface over the course of the bombardment, implying that some degree of Sb must be present at the surface before nanopattern formation can occur.

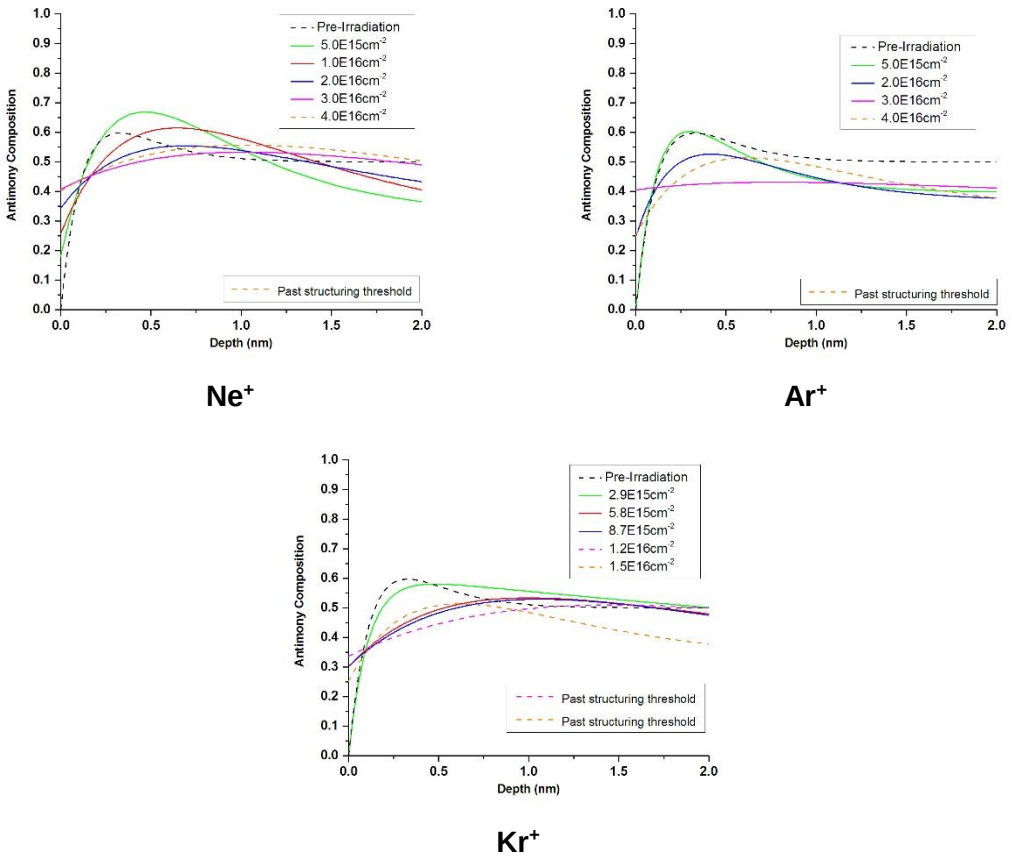

Figure 3.1: Compositional depth profiles of GaSb irradiated at 500 eV and normal incidence with Ne^+ (upper left), Ar^+ (upper right), and Kr^+ (lower) to various fluences, obtained experimentally via angle-resolved Auger electron spectroscopy [30].

In parallel with experimental investigations, work has also been done to develop theoretical models which incorporate compositional mechanisms. At present, two principal models have been proposed. The first model holds that compositional and morphological evolution proceed simultaneously due to a combination of curvature-dependent sputtering and preferential ion-induced redistribution of one component across the surface [6,21,22]. The second model conjectures that the compositional instability evolves first, leading to lateral phase separation due to preferential sputtering, and that this separation induces a "sputter shield" effect wherein islands of the low-yield phase "shield" the underlying material while the surrounding surface is eroded, yielding dot or cone-like nanostructures [7,23]. Seemingly contradictory, both of these models predict the "expected" nanodot morphology, but predict completely opposite lateral compositional

profiles. Since experiments are not able to access the lateral compositional distribution, it is not clear which model, if either, offers a credible and viable explanation of nanopattern formation. Conversely, there does not yet exist a theoretical model which incorporates the effects of the ion-induced compositional depth profile to generate a lateral pattern-forming instability.

The emergence of a compositional depth profile like that shown in **Figure 3.1** provides two broad avenues for pattern-forming mechanisms to become active. At the atomic scale, the nature of the single-ion impact and collisional cascade can vary with composition. However, this scale is smaller than can be realistically accessed with current experimental techniques, which means that theoretical models must rely on speculation or *a priori* assumptions about the nature of these interactions to derive their driving force terms. On the other hand, nonstoichiometric composition can induce large-scale phenomena such as phase separation or asymmetric diffusion. These mechanisms form the basis of the models discussed above, but are difficult to ascertain experimentally since nanometer-resolved compositional analysis is not easily performed.

In light of this, there exists a clear need for atomistic computational modeling to address the disparity between experimental and theoretical knowledge. In particular, two principal knowledge gaps can be formulated which define the scale and scope required for the necessary simulations:

First, the experimentally-observed compositional depth profile [30] *must be connected to the lateral pattern-forming instability necessary for nanopattern formation* [6,7,21–23]. Since quantum dots do not form for normal-incidence irradiation of single-element materials such as Si, this driving instability must be compositional in nature. Thus, atomistic modeling is required to incorporate the detailed nature of interatomic bonding leading to e.g. phase separation. Simultaneously, the expected scale of any lateral compositional instability will be of the same order as the characteristic spacing of the quantum dots studied experimentally, which can be from 30-60

nm [4,29,109]. This implies that a large-scale simulation covering lateral dimensions on the order of 100 × 100 nm^2 is called for. Ideally, the results of these simulations can not only show how a lateral compositional variation is developed from the depth profile, but also clarify which theoretical mechanism – if any of those proposed thus far – leads to the critical pattern-forming morphological instability.

Second, the atomic-scale ion-surface interactions leading to the formation of a compositional depth profile must be discovered. While the compositional depth profiles themselves, as shown in **Figure 3.1**, are fairly well-characterized, the physical reason for the emergence of a depth profile is not yet known. One conjecture has been that the energy deposition from the incident ions is able to induce a Gibbsian-type segregation of Sb to the surface [30]. Alternatively, an ion-enhanced diffusive mechanism could be at play, since Ga is known to diffuse much faster than Sb in GaSb [110]. Atomistic modeling provides the capability to investigate these and other potential mechanisms from the single-ion impact scale up to the scale of pattern formation. While long-time mechanisms such as diffusion or stress-driven flow may be beyond the temporal scope of MD simulations, the ion-induced modifications that would lead to these phenomena can be observed and characterized up to patterning-relevant fluences. This final point is a key emphasis; statistical studies of single-ion impacts [54] are insufficient to show how a large number of successive impacts can cause dramatic changes in the structural and chemical landscape of the irradiated surface.

To address these knowledge gaps, two sets of simulations were carried out on the Blue Waters supercomputer operated by the National Center for Supercomputing Applications (NCSA) [111]. To address the former question, a surface with a prescribed compositional depth profile based on initial analysis of experimental data [30] was created with a 100 × 100 nm^2 size and bombarded with 500 eV Kr^+ ions. To address the latter question, an initially-pristine 25 × 25 nm^2 GaSb surface was bombarded with 500 eV Ne^+, Ar^+, and Kr^+ ions up to fluences approaching 10^{16} cm^{-2}. In each

set of simulations, the GaSb surface showed clear compositional changes due to ion-induced instabilities, including the emergence of laterally-distributed compositional phases which could provide the physical basis or "seeds" for nanopattern formation.

3.2 Molecular dynamics simulations of the effects of the as-irradiated GaSb compositional depth profile

3.2.1 Design of simulations

MD simulations were carried out with the LAMMPS code package [84] to study the effects of the compositional depth profile on the evolution of ion-irradiated GaSb. For these simulations, the chosen conditions were Kr^+ at 500 eV and normal incidence. The choice of Kr^+ was made based on experimental observations of a significantly lower threshold fluence for pattern formation compared to other species (see **Figure 3.1**), suggesting that the ion-induced changes would proceed more rapidly and thus be more easily observed from simulations under these conditions.

The simulation setup is shown in **Figure 3.2** schematically. The simulation box has dimensions of 100×100 nm^2 in the lateral dimensions, and approximately 10 nm in the vertical dimension with various subdivisions of the simulation cell as shown in the figure. The lowest layer of lattice cells is held fixed to represent the boundary between the ion-modified surface and the pristine bulk GaSb. The next two lowest lattice cell layers are controlled by a Berendsen thermostat [112] held at an equilibrium temperature of 300 K to act as a heat sink for the excess energy deposited by incident ions. The remaining layers of GaSb were generated prior to bombardment simulations according to a prescribed compositional profile. The details of this profile and of the surface creation procedure are given later on in **Section 3.2.2**.

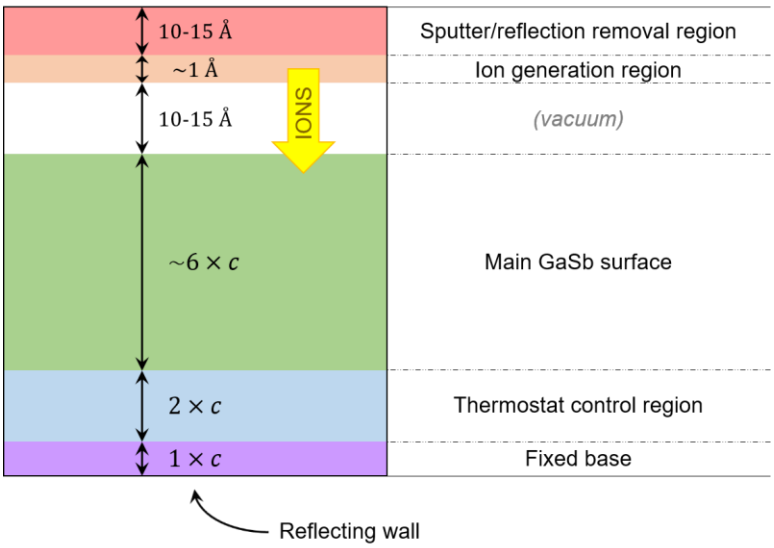

Figure 3.2: Design of simulation schematic showing the vertical divisions of the MD simulation cell. The vertical lattice constant *c* is 0.862 nm and the total simulation cell height is approximately 10 nm.

Ions are generated successively in a thin region above the surface, with enough vacuum space allotted to ensure that the surface does not swell up to such a degree that ions are generated within the surface, and are given a downward velocity corresponding to the chosen ion energy of 500 eV. LAMMPS chooses a dynamic timestep size for each time integration step based on the calculated particle velocities to ensure that no particle is displaced by more than 5 pm in a single integration step. Due to the size of the surface, a mere 5,000 timesteps are allotted between impacts, since the large size of the surface means that successive impacts are rarely close to each other in space[5]. After every 5,000 steps, the position data of all particles is output to a dump file for later analysis.

Prior to these simulations, no single potential had been formulated which considered Ga-Ga, Sb-Sb, and Ga-Sb bonding, all of which are necessary to model a surface with the compositional depth profiles shown in **Figure 3.1**. Previous modeling of GaSb by Norris and coworkers [54] had relied

[5] In simulations over smaller length scales, such as those described in **Chapter 4**, a larger time is needed between impacts to allow the surface to reach an equilibrium state and avoid having successive collision cascades interfere with one another. For a large surface as considered here, a single cascade may resolve over the course of several other impacts located so far away across the surface that no cross-cascade interaction occurs, allowing a shorter time between impact events to be used for the sake of time-efficiency.

on combining the GaSb potential of Powell [113] for Ga-Sb bonding with a rescaled version of the GaAs potential of Albe [114] to model Ga-Ga and Sb-Sb bonds. Both of these potentials are of the Abell-Tersoff form [115] and are thus compatible, however the rescaling by Norris only affected two parameters and thus gave a poor estimate for the density of the pure-Sb phase. This was dismissed by those authors with the logic that pure-Sb phases would not be expected to form in their simulations, which was not the case for the present work. Therefore, a revised approach to the interatomic potential was taken, which is described in detail below.

Within the LAMMPS codebase [84], this potential is expressed in the form:

$$V_{ij}^{Tersoff}(r_{ij}) = f_C(r_{ij})\left[A\exp(-\lambda_1 r_{ij}) - b_{ij}B\exp(-\lambda_2 r_{ij})\right] \tag{3.1}$$

$$f_C(r) = \begin{cases} 1, & r < R - D \\ \frac{1}{2}\left[1 - \sin\left(\frac{\pi(r-R)}{2D}\right)\right], & R - D < r < R + D \\ 0, & r > R + D \end{cases} \tag{3.2}$$

The four parameters, $\{A, B, \lambda_1, \lambda_2\}$ describe the two-body interaction, while the cutoff function f_C smoothly brings the potential to zero at a finite distance for computational tractability. The three-body effects, which modify the two-body interaction based on the three-particle bond angle, are contained in the body term b_{ij}:

$$b_{ij} = \left(1 + \beta^n \zeta_{ij}^n\right)^{-\frac{1}{2n}} \tag{3.3}$$

$$\zeta_{ij} = \sum_{k \neq i,j} f_C(r_{ik}) g(\theta_{ijk}) \exp\left[\lambda_3^m (r_{ij} - r_{ik})^m\right] \tag{3.4}$$

$$g(\theta) = \gamma_{ijk}\left\{1 + \frac{c^2}{d^2} - \frac{c^2}{[d^2 + (\cos\theta - \cos\theta_0)^2]}\right\} \tag{3.5}$$

The Tersoff potential is smoothly connected to a ZBL potential [58], V_{ij}^{ZBL}, to describe close-range collisional interactions by way of a Fermi-like switching function, f_F:

$$V_{ij}^{net}(r_{ij}) = [1 - f_F(r_{ij})]V_{ij}^{ZBL} + f_F(r_{ij})V_{ij}^{Tersoff} \tag{3.6}$$

$$V_{ij}^{ZBL}(r_{ij}) = \frac{1}{4\pi\epsilon_0}\frac{Z_1 Z_2 e^2}{r_{ij}}\phi_{ZBL}\left(\frac{r_{ij}}{a}\right) \tag{3.7}$$

$$f_F(r) = \frac{1}{1 + \exp[-A_F(r - r_C]} \tag{3.8}$$

Note that the ZBL screening function, $\phi_{ZBL}(x)$, is omitted since it contains no free parameters.

The potential parameters used are summarized in **Table 3.1** below. The parameters for Ga-Ga and Ga-Sb interactions are the same as in their cited sources. For Sb-Sb interactions, the As-As potential of Albe et al. [114] was adapted, since As and Sb share the same rhombohedral crystal structure, and the four two-body terms $A, B, \lambda_1, \lambda_2$ were rescaled accordingly. Specifically, these parameters were fit to provide the best estimate of the Sb dimer energy (3.11 eV) [116], lattice constants (4.31 Å and 11.27 Å) [117], and cohesive energy (2.72 eV) [118]. The resulting values after fitting these parameters were: dimer energy 3.11 eV, lattice constants 4.32 Å and 11.19 Å, and cohesive energy 2.716 eV, all within the bounds of reasonable uncertainty. The three-body terms from [114] were left alone since they primarily determine the crystal structure, which is almost identical between As and Sb.

To confirm the validity of the adjusted potential for Sb-Sb interactions, the lattice constants and cohesive energies of several Sb crystal structures were computed with the modified coefficients. The results of these calculations are shown in **Table 3.2**, and show that the rhombohedral structure (α-Sb) is the most stable with a cohesive energy of 2.72 eV/atom. The next most-stable structure is

predicted to be simple-cubic (sc-Sb) with a cohesive energy of 2.70 eV/atom. Note that since sc-Sb is slightly more dense than α-Sb, it may become the preferred lattice structure under high pressures.

Table 3.1: Parameter sets for the Tersoff/ZBL hybrid potential used to model GaSb in LAMMPS. Parameters for the Sb-Sb interaction in bold font are changed from their original values in [114].

Parameter	**Ga-Ga**	**Ga-Sb**	**Sb-Sb**
Two-body parameters			
A (eV)	535.199	2521.76	**22752.7**
B (eV)	410.132	544.904	**412.687**
λ_1 (Å^{-1})	1.60916	2.50245	**3.31331**
λ_2 (Å^{-1})	1.44970	1.74517	**1.56288**
Three-body parameters			
m	1	3	1
γ	0.007874	1.0	0.455
λ_3 (Å^{-1})	1.846	0.968688	3.161
c	1.918	1.20875	0.1186
d	0.75	0.839761	0.1612
$\cos(\theta_0)$	-0.3013	-0.427706	-0.07748
n	1.0	4.60221	1.0
β	1.0	0.363018	1.0
Cutoff parameters			
R (Å)	2.95	3.5	3.6
D (Å)	0.15	0.1	0.2
ZBL parameters			
Z_1	31	31	51
Z_2	31	51	51
r_C (Å)	1.2	1.2	1.2
A_F (Å^{-1})	12.01	12.01	12.01

Table 3.2: Calculated properties for several crystal structures of Sb calculated with the modified Tersoff potential described in the main text. Note that listing a crystal structure here does not necessarily imply that it is expected to be observed in experiments.

Lattice structure	**Lattice constants (Å)**	**Cohesive energy (eV)**	**Atomic density (cm^{-3})**
Diamond cubic (dc-Sb)	$a = 6.98$	2.27	2.35×10^{22}
Rhombohedral (α-Sb)	$a = 4.32, c = 11.19$	2.72	3.32×10^{22}
Simple cubic (sc-Sb)	$a = 3.09$	2.70	3.39×10^{22}
Body-centered cubic (bcc-Sb)	$a = 3.70$	2.44	3.95×10^{22}
Face-centered cubic (fcc-Sb)	$a = 4.69$	2.57	3.88×10^{22}

As additional validation of the MD potential, the sputtering yields were calculated using essentially the same procedure as described above to simulate 349 consecutive 500 eV Kr^+ ion impacts into GaSb(110), reaching a fluence of 3.5×10^{14} cm^{-2} (low enough that no significant surface

modification occurred). The total sputtering yield was found to be 2.3 ± 0.1 atoms/ion, with partial yields of 1.1 ± 0.1 atoms/ion for Ga and 1.2 ± 0.1 atoms/ion for Sb. The observation of preferential Sb sputtering, if only by a slight amount, is in decent agreement with experimental results [107]. This represents a significant improvement over the results obtained from the potential of Norris and coworkers, which predicted significant preferential sputtering of Ga over Sb for 250 eV Ar^+ irradiation [54].

For data analysis, OVITO [119] was used for visualization and basic analysis features such as coordination analysis and cluster identification/selection. This was supplemented with self-written codes to calculate e.g. the mean square displacement of the atoms across numerous snapshots.

3.2.2 Construction of the GaSb surface with an altered compositional depth profile

As incident ions modify the surface compositional depth profile, it is reasonable to expect that the structure of the surface will also change in response to compositional changes. Thus, to construct a surface of altered composition for the MD simulations, simply replacing atoms to obtain a desired stoichiometry is insufficient, and a more complex approach is required. To achieve this, a surface with the desired compositional profile was created by starting from an initial crystalline GaSb base and successively adding layers of altered stoichiometry to the top of the surface. Each layer was heated and quenched to mimic the ion-damaged GaSb surface that would exist in the actual experimental scenario. The composition and thickness of each layer is shown in **Figure 3.3** along with the experimental data on which the simulated surface was based.

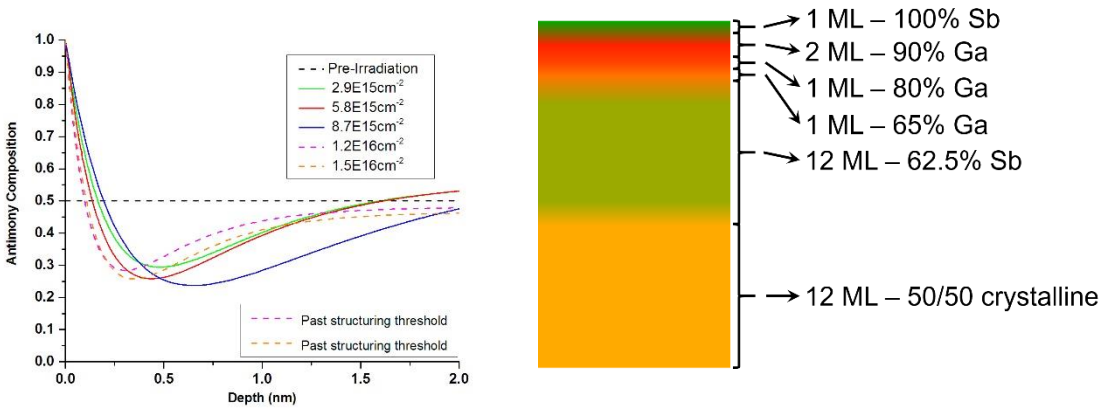

Figure 3.3: (a) Experimental depth profile obtained from absolute analysis of ARAES data for 500 eV Kr^+ irradiation of GaSb; **(b)** Schematic of the compositional profile used to construct the MD simulation cell, which was based on the experimental data in **(a)**. Note that 1 ML = 1 monolayer = 0.22 nm.

The procedure for creating a single layer is as follows: first, atoms are created in the volumetric region corresponding to the active layer being created, with the desired compositional ratio. For the 62.5% Sb-enriched layer, these atoms are created with an initial GaSb crystalline ordering, while for succeeding layers the atom placement is random within the layer region. All atoms in layers beneath the active layer are held fixed, and reflecting walls are created at the top and bottom to confine the hot atoms in the active layer (the lateral boundaries are periodic).

Once this is done, the active layer atoms are considered to be an NVT ensemble and are given velocities with a Maxwellian distribution corresponding to a high temperature. This temperature must be fairly high in order to melt the solid, but care must be taken that the temperature is not so high that the Ga and Sb atoms are driven to completely phase-separate due to their different thermodynamic properties combined with the large pressure in the active layer. In practice, the correct temperature is found through trial and error.

The simulation is run for some time to allow the atoms to mix completely, and then the temperature of the active layer is instantly reset to 300 K to induce immediate solidification. This is in contrast to the methodology used previously for Si amorphization (**Chapter 2**), where the sample is slowly cooled. For compound materials like GaSb, this approach does not work because the disparate melting temperatures of the two components can lead to undesirable precipitation, which would not realistically reflect the nature of the ion-damaged surface. Once the active layer has spent some time at 300 K to equilibrate, it is slowly cooled to 77 K to further allow the resulting layer structure to "settle" into its stable configuration. Once this is finished, the thermodynamic constraints and reflecting walls are removed, and the surface is frozen and considered to be part of the "bulk" from then on. This procedure is repeated until all layers shown in **Figure 3.3** are created.

Once the complete surface is created, the entire surface is relaxed at 300 K for a long time in order to relieve the interfacial stresses between layers. This is done by holding the bottom layer of the simulation cell fixed, and the few layers above this are treated by a Berendsen thermostat, just as in a normal bombardment simulation. In the very early stages of this relaxation, it is necessary to add a reflecting wall just above the surface to prevent the top layers from immediately exploding apart due to the interfacial stresses. This wall is raised slightly after some time, and then removed completely once it is no longer necessary.

A snapshot of the resulting final product from this surface creation procedure is shown in **Figure 3.4**. For the initial surface creation, only a 25 × 25 nm^2 surface area was created, enabling the surface to be prepares on a local computing cluster before being transferred to Blue Waters for the main simulations. To create the final 100 × 100 nm^2 surface, this smaller surface was simply duplicated four times in each lateral dimension (for a total of 16 copies).

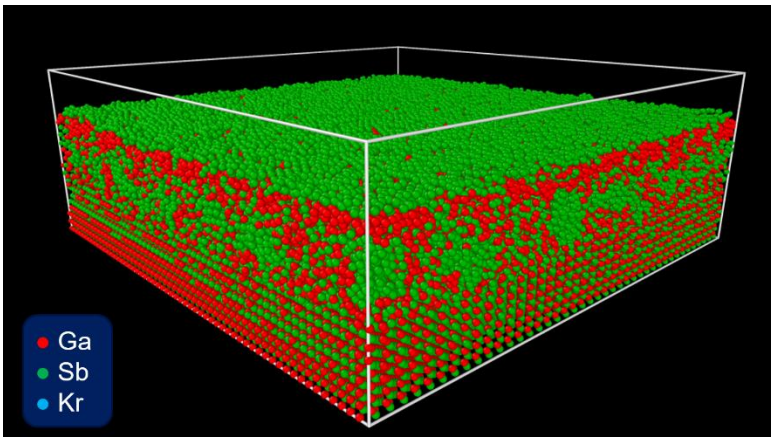

Figure 3.4: Render of the initial surface (25 × 25 nm^2) created for bombardment studies on Blue Waters, following the surface creation procedure described in the main text.

Even for this initial surface, prior to any ion bombardments, it is clear that the altered composition has led to changes in the lateral compositional distribution of the surface. In particular, in the Sb-enriched (Ga-enriched) region, the atoms in that region have readily phase-separated into 50-50 GaSb phases and pure phases of Sb (Ga). This is in agreement with the behavior expected from the GaSb phase diagram [7], lending some initial support to the proposed phase-separation mechanism of nanopattern formation.

In concluding this section, it should be noted that the data shown in **Figure 3.4** contain a minor error, as some of the thermodynamic controls during the relaxation steps were not reset between those steps. While correcting this error does cause some change in the initial surface, the results obtained using the surface of **Figure 3.4** are not significantly affected, as will be discussed below.

3.2.3 Crystallization behavior of phase-separated Sb clusters

Figure 3.5 shows cross-sectional snapshots of the ion-irradiated GaSb at various fluences, including the initial state. It is immediately apparent that even within the very short fluence interval of 1.9 × 10^{13} cm^{-2}, the Sb atoms in pure-Sb clusters have self-arranged into crystalline lattice

structures. This even appears to be the case at the very surface, where what was originally a single monolayer of Sb atoms has self-arranged into crystalline terrace structures, rather than remaining in a disordered state or forming a two-dimensional lattice. By contrast, the Ga atoms in pure-Ga clusters appear to have remained largely amorphous. At higher fluences, the situation remains largely unchanged, and in fact it appears that the incident ions have had a minimal effect on the compositional structure of the surface.

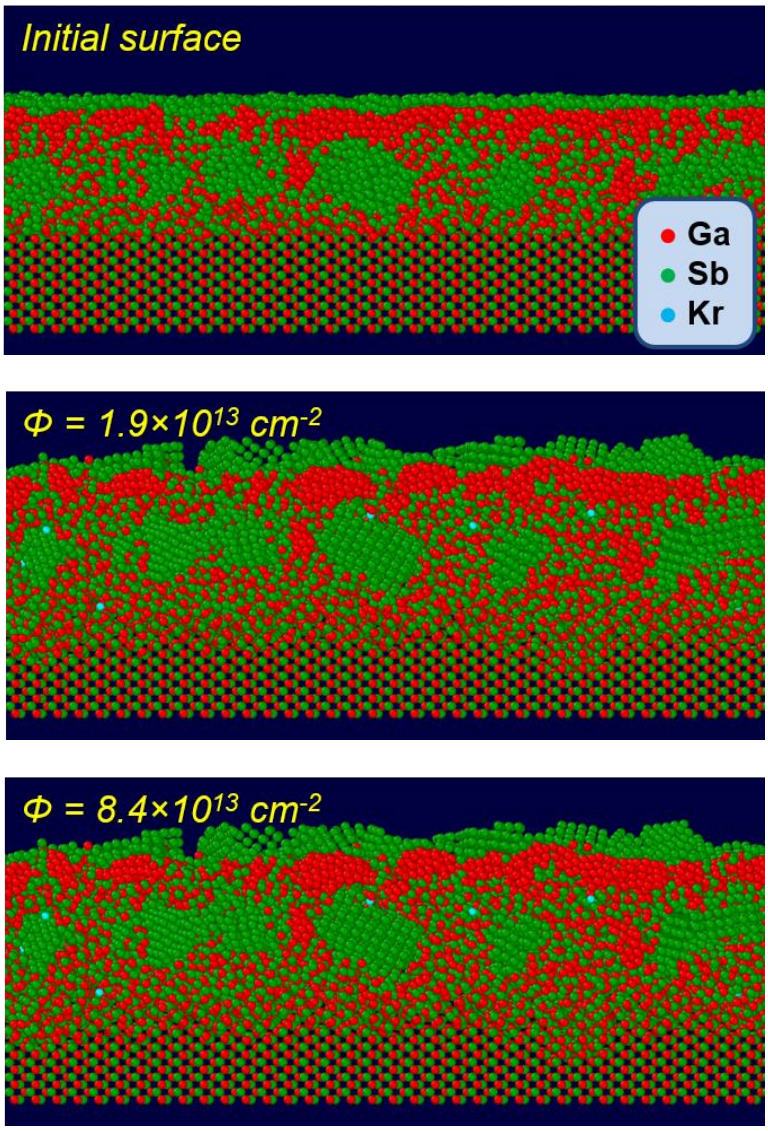

Figure 3.5: Cross-sectional snapshots of the ion-bombarded GaSb surface from the initially-altered compositional depth profile at indicated differential fluences, Φ.

To characterize the crystallization of Sb clusters (and non-crystallization of Ga clusters), the radial coordination of the Sb and Ga atoms in single-element clusters can be computed with OVITO. **Figure 3.6** shows this data for Sb and Ga in clusters, respectively. The presence and growth of several pronounced peaks in the Sb-Sb correlation pattern indicate a transition from amorphous to crystalline, while the lack of many distinct peaks and near flatness of the Ga-Ga coordination plot at large distances indicates a lack of long-range order characteristic of amorphous surfaces. Interestingly, for the Sb-Sb coordination number, significant change occurs even for a fluence as low as 10^{12} cm^{-2}, by which point only one ion impact has occurred, on average, for every 100 nm^2 of surface area. At such low energies as 500 eV, this is far too few impacts to be directly responsible for the degree of change observed in these Sb clusters, implying that the crystallization may not be directly ion-induced.

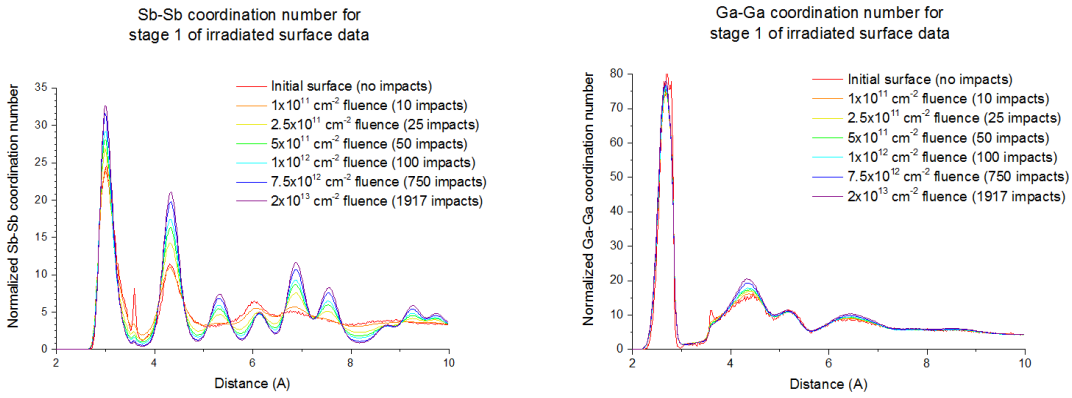

Figure 3.6: Evolution of the coordination number with respect to ion fluence for Ga-Ga and Sb-Sb interactions during the irradiation simulations.

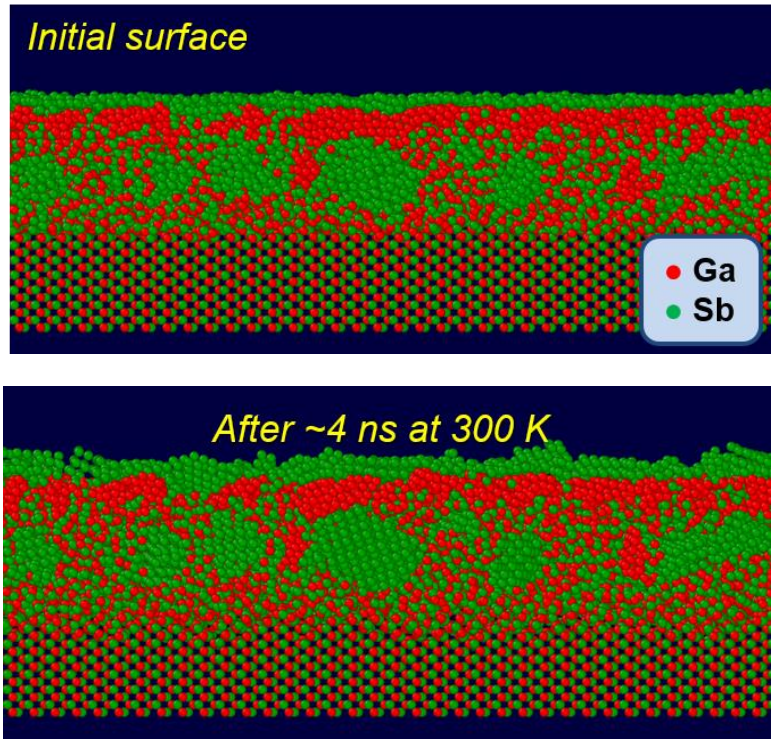

Figure 3.7: "Control" snapshots with no ion bombardment of the initial altered-composition GaSb surface initially, and after 4 ns of evolution with no external influence on the surface.

In order to allow for effects of the ion irradiation to be separated from any other effects of the altered surface composition which might arise over longer time scales than the surface preparation, a "control" simulation was also performed. In this case, "control" simply meant that no ions were generated, and the surface was allowed to evolve by itself for a time of ~4 ns. Snapshots of the results are shown in **Figure 3.7**, and coordination analysis of the results for this simulation are shown in **Figure 3.8**.

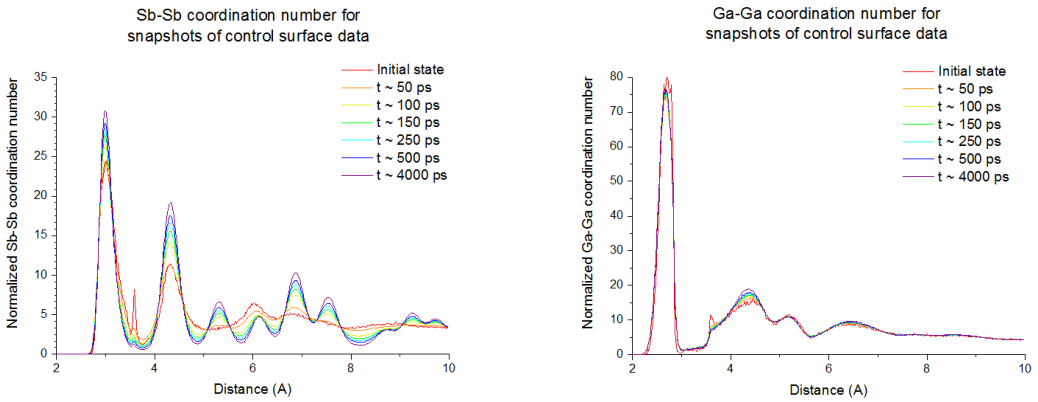

Figure 3.8: Evolution of the coordination number with respect to time elapsed for Sb-Sb and Ga-Ga correlation over the course of the "control" simulations without ion bombardment.

As before, Sb atoms in clusters are clearly observed to self-arrange into crystalline lattices while Ga atoms in clusters remain in an amorphous configuration. Indeed, when compared to the results from the ion-bombarded samples in **Figures 3.5** and **3.6**, the results are nearly identical aside from the lack of Kr^+ ions implanted in the surface. This provides a strong indication that the crystallization of the Sb clusters is not directly-ion induced, but is in fact an intrinsic material response to the ion-induced compositional depth profile and the consequent phase separation in the non-stoichiometric regions of the surface. This intuitively makes sense, since the fluence of ions reached in these simulations is less than 10^{14} cm^{-2}, well below the amount of incident ions which would be expected to cause significant change and evolution of the surface. Therefore, it would be a logical stretch to expect that the incident ions alone would cause such a uniform change across an entire surface in any case.

Interestingly, the observation of Sb crystallization in irradiation-modified GaSb is not a new phenomenon. In fact, this has been observed experimentally in studies of GaSb core-shell nanowires formed by ion irradiation [120], albeit at much higher energies (1 MeV Au^+). Results from these experiments are shown in **Figure 3.9** as a visual basis of comparison with the simulation results. In the experiments, it was found that the resulting nanowires consisted of crystalline cores

of primarily Sb surrounded by amorphous shells. In the experimental studies, the separation of Ga and Sb was attributed to the low sublimation energy of Sb combined with rapid Ga diffusion to and oxidation at the very surface. Here, however, this cannot be the case because the Sb clusters are formed beneath the surface, and instead phase separation due to the altered composition is a more plausible explanation.

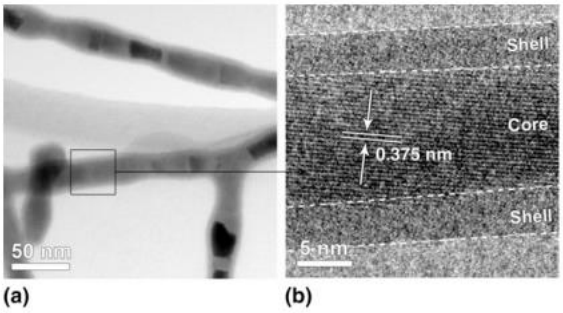

Figure 3.9: TEM analysis of a GaSb nanowire formed by ion bombardment and subsequent annealing [120]. The core of the nanowire consists mostly of crystalline Sb, while the outer shell consists of amorphous material.

The marked difference between the crystalline Sb clusters and the amorphous Ga clusters may bear some resemblance to the significant difference in mobility and diffusivity between the two species. It has been found experimentally [110] and from density functional theory (DFT) [121] that the diffusivity of Ga in GaSb is orders of magnitude higher than that of Sb. This agrees with the difference in structure between clusters of each material, since Ga in an amorphous cluster is much less rigidly bound and more easily given mobility than Sb in a rigid crystalline lattice. However, further detailed study is required to confirm this correlation between the structure of the Ga and Sb clusters and their respective component diffusivities. While a fair amount of DFT studies [121–123] support the enhanced diffusivity of Ga in GaSb, all studies thus far have been in the context of a near-equilibrium, crystalline solid, rather than the ion-damaged, highly-amorphous solid considered in the present simulations.

Before moving on from these results, the note about minor thermodynamic errors from **Section 3.2.2** must be revisited. The results of the "control" simulation show that a "reset" of the thermodynamic controls, inherent in a completely new simulation, frees up some degree(s) of freedom for the surface to evolve and show the Sb cluster crystallization. In fact, the surface creation procedure was revised to ensure that the thermodynamics were completely reset between relaxation stages, and the same crystallization behavior was observed. However, since the incident ions had a minimal effect, if any (as evidenced by the similarity between the irradiated and "controlled" surfaces), the net effect of this on the results is minimal. In fact, the error in this case has allowed the crystallization behavior to be characterized with respect to elapsed time, in **Figure 3.8**.

In any case, the present simulations, while they have provided significant insights into the nature of the altered compositional depth profile and its effects on the surface, have not shed much light on the question of how the incident ion flux drives the surface evolution. In particular, the question of how the depth profile and attendant single-element cluster actually are formed remains open. The simulations in the following section try to address this open question.

3.3 Structural and compositional evolution of pristine GaSb under ion bombardment

3.3.1 Design of simulations

MD simulations were conducted on Blue Waters to study 500 eV ion irradiation of initially-pristine, 50/50 crystalline GaSb(110) to fluences of 7.5×10^{15} cm^{-2}. Experimentally, the ion species has been observed to have a significant effect on the surface evolution [29,30], and therefore simulations were run for Ne^+, Ar^+, and Kr^+ ions to study these effects. The simulation methodology was mostly

the same as that used in the previous section, described in **Section 3.2.1** and **Figure 3.2**, but a few changes were made due to the different nature of these simulations.

The surface size was reduced to only 25 × 25 nm^2, compared to the 100 × 100 nm^2 size used previously. On one hand, this was necessary to reduce the number of atoms being simulated so that the desired high fluences could be reached with the available computational resources on Blue Waters. On the other hand, experience from the previous simulation had shown that the salient features of the lateral compositional distribution would have characteristic size and spacing on the order of ~5 nm, at most. Thus, a smaller surface was not expected to obscure any significant features arising from the high-fluence ion bombardment.

The reflecting wall at the bottom of the simulation box (see **Figure 3.2**) was eliminated, and instead particles reaching the bottom of the simulation box were simply removed entirely. While it could be argued that this is a slightly more physical boundary condition compared to the reflection used previously, the choice is largely arbitrary and has little if any effect on the course of the overall simulation.

Finally, due to the high fluence and correspondingly-higher amount of sputtered material compared to the previous simulations, additional layers of GaSb(110) were added to the bottom of the simulation cell between stages of the simulation (each simulation was broken into several stages due to the 48-hour wallclock limit for a single job submission on Blue Waters). This approach was preferred to using a larger initial thickness in order to improve the simulation efficiency by limiting the total number of atoms being simulated during a given stage. Whenever a new layer of atoms was added, the fixed layer and thermostat layer positions were adjusted downwards accordingly, so that the lowest 0.86 nm of atoms were always held fixed, and so that the thermostat layer was always immediately above the fixed layer.

3.3.2 Formation of Sb protoclusters by prompt ion effects

Figure 3.10 shows the initial GaSb surface, and the final GaSb after 500 eV Kr^+ bombardment to a fluence of 7.5×10^{15} cm^{-2}. As is usual for ion irradiation of semiconductor surfaces, the GaSb has been completely amorphized except for the fixed layers at the bottom representing the amorphous-crystalline interface. However, there is no discernable compositional depth profile in the snapshot of the final surface. Attempting to calculate the approximate compositional depth profile by dividing the surface into horizontal layers and finding the ratio of Ga and Sb atoms in each layer confirms the visualization, as no layer varies by more than 2-3% from stoichiometric 50/50 GaSb. The lack of a prompt ion-induced compositional depth profile indicates that there must be long-timescale mechanisms (e.g. asymmetric diffusion or stress-driven viscoelastic flow) active during experiments, which are beyond the timescales accessible with MD simulations, that drive the compositional evolution of the surface.

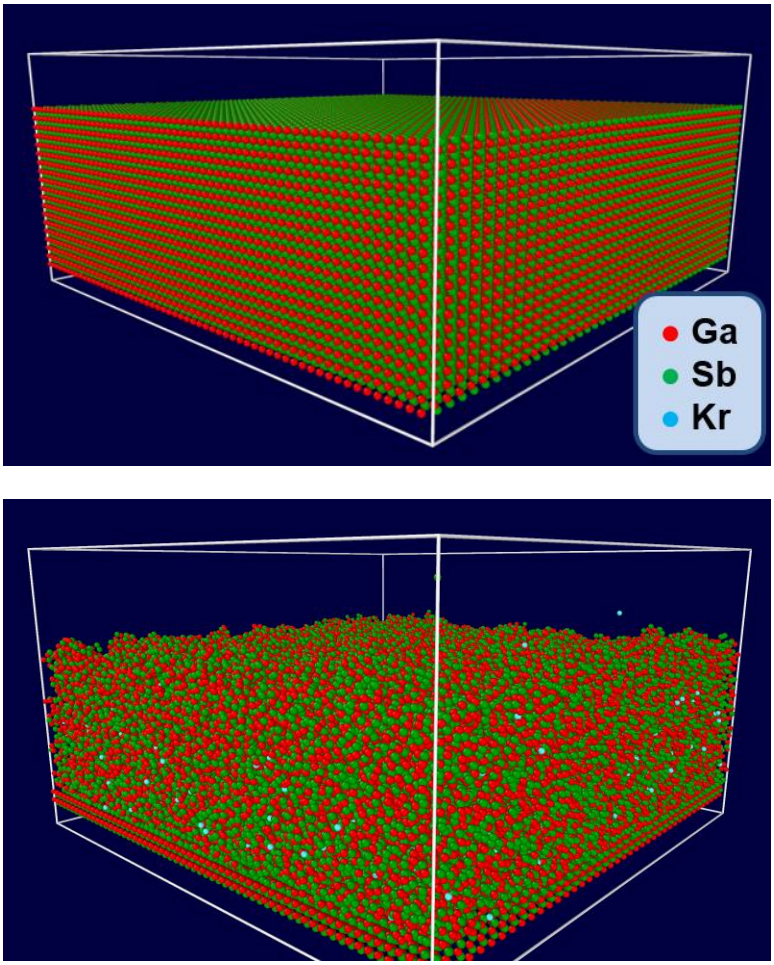

Figure 3.10: Perspective snapshots of the GaSb surface: **(top)** initially, prior to ion bombardment; **(bottom)** after irradiation with 500 eV Kr^+ to a fluence of 7.5×10^{15} cm^{-2}.

Despite the lack of a "global" ion-induced compositional depth profile, the simulated surfaces still undergo compositional changes due to the ion bombardment. **Figure 3.11** shows the same final surface as in **Figure 3.10** (500 eV Kr^+ bombardment), but with the snapshot data filtered to only show clusters of Ga or Sb, alternately. Interestingly, while a large number of Sb clusters are formed, often containing a dozen or more atoms, very few Ga clusters are formed and almost all of them are very small, usually containing ≤ 6 atoms. It should be noted that these clusters cannot be formed by the same phase separation mechanism as discussed previously for the altered-composition GaSb surface, since in this case there is no significant compositional depth profile to induce such a phase separation effect. To distinguish the clusters shown in **Figure 3.11** (and following snapshots) from

the clusters discussed in **Section 3.2.3**, and also because the Sb clusters are smaller and more numerous than those formed in the previous study, the term "protocluster" will be used from this point forth to refer to those clusters formed by prompt ion effects in the current set of simulations.

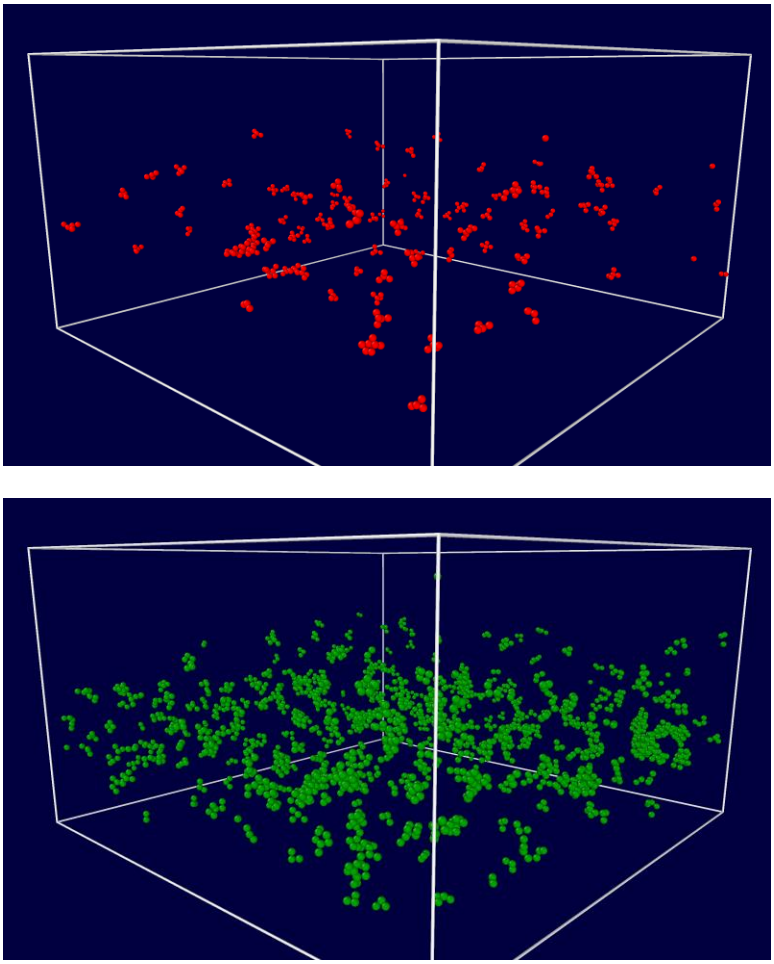

Figure 3.11: Snapshots of the surface in **Figure 3.10** for 500 eV Kr^+ irradiation to 7.5×10^{15} cm^{-2}, filtered in OVITO to only show clusters of Ga **(top)** and Sb **(bottom)**. Ga atoms are in red, while Sb atoms are in green.

In all simulations (i.e. for all ion species), no significant preferential sputtering of Ga was observed. If anything, usually the sputtering yield of Sb was usually higher than that of Ga if only by a slight amount. Thus, it is at first curious to see the vast difference in protocluster formation of Ga versus that of Sb, since this disparity would imply that stoichiometry of Ga and Sb is not preserved. In other words, the question is raised: Where do the extra Ga atoms go? **Figure 3.12** answers this question by showing a snapshot of the same Sb protoclusters as in **Figure 3.11**, but with the OVITO

filter expanded to include all particles "near" (within ≤ 3.6 Å of) an Sb protocluster. These nearby particles are mostly Ga atoms, which provide a sort of shell (albeit far from completely) around the Sb protoclusters at the interface with the bulk amorphous 50/50 GaSb. This observable "core-shell" structure is reminiscent of the experimental results [120] highlighted in **Figure 3.9**. Furthermore, the Ga shell can be considered as terminating the interface of the bulk GaSb and the Sb protoclusters. In this sense the Ga shell formation could be considered analogous to the surface enrichment of Ga that has been observed experimentally for GaSb even at low fluences or before ion bombardment [29,30,107], in the sense that both the surface and the boundary between amorphous GaSb and pure Sb protoclusters are classified as interfaces and that Ga preferentially settles at such interfaces.

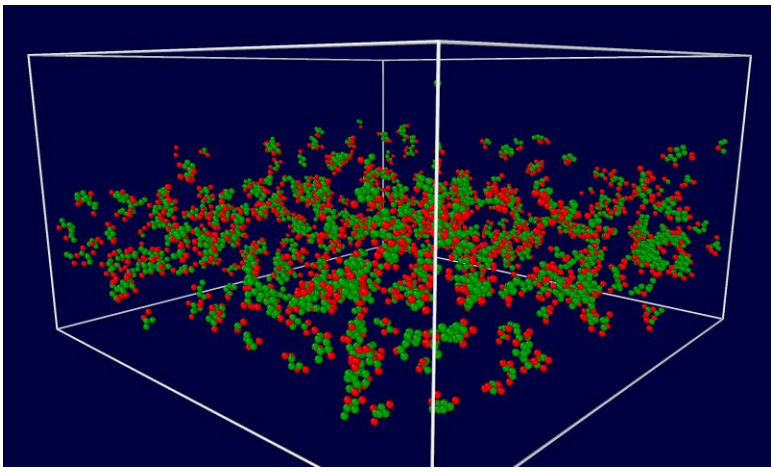

Figure 3.12: Snapshot of the Sb clusters (**Figure 3.11**) after 500 eV Kr^+ irradiation to 7.5×10^{15} cm^{-2}, with the OVITO filter expanded to show all particles near those clusters (within 3.6 Å). Ga atoms are in red, while Sb atoms are in green.

To gain better understanding of the protocluster formation, the tendency of various incident ion species to induce protocluster formation was characterized. **Figure 3.13** shows all Sb protoclusters formed from 500 eV Ne^+ irradiation of GaSb to a fluence of 7.5×10^{15} cm^{-2}. The Sb atoms shown in the snapshots represent 5.4% of all Sb atoms in the surface, i.e. 5.4% of Sb atoms are members of a protocluster. Two features can be noted which have not yet been observed in the previous discussion. First, the protoclusters show a range of structures, with some exhibiting clear simple

cubic or rhombohedral ordering while others appear poorly-ordered or possibly even amorphous. Second, from the side-view image in **Figure 3.13**, the boundary between the fixed layer of GaSb(110) and the rest of the simulation cell can be visualized easily as some of the deeper protoclusters have formed right up against the boundary. While not a significant issue as only a few protoclusters are formed at this boundary, this could indicate that the simulation cell is not quite deep enough to contain the majority of collision cascades completely.

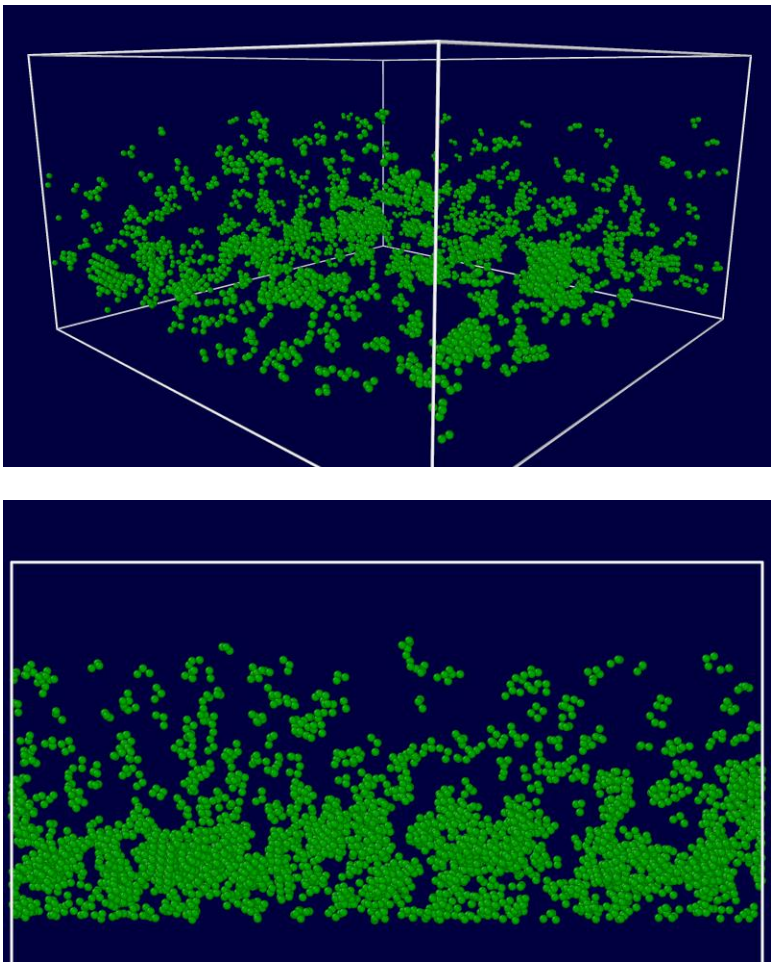

Figure 3.13: Snapshot of Sb clusters from the simulated GaSb surface irradiated with 500 eV Ne^+ to a fluence of 7.5×10^{15} cm^{-2}: **(top)** perspective view; **(bottom)** side view.

Figure 3.14 shows all Sb protoclusters formed from 500 eV Ar^+ irradiation of GaSb to a fluence of 7.5×10^{15} cm^{-2}. The Sb atoms shown in the snapshots represent 5.5% of all Sb atoms in the surface, i.e. 5.5% of Sb atoms are members of a protocluster. Compared to the protoclusters formed

by Ne^+ bombardment, there seem to be fewer protoclusters with crystalline ordering for Ar^+ bombardment, although this is difficult to quantify with certainty. As for the Ne^+ case, the boundary with the fixed layer is clearly seen from the shapes of the deepest protoclusters, suggesting that the simulation cell should be somewhat deeper.

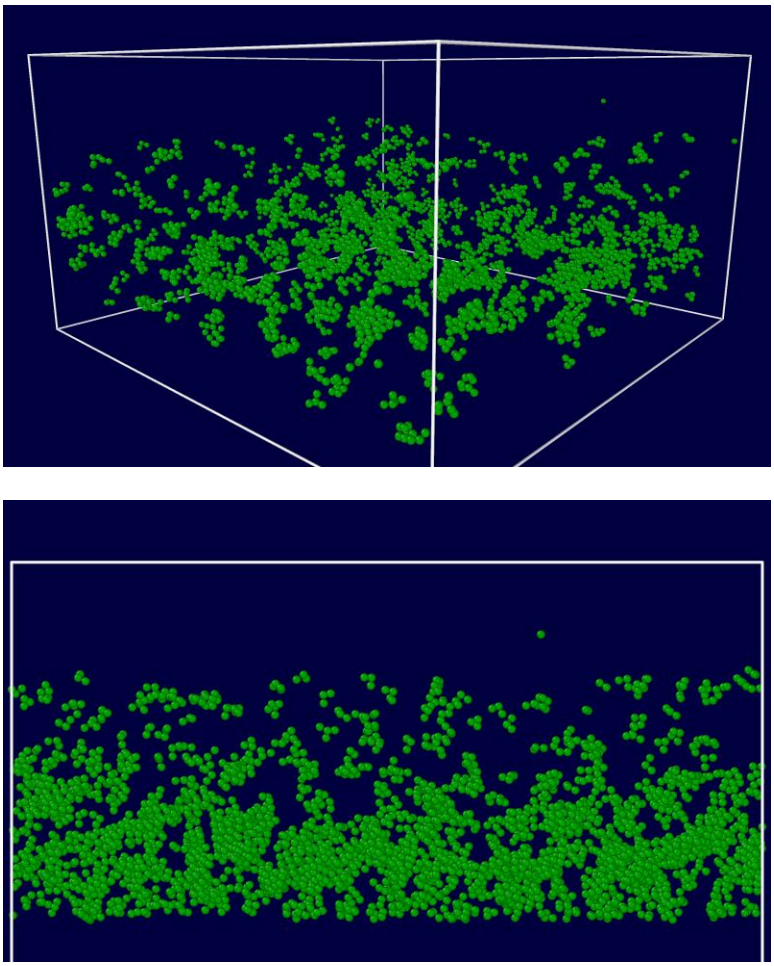

Figure 3.14: Snapshot of Sb clusters from the simulated GaSb surface irradiated with 500 eV Ar^+ to a fluence of 7.5×10^{15} cm^{-2}: **(top)** perspective view; **(bottom)** side view.

Finally, **Figure 3.15** shows all Sb protoclusters formed from 500 eV Kr^+ irradiation of GaSb to a fluence of 7.5×10^{15} cm^{-2}. In a surprising divergence from the Ne^+ and Ar^+ cases, the Sb atoms shown in the snapshots represent only 3.2% of all Sb atoms in the surface, i.e. only 3.2% of Sb atoms are members of a protocluster. There are visibly fewer protoclusters compared to the previous cases, and few of these seem to exhibit any apparent crystallographic structure, which

may be attributable to the smaller average size of these protoclusters compared to the previous examples. Additionally, the average depth of a Kr-induced protocluster appears shallower than for Ne or Ar-induced protoclusters, and there are few if any protoclusters which occur at the boundary with the fixed layer at the bottom of the simulation cell. This is in good agreement with the fact that Kr, being much heavier than Ne or Ar, has a shallower range in GaSb than the lighter ion species. This shallow range may be at least partially responsible for the lower degree of protocluster formation, as a smaller overall volume of the surface would be available in which to form the protoclusters.

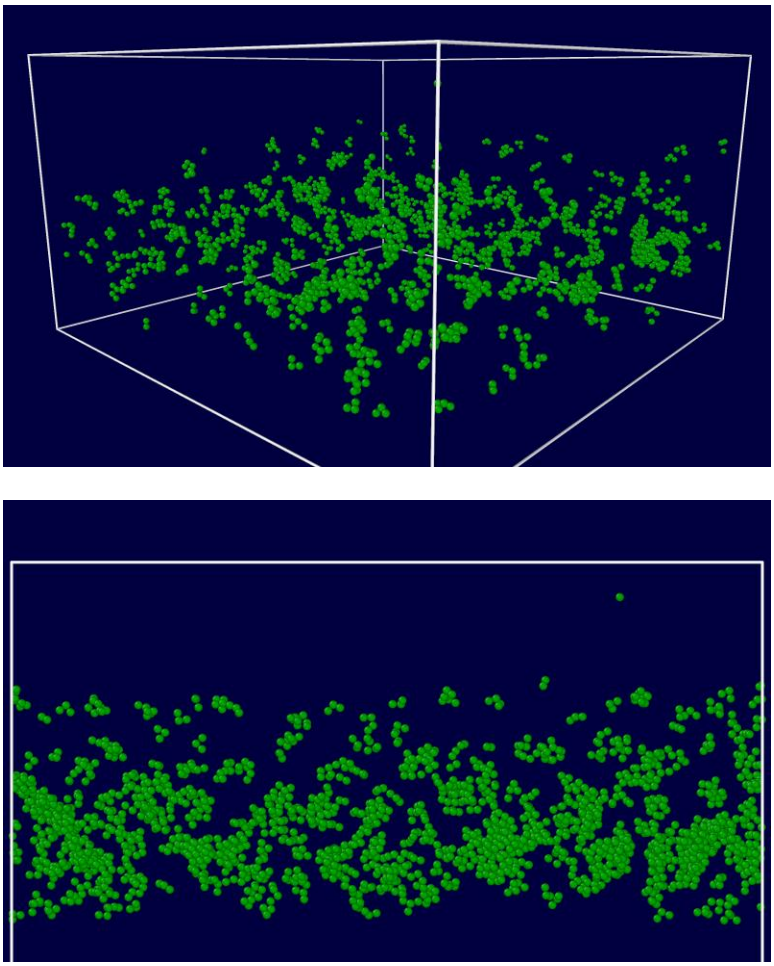

Figure 3.15: Snapshot of Sb clusters from the simulated GaSb surface irradiated with 500 eV Kr^+ to a fluence of 7.5×10^{15} cm^{-2}: **(top)** perspective view; **(bottom)** side view.

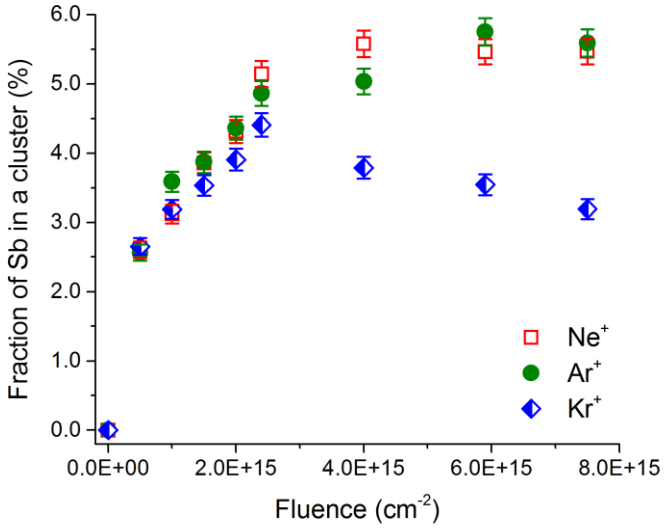

Figure 3.16: Fluence dependence of the fraction of Sb atoms which are part of a cluster, compared for each ion species studied (Ne^+, Ar^+, Kr^+).

The fluence dependence of the protocluster formation, measured as the fraction of Sb atoms which make up part of a protocluster, is compared for all three ion species in **Figure 3.16**. Interestingly, for the early stages of irradiation up to a fluence of around 2.4×10^{15} cm^{-2} the protocluster formation for all three ion species is very similar, although Kr^+ still shows a lower formation rate than the other species. However, for fluences > 2.4×10^{15} cm^{-2} the protocluster formation for Kr^+ actually decreases with increasing fluence! Meanwhile, the other species appear to approach an asymptotic protocluster fraction of ~5.5±0.5%. The origin and meaning of these surprising trends remain unclear, and it is likely that a fuller understanding of the protocluster formation process will be necessary to gain a full understanding of these fluence-dependent phenomena.

While the full mechanics of the protocluster phenomenon may not be understood, the apparent differences between ion species in **Figure 3.16** does show some agreement with experimental observations. From GISAXS experiments [30], the threshold fluence for pattern formation has been found for each of these ion species on GaSb (these values can also be observed in **Figure 3.1**). For

Ne^+ and Ar^+ irradiation, the threshold fluence value was found to be > 3×10^{16} cm^{-2}, however for Kr^+ irradiation the threshold fluence was significantly lower, at only 8.7×10^{15} cm^{-2}, a factor of four times lower than for the lighter ion species. This seems to correlate neatly with the sharp difference between Kr^+ and the lighter ions for the protocluster formation data in **Figure 3.16**, providing a small but encouraging verification of the simulation results.

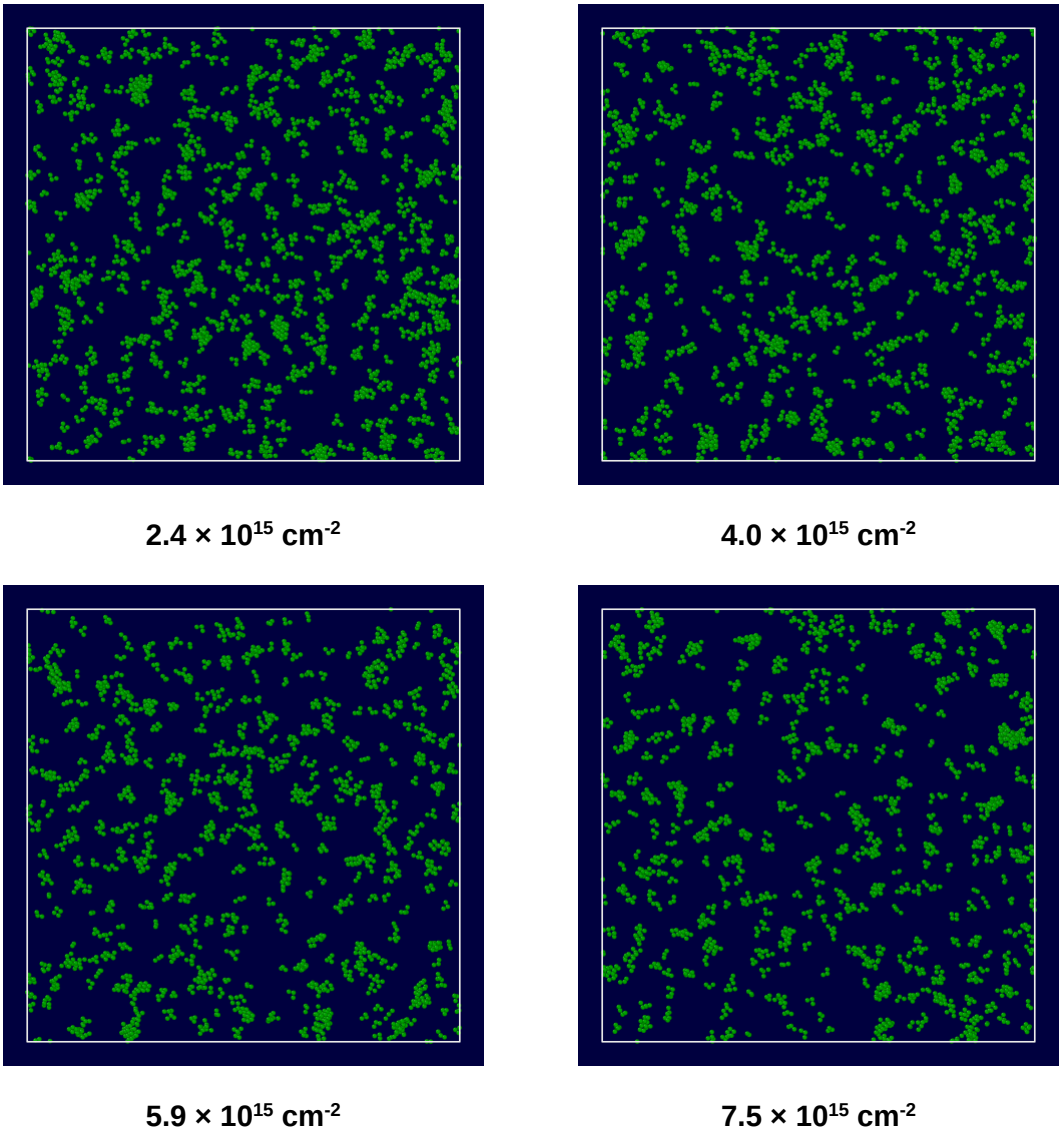

Figure 3.17: Top-down views of Sb protoclusters obtained after 500 eV Kr^+ irradiation of GaSb to several fluences (as indicated on figure).

The fluence-dependent evolution of these protoclusters is worth investigating in some more detail. **Figure 3.17** shows top-down views of all the Sb protoclusters formed by 500 eV Kr^+ irradiation of GaSb for several different fluences. It is intriguing to note that few if any protoclusters appear to survive from one fluence step to the next. In other words, it would seem that the Sb protoclusters are not stable under sustained ion bombardment, perhaps because direct ion impacts on or near the center of a protocluster may shatter it entirely. Alternatively, it could be possible that at least some of the protoclusters are migrating throughout the surface as bombardment continues, but given the significant change in size of clusters in the same local area between fluence steps in **Figure 3.17** this seems rather unlikely.

3.3.4 Candidate mechanisms for Sb protocluster formation

From the data shown thus far, a few different hypotheses exist to explain the formation of the Sb protoclusters. In this section, two hypotheses are advanced, and one is tested by smaller-scale MD simulations of single-impact events.

To motivate the first hypothesis, recall that Ga mobility (i.e. diffusivity) in GaSb is orders of magnitude greater than that of Sb [110,121]. Thus, it is reasonable to imagine that during an ion impact, the ion-enhanced mobility of Ga atoms within the collision cascade would be similarly greater than that of Sb, albeit perhaps not to the same stark degree of contrast. In this case, the Ga atoms would be displaced farther from the center of impact, on average, compared to Sb, leading to a situation where Sb in the core of the cascade volume is surrounded by Ga at the edge of the cascade volume. In other words, the first hypothesis is: *Higher ion-induced mobility of Ga versus Sb leads to the emergence of a Sb core-Ga shell structure during the collision cascade*. This hypothetical mechanism is illustrated schematically in **Figure 3.18**, although it should be noted that this is somewhat simplified. In fact, it is unlikely that a single cascade could lead to a 100%-

Sb core volume since the collision cascade is a stochastic process, and only repeated impacts would lead to a cumulative effect generating the core-shell structure.

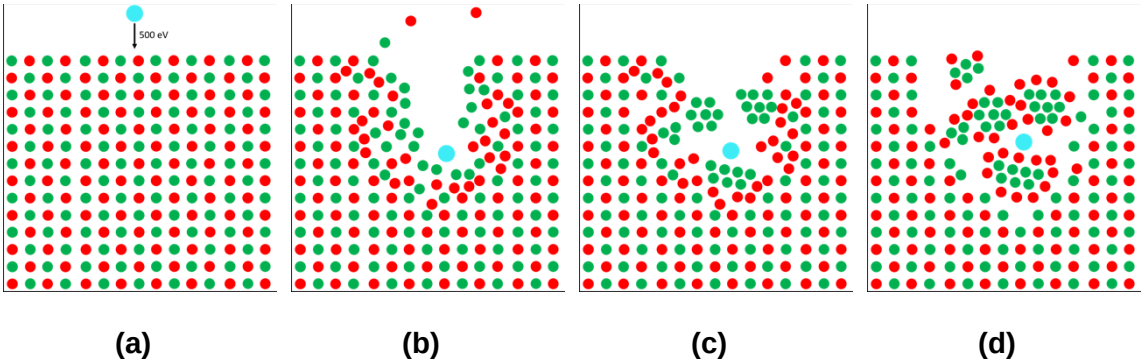

Figure 3.18: Hypothetical mechanism for protocluster formation. **(a)** An incident ion collides with the GaSb surface. **(b)** During the collision cascade, a higher outflux of mobile Ga from the cascade volume compared to Sb leads to **(c)** an excess of Sb in the core of the cascade volume, which will tend to cluster and crystallize, leaving **(d)** the excess Ga to form a partial shell-like structure around the Sb protoclusters.

To test this hypothesis, a moderate number of single-ion impact simulations (500 eV Kr^+) were run on crystalline and amorphous 50/50 GaSb surfaces. These simulations used the same procedure described above, but produced output data files at very close timestep intervals of either one file for every 10 timesteps or one file for every 100 timesteps. This enabled detailed visualization of the single-ion impact cascade dynamics, as well as highly time-resolved calculation of quantities such as the mean square displacement (MSD) of the atoms in the collision cascade. For the sake of addressing this hypothesis, only the latter is needed, and to this end **Figure 3.19** shows the ensemble-averaged MSD of Ga and Sb for the crystalline and amorphous surfaces. In the crystalline case, there are a few peaks in the Ga MSD which are notably greater than the Sb peaks, but these are temporary fluctuations as the Ga atoms "snap back" to their lattice positions for the most part. By the end of a single-ion impact, on average the Ga and Sb atoms have approximately the same MSD. For the amorphous case, the situation is much simpler as the Ga and Sb MSDs remain almost identical for the entire simulated timeframe. Recall that the diffusivity (and thus mobility) of a species is related to its MSD as:

$$D = \frac{1}{6}\frac{\langle MSD \rangle}{\Delta t} \tag{3.9}$$

Thus, it is clear that the ion-induced mobility of Ga and Sb is in fact quite similar over the timeframe of the single-ion impact simulations. Without a significant ion-induced mobility difference, the mechanism proposed in the first hypothesis cannot be responsible for the formation of the core-shell Sb protoclusters.

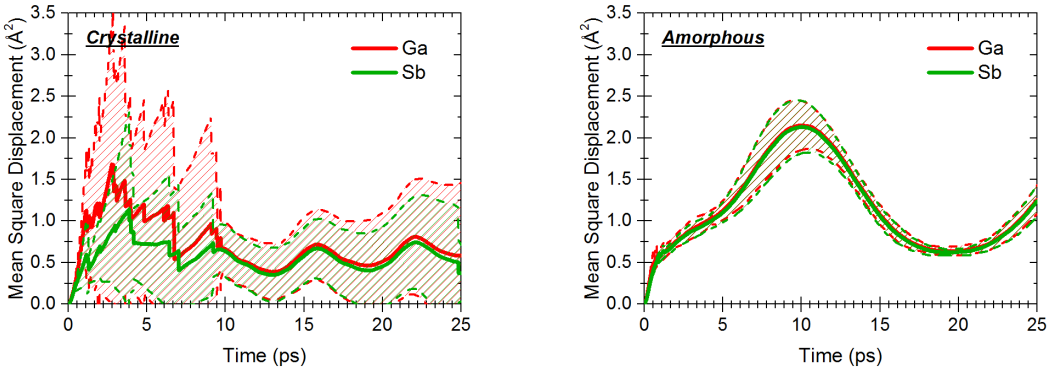

(a) **(b)**

Figure 3.19: Mean square displacement (MSD) of Ga and Sb target atoms over the course of **(a)** crystalline and **(b)** amorphous surface single-ion impact simulations, averaged over all simulations performed. Shaded areas indicate the uncertainty in the calculated MSD values.

The second hypothesis is based on intrinsic thermodynamic properties of Ga and Sb, providing a conceptual connection to the thermodynamic phase separation discussed in **Section 3.2**. Within the thermal spike produced by a single-ion impact, a significant volume is heated to temperatures on the order of 10^3-10^4 K, which is well beyond the melting point of GaSb (985 K) and thus is more than sufficient to induce a temporary liquid state in the cascade volume. As this region cools, Sb can precipitate out of the liquid GaSb mixture due to its melting temperature (904 K) being much higher than that of Ga (303 K). The liquid Ga left behind then eventually solidifies into an amorphous shell around the Sb nanocrystal. In other words, the second hypothesis is: *The higher melting temperature of Sb leads to Sb precipitation out of the melted GaSb from the ion-induced*

thermal spike, forming Sb protoclusters. This kind of mechanism would furthermore allow for protoclusters to form or grow as a result of successive ion impacts in the same locality of the surface, as small groups of Sb atoms which had precipitated out of a previous thermal spike could provide a nucleation or growth seed for additional precipitation from nearby thermal spikes. However, the lack of long-term cluster stability could bring into question the validity of a nucleation or growth process as an explanation for the protocluster phenomenon. In any case, this hypothesis remains to be rigorously tested in any notable capacity.

3.4 Implications for theoretical and computational modeling of compound semiconductor nanopatterning with ion beams

3.4.1 Proposed compositionally-driven mechanisms for nanopattern formation

The MD simulations presented here are not able to cover the complete range of spatio-temporal physical mechanisms which may be activated by ion bombardment of GaSb and other III-V surfaces. However, the information gained from these simulations, in combination with prior knowledge from experimental studies of nanopatterning and other literature sources, can be taken to suggest compositionally-driven mechanisms that may drive ion beam-induced nanopatterning. In particular, the following may be taken as axioms for the present discussion:

- Prior to ion irradiation, a compositional depth profile exists with Ga segregated to the very surface and Sb enrichment up to ~1-2 nm deep in the subsurface [30].
- As bombardment proceeds, the very surface gains Sb but remains Ga-enriched at least up until structure formation occurs [30].
- In regions of altered stoichiometry, lateral phase separation occurs leading to clusters of the enriched component within or alongside 50/50 GaSb (**Section 3.2**).

- In the deeper subsurface (> 2 nm), Sb protocluster formation occurs due to prompt ion effects even if no compositional depth profile occurs at this depth (**Section 3.3**).
- Preferential sputtering from 50/50 GaSb is either nonexistent or slightly weighted towards Sb (ref. [107], **Section 3.2.1**).
- Ga in pristine, *crystalline* GaSb diffuses orders of magnitude faster than Sb [110,121] (whether this holds for amorphized GaSb is certainly a matter for future study).

What is not yet known, from experiments or simulations, is the potential role of mechanisms which might occur on longer timescales such as diffusion or cluster growth, which are necessary to provide a complete understanding of the ion-induced nanopatterning.

For patterning threshold fluences on the order of 10^{16} cm^{-2}, anywhere from 1-10 nm thickness of surface material will be removed by ion-induced sputtering erosion. This means that the initial depth profile before the ion beam is turned on will be quickly destroyed unless some mechanism is active to continually re-form it as the surface recedes. While preferential sputtering has been proposed as a mechanism to maintain the very surface Ga enrichment [107], this by itself would not be sufficient to maintain the subsurface Sb enrichment seen from the experimental depth profiles in **Figure 3.1**[6]. In this case, it seems probable that the Ga enrichment at the very surface is supported in part or in total by fast preferential diffusion of Ga from the subsurface, which accumulates at the very surface due to the Gibbsian segregation observed even prior to irradiation.

[6] The observant reader may note that while the relative Sb composition at ~0.5 nm depth is almost always greater compared to that at the terminal 2 nm depth in **Figure 3.1**, it does not always rise past or in some cases even to 50%. However, the fitting procedure used in this analysis does not assume a terminal boundary condition of 50% composition as the depth becomes arbitrarily large [30], as would be expected physically. In light of this, it is reasonable to judge that "if the terminal composition were 50% for arbitrarily large depth, then the compositional depth profile in the near subsurface would be Sb-enriched", in lieu of a more comprehensive quantitative analysis of the experimental data.

The ion-induced protoclusters can serve as initial Ga sources, in a sense. It has already been shown (**Figure 3.12**) that the formation of Sb protoclusters leads to the collection of excess Ga at the interface between Sb and GaSb. In order to maintain the diffusion current, excess Ga from this interface would be driven into the bulk GaSb and ultimately towards the surface. Meanwhile, the vacancies left at the Sb/GaSb interface would accept Sb atoms from the nearby GaSb, providing not only a growth mechanism for the Sb protoclusters but also a continuing source of excess Ga to maintain the surface enrichment. Note that in contrast to the MD simulations in **Section 3.3**, which reached fluences of 7.5×10^{15} cm^{-2} in a "real-time" interval of only ~1 μs, for a real system with the same surface area (625 nm^2) and a nominal ion beam flux of ~10^{14} $cm^{-}2$ s^{-1} the average time between *successive* ion impacts would be on the order of a millisecond. Thus, in contrast to the MD simulations there is ample time between nearby ion impact events for a diffusive process such as described here to occur.

Finally, it seems likely that the resulting patterning instability would be due to preferential sputtering, leading to a "sputter shielding" effect [23] where regions where the sputtering yield is high recede around regions where the sputtering yield is low, leading to pattern formation. In order to achieve the necessary lateral compositional patterning needed to effect this behavior, two possibilities present themselves. One possibility is the lateral separation of the Ga-enriched very surface layer into two-dimensional Ga islands within a "sea" of GaSb. From TRIM simulations, the sputtering yield from 500 eV Kr^+ bombardment of pure Ga (1.1 atoms/ion) is less than that for GaSb (1.3 atoms/ion), so this is a plausible possibility. The other possibility is the exposure over time of Sb clusters due to continuous surface erosion, which have either formed in a Sb-enriched subsurface region or have been grown from Sb protoclusters as described above. The calculated sputter yield of pure Sb from 500 eV Kr^+ bombardment (1.8 atoms/ion) is higher than that of pure Ga or GaSb, so this is also a plausible possibility.

In either case, while the proposed patterning mechanisms remain hypothetical at this stage, they do provide excellent motivation for efforts, both to characterize irradiated III-V materials and to develop models for the evolution of nanopatterns on those surfaces.

3.4.2 Implications for multiscale modeling approaches

The results presented here from MD simulations clearly show that the compositional evolution of the surface must be accounted for by models of ion beam nanopatterning. More than this, it is clear that the surface composition must be treated as a significant quantity which evolves in three spatial dimensions as well as with respect to time (or fluence), and not only as a scalar variable representing a locally or globally-homogeneous surface.

Previously, computational modeling has relied primarily on considering the surface to be homogeneous, even if the composition has been altered from the usual stoichiometry [29,54]. However, the results presented above clearly show that in order for such modeling efforts to correctly describe the surface evolution, the subsurface compositional distribution must also be treated as a simulation parameter, and whether MD or BCA methods are used a suitable domain must be considered. Recently, some progress has been made towards this end, in the form of BCA simulations considering ion impacts onto a Ga_xSb_{1-x} surface, with and without an altered 1-nm layer of composition Ga_ySb_{1-y} [101]. While this provides an interesting first step towards complete consideration of surface composition, the use of BCA in these simulations may be insufficient to capture the compositional complexity implied by these compositions, since even at small scales there may be phase separation effects that can only be accurately described by MD simulations. Additionally, significant compositional variations may occur on length scales smaller than 1 nm, as illustrated by the experimental results of **Figure 3.1**.

Turning attention to theoretical modeling efforts, two significant omissions in the present body of work must be addressed based on the simulation results presented in this chapter. The first of these, which has already been alluded to, is that the existing models do not consider any form of surface compositional depth profile in their mathematical formulations. Because of this, even if a model includes the "correct" set of physical mechanisms in its formulation, the model predictions are almost certainly likely to be incorrect since the model is limited to only a two-dimensional view of the compositional evolution. The possibility might be considered that these two-dimensional models could be coupled to an ad-hoc conceptual description, such as given in **Section 3.4.1** above, to motivate the surface composition used throughout the rest of the model, e.g. using the model and experiment results to assume a surface composition of 60% Ga and 40% Sb. However, such a model would not have any predictive ability of its own, and would lack the necessary connection between the very surface and subsurface layers to describe the compositional and morphological changes as bombardment continued past the patterning threshold fluence.

A second key limitation of all existing continuum models for compound material ion beam nanopatterning is the reliance on linear differential equations with fixed coefficients for every term. For example, the phase-separation model of Norris [7] describes the evolution of the surface height (u) and composition (ϕ) fields by two coupled partial differential equations:

$$\frac{\partial u}{\partial t} = -A\phi + C\nabla^2 u - D\nabla^4 u \tag{3.10a}$$

$$\frac{\partial \phi}{\partial t} = -A'\phi + B'\nabla^2\phi + C'\nabla^2 u - E'\nabla^4\phi \tag{3.10b}$$

However, to properly include the compositional dependence, these equations must be rewritten as

$$\frac{\partial u}{\partial t} = -A(\phi)\phi + C(\phi)\nabla^2 u - D(\phi)\nabla^4 u \tag{3.11a}$$

$$\frac{\partial \phi}{\partial t} = -A'(\phi)\phi + B'(\phi)\nabla^2\phi + C'(\phi)\nabla^2 u - E'(\phi)\nabla^4\phi \tag{3.11b}$$

The compositional dependence of the lettered coefficients renders the system of equations entirely nonlinear, even without including any of the traditional nonlinear mechanisms such as tilt-dependent sputtering or Hauffe reflection [124]. The argument for neglecting these nonlinearities is that the variation in surface composition is small, at least in the very early stages of pattern formation when a linear model is applicable. However, the experimental [30] and simulation results do not support that assertion, instead clearly showing that the surface composition varies significantly well before even the earliest stages of pattern formation. In short: ***linearized models are insufficient to predict nanopattern formation by ion beam irradiation on compound material surfaces***.

To further justify this last statement, **Figure 3.20** shows GISAXS scans of etched GaSb irradiated with 500 eV Ar^+ [30]. From the scan data, the surface morphological evolution is divided across several different regimes, including early-stage smoothening, mid-stage roughening, and eventually pattern formation and growth. The existence of not one but three distinct regimes of morphology is a stark contrast to the prediction of the linear continuum theories, which by definition are only able to anticipate the evolution of only one type of morphology over time. Linear models can predict smooth surfaces with no features, rough surfaces, or periodic nanopatterns, but cannot predict the emergence and transition between all three for a single set of experimental parameters. Thus, nonlinearities such as contained by Equation (3.11) are in fact necessary to predict the correct morphological evolution of GaSb and other complex material surfaces under ion beam irradiation.

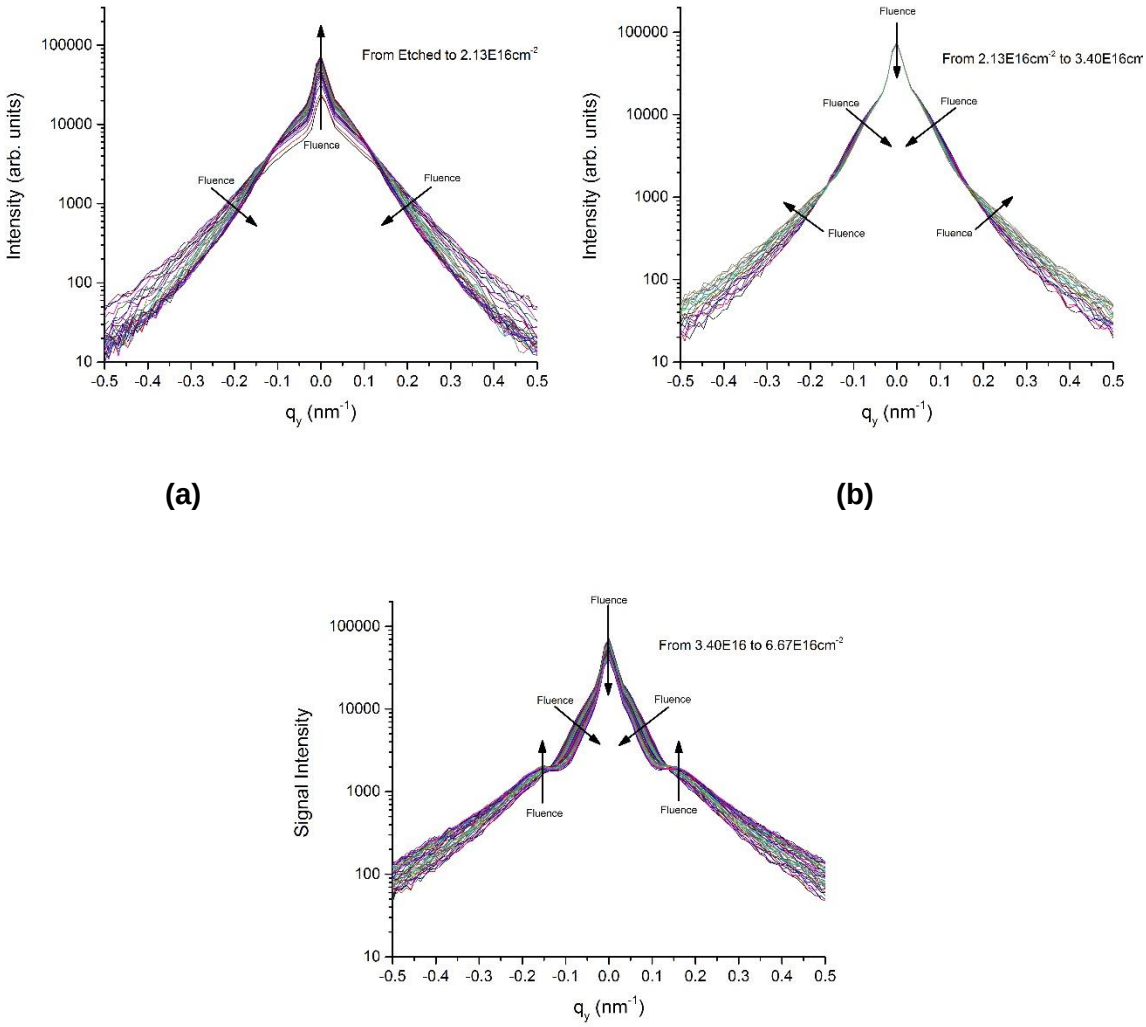

Figure 3.20: GISAXS data across numerous fluence steps from the initial surface to 6.67×10^{16} cm^{-2} fluence for 500 eV Ar^+ irradiation of etched GaSb [30], split into several steps corresponding to difference morphological evolution regimes: **(a)** initial surface smoothening; **(b)** pre-pattern coarsening, and **(c)** the onset and aftermath of pattern formation.

3.4.3 Limitations of the molecular dynamics simulations

While the MD simulations presented above are, within the constraints of the simulation design, physically accurate to a high degree, there still exist several intrinsic limitations which must be taken into account when considering the results of those simulations.

As has already been mentioned, the timescale of the MD simulations is not sufficient to study mechanisms such as ion-enhanced diffusion which occur over longer timescales. This means that while formation of Sb protoclusters, for example, can be readily observed from the prompt ion effects, within the confines of the MD methodology there is no real approach to study e.g. the growth of these clusters to determine if they may in fact become large enough to affect the compositional depth profile. To address this limitation, kinetic Monte Carlo methods are one possible approach which has already become widely used to study surface diffusion processes. From a mathematical perspective, phase-field modeling may present a useful alternative and should also be considered as an avenue for future efforts.

On the other hand, the MD simulations are inherently limited by the classical nature of the technique, and cannot directly consider quantum-mechanical effects which may be of importance. Two particular cases readily come to mind where this may be a significant limitation. First, since potentials for different materials are usually developed for the special case of homogeneous bulk crystals of exclusively a single material (whether single or multiple-component), the nature of the bonding at the interfaces between the different phases may not be well-considered by the potential used here. In this case, some form of quantum mechanical modeling such as tight-binding/DFT methods is needed here to consider the rather anomalous electronic behavior at such complex interfaces. A second case arises when considering the supposed enhanced diffusivity of Ga in GaSb [110], as this diffusivity has been found through DFT studies to be mediated by the formation of particular point defects [121–123] which admit fast Ga motion. In order to show the potential for similar fast Ga diffusion in the ion-damaged GaSb surface region, it would be necessary to similarly characterize the kinds of point defects, if any, which might be present in the amorphized region that could permit similarly-rapid Ga motion. Since point defects have a significant effect on the nearby electronic environment, quantum mechanical approach is again needed to characterize

the amorphous point defect environment and accurately determine the diffusion energy barriers for both Ga and Sb in that environment. This would likely prove to be another highly fruitful direction for future research efforts.

Chapter 4: High fluence molecular dynamics studies of noble gas ion implantation into Si

On first glance, the elemental silicon surface seems almost trivial compared to the complex multicomponent III-V semiconductor surface of the previous chapter. However, the continued lack of a consensus explanation for the patterning behavior of that Si surface implies a situation which is rather the opposite of "trivial". Among the numerous candidate mechanisms considered in models thus far – including erosion [8], mass redistribution [12], and ion-induced stress [31,33] – very little consideration has been given to the potential influence of the implanted ions themselves, with only very recent efforts beginning to investigate the possibility [125,126]. Here, the hypothesis is put to the test that implantation of ions into Si plays a critical role in determining the structure and properties of the irradiated layer which lead to pattern formation or a lack thereof. The key to this surface response lies in the formation of implanted ion clusters and their interaction with the surface as irradiation continues.

4.1 Motivation and key knowledge gaps

The structure of ion-bombarded Si can potentially play a significant role in the dynamics of the surface morphology. This has been considered explicitly in recent years by the "hydrodynamic" models which consider the stress-driven viscous flow of the ion-damaged region near the surface [31–33,36,92]. In fact, in the near-surface region it has been shown by both simulations [44] and experiments [33] that Si becomes amorphous very quickly under ion bombardment. However, additional simulations have shown that the ion-damaged Si surface reaches the same state regardless of its initial condition, including surfaces which are initially amorphous or ion-damaged [48]. Thus, how the ion-damaged layer is structurally different from amorphous Si obtained by conventional means remains unclear. Furthermore, the influence of the ion-modified

surface structure on the properties of the surface and its response to further ion bombardment is not well-understood.

Consideration of the implanted ions themselves is critical to provide the answers to these questions. While it has been known for some time that implanted ions can aggregate into clusters or bubbles at sufficiently high fluences [100,127,128], very little attention has been given to this phenomenon. Besides occasional simulations addressing e.g. the effect of clusters on sputtering yields [43], no theoretical model of nanopatterning has considered the effects of the implanted species until very recently [125,126]. Even these recent models are limited to the consideration of single-ion effects on the local surface height, and provide no insight into structural modifications or collective effects due to the implantation. These are quite glaring omissions from the present body of work on ion beam nanopatterning, which is contrary to the acknowledged importance of these effects from studies in other fields. For example, in the literature on nuclear fusion plasma-material interactions it is widely accepted that He bubble formation is instrumental in the creation of tungsten "fuzz" under divertor plasma conditions [129].

In the work presented here, the implanted species are explicitly included in the data analysis, and they are therefore considered as a compositional impurity within the Si matrix. This means that, among other considerations, the formation and behavior of distinct phases (i.e. clusters) composed of the implanted species are studied. This breaks from the traditional view of ion-bombarded Si as a single-component system, bringing this work into line with the multicomponent phenomena considered in the previous studies of III-V nanopatterning (**Chapter 3**). This expansion of scope to include compositional mechanisms also serves to lay groundwork for the study of metal/silicon systems which are known to form quantum dots under ion beam irradiation [130–132].

4.2 Design of simulations

4.2.1 MD simulations of ion implantation

MD simulations have been carried out using LAMMPS [84] to study cumulative bombardment and implantation of noble gas ions (Ne^+, Ar^+, Kr^+, Xe^+) on Si surfaces. The simulation setup is shown in **Figure 4.1** schematically. The simulation box has dimensions of 13 × 13 × 21 lattice cells (lattice constant a = 5.431 Å). An initially-crystalline layer of Si(001) is created in the lower 13 × 13 × 17 lattice cells (~23,000 atoms) of the simulation box, with a per-atom velocity distribution corresponding to an initial temperature of 300 K. The remaining space at the top of the simulation box is left as empty vacuum. The bottom layer (13 × 13 × 1 lattice cells) of the simulation box is held as a fixed boundary representing the interface between the near-surface region and the bulk crystalline Si below in a real system. The two next-lowest layers are treated as a heat sink, and are controlled by a Berendsen thermostat [112] with an equilibrium temperature of 300 K. The remaining layers of Si atoms are able to move freely and interact with each other as well as the incident and implanted ions over the course of the simulation.

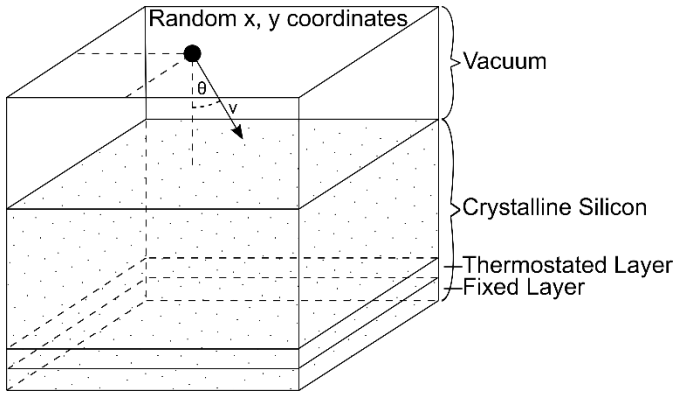

Figure 4.1: Design of simulation schematic showing the vertical divisions of the MD simulation cell. Sputtered and reflected particles are removed from the top of the simulation cell.

Ions are generated successively in the vacuum region near the top of the simulation cell at random lateral coordinates, with a velocity directed toward the surface based on the specified incidence

angle and energy. For each time integration step in LAMMPS, a timestep is chosen dynamically based on the calculated particle velocities so that no particle is displaced by more than 1 pm in a single timestep. A single-ion impact takes place over a total of 20,000 timesteps, which is sufficient to allow the energy from the ion impact to be dispersed and the surface to reach a local equilibrium state. After these 20,000 timesteps, the position data of all particles is written to an output file and a new ion is generated. For these simulations, anywhere from 1,500 to 5,000 consecutive impacts were simulated.

The accuracy of the results from MD simulations hinges on the choice of interatomic potentials used. Thus, MD simulations of normal-incidence Ar^+ bombardment of Si(001) at various ion energies were carried out using several combinations of interatomic potentials, and the sputtering yields were calculated for comparison to experimental results [133–137]. The potential combinations consisted of using either a Stillinger-Weber (S-W) [138] or Tersoff [115] potential to represent Si-Si interactions, along with using either a Molière [139] or ZBL [58] potential to represent the repulsive ion-Si and ion-ion interactions. The results are shown in **Figure 4.2** and indicate that the combination of the S-W and ZBL potentials gives the best overall agreement with experimental data, while the Tersoff potential gives particularly poor results at lower ion energies. Thus, the S-W/ZBL combination of potentials was chosen for all simulations presented in the remainder of this chapter.

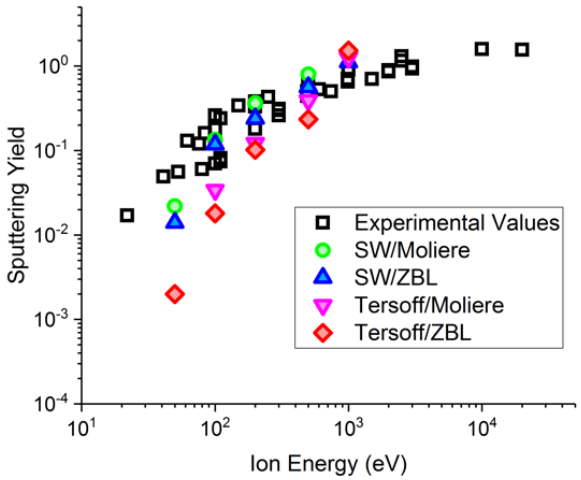

Figure 4.2: Comparison of sputtering yields from experiments [133–137] to those calculated for Ar^+ bombardment of Si(001) using various combinations of MD potentials to represent the Si-Si and Si-Ar/Ar-Ar interactions.

The "base case" simulation, from which individual parameters were usually varied in other simulations, was 500 eV normal incidence Ar^+ bombardment of Si(001). To study the effects of the ion species (i.e. mass), 500 eV normal incidence bombardment was simulated with Ne^+, Kr^+, and Xe^+ ions. To study the effects of the ion energy, normal incidence Ar^+ bombardment was simulated at 20, 50, 100, 200, and 1000 eV. To study the effects of the ion incidence angle, 500 eV Ar^+ bombardment was simulated at 20°, 40°, 45°, 50°, 60°, and 85°, and 500 eV Ne^+ bombardment was additionally simulated at 45° and 60°. All simulations were run to a cumulative ion fluence of at least 3×10^{15} cm^{-2}.

4.2.2. Analysis of simulation data

Several complementary methods were used to analyze the resulting data. The starting point for most analysis was OVITO [119], which was used to render two-dimensional projections and full three-dimensional snapshots of the atomic positions at various timesteps. From these visualization, a key finding was the presence of clusters of implanted ions formed at sufficiently high implantation fluences, which remained a focal point of the following analysis.

Clusters of implanted ions were programmatically identified by finding groups of ions with a cutoff distance *d* of each other. The process used to choose this cutoff distance is shown in **Figure 4.3**, and consisted of counting the number of ions in clusters for various values of *d*. For a range of values spanning approximately $d \in [5, 6]$ Å the number of ions in clusters was found to be insensitive to variations in *d*, leading to the final choice of 5.4 Å as the cutoff distance for the following analysis. For most purposes, a cluster was only labeled as such if it contained more than 5 ions, large enough to occupy a substantial volume free of Si atoms.

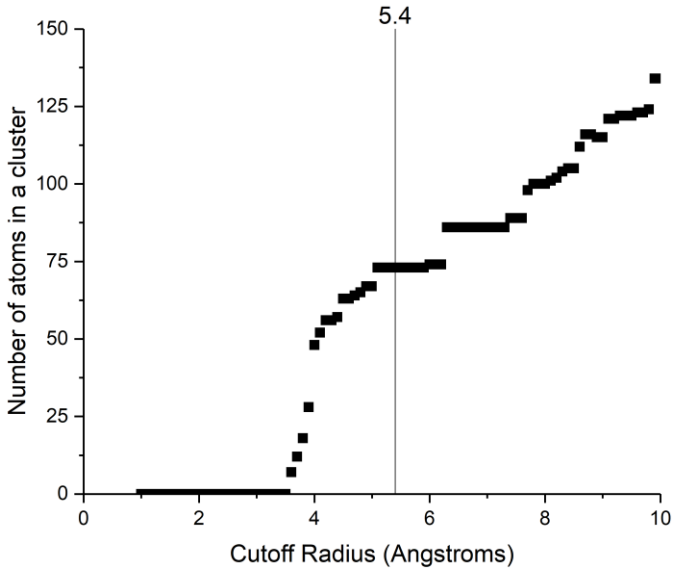

Figure 4.3: Selection of the cutoff distance between implanted atoms used to determine the existence of a cluster. The cutoff is chosen to be a value near which the number of atoms in clusters is insensitive to small changes in the cutoff value.

Once the existence of clusters and the set of implanted ions in clusters could be found programmatically, several key quantities were obtained, including the number of implanted species, the fraction of implanted ions which were members of clusters, and the size distribution of the clusters. In addition, depth profiles of the implanted ions were constructed by dividing the surface into horizontal layers 5 Å in thickness, and counting the number of implanted ions in each layer.

To determine the estimated steady-state values for these quantities, the calculation results were averaged over all data snapshots for fluences greater than 10^{15} cm^{-2}, by which fluence a "quasi-steady state" had been reached for all parameter sets.

For computation of mechanical properties, the LAMMPS stress tensor computation was used [140]. This computation yields the 3 × 3 per-atom stress tensor, which was then averaged over over thin horizontal layers (to obtain shear stress depth profiles). As with the implantation and clustering measurements, these calculations were carried out as an average over all fluence steps beyond 10^{15} cm^{-2} to provide time-averaged quasi-steady state values for the various measurements of interest. Additionally, tensile strain tests were carried out using LAMMPS to calculate the elastic modulus of the ion-implanted surface under various conditions.

4.3 Influence of cluster formation on surface morphology

Ion bombardment of initially-crystalline Si(001) was carried out to cumulative fluences of at least 3×10^{15} cm^{-2} for a variety of simulation parameters, focusing on the effects of: incident ion species (mass), incident ion energy, and incidence angle. Additionally, considerable effort was devoted towards understanding the fluence dependence of the implanted ion concentration, clustering, and related phenomena. In most cases, implanted ions tended to form clusters even in the early stages of the simulations, with the size and distribution of the clusters strongly-dependent on the simulation parameters and closely correlated to the implanted ion concentration in general. It should be noted, and is shown in several figures below, that the implanted ion concentration does not reach a true "steady state", but rather achieves a "quasi-steady state" at which the instantaneous implanted ion concentration wavers about some mean value due to fluctuations from implantation, ion reflection, sputtering, degassing, etc. This is observed due to the limited size of the MD simulation cell; for an "infinite" simulation domain (i.e. wafer scale, ~cm length), these local

fluctuations would average out over space and the implanted ion concentration would in fact approach a constant steady-state value.

The results for ion implantation of 500 eV Ne^+ into Si are shown in **Figure 4.4** for normal incidence. Under these conditions, 67% (±11%) of implanted ions were members of a cluster once a quasi-steady state concentration profile was achieved. The average cluster size was 14 (±3.6) ions per cluster. Both of these values represent the largest measurements obtained for any set of simulation parameters. The average quasi-steady state concentration of the implanted ions was 7.0×10^{14} ($\pm0.8\times10^{14}$) cm^{-2}, which was higher than the implanted concentration of any other ion species studied at normal incidence. Overall, the increased degree of implantation and clustering of Ne in Si suggests that any effects due to the implanted ions or clusters will be correspondingly greater than for other (heavier) ion species.

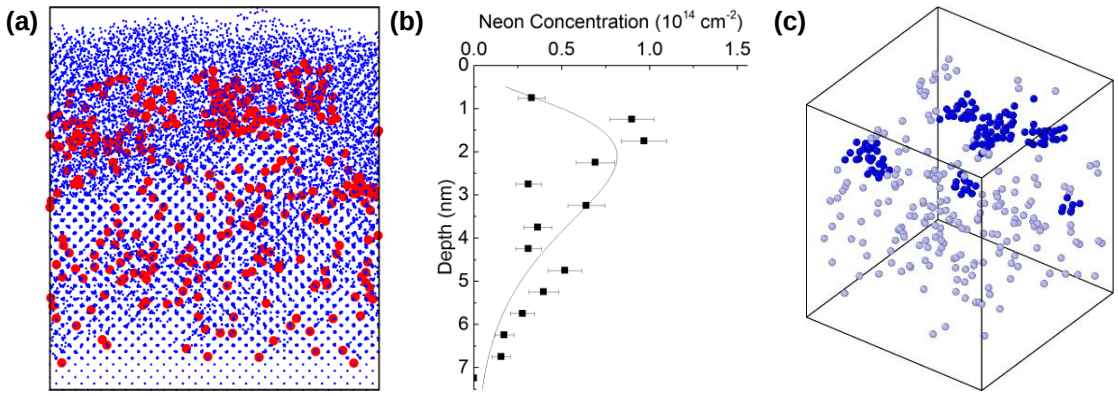

Figure 4.4: Summary of results for ion implantation of 500 eV Ne^+ up to a fluence of 3×10^{15} cm^{-2}. (a) Side view of Ne ions (red) in the Si (blue) matrix. (b) Depth profile of implanted Ne. (c) 3D view of implanted ions, with faded ions being isolated from each other and darkened ions being members of a cluster. Only clusters of six or more ions are darkened.

The results for implantation of 500 eV Ar^+ into Si are shown in **Figure 4.5** for normal incidence. For these conditions, the quasi-steady state concentration of implanted Ar was 3.7×10^{14} ($\pm0.5\times10^{14}$) cm^{-2}. Of the implanted ions, 56% (±13%) were members of a cluster. The average size of an Ar cluster was 10 (±3.3) ions per cluster. All of these values are median among those for the different ion species studied.

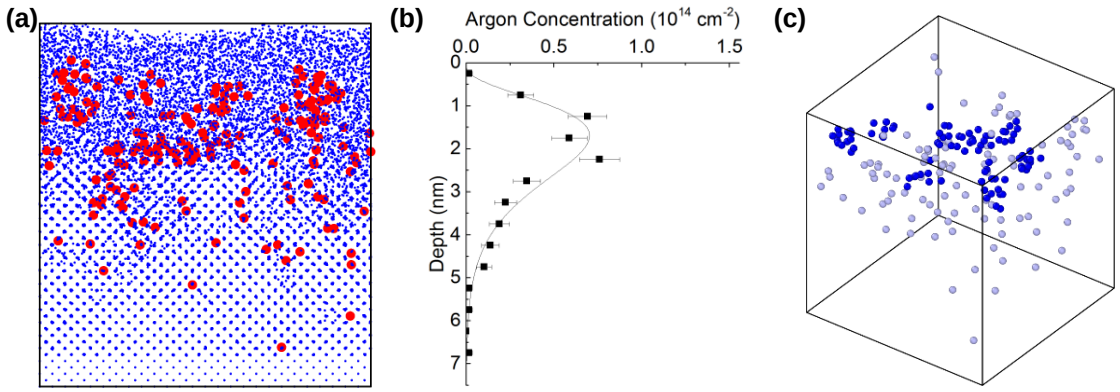

Figure 4.5: Summary of results for ion implantation of 500 eV Ar^+ up to a fluence of 3×10^{15} cm^{-2}. (a) Side view of Ar ions (red) in the Si (blue) matrix. (b) Depth profile of implanted Ar. (c) 3D view of implanted ions, with faded ions being isolated from each other and darkened ions being members of a cluster. Only clusters of six or more ions are darkened.

The results for 500 eV Kr^+ irradiation of Si are given in **Figure 4.6** for the normal-incidence case. Under these conditions, the quasi-steady state concentration was found to be 3.0×10^{14} ($\pm0.5\times10^{14}$) cm^{-2}. Of the implanted ions, 47% (±15%) were found to be part of a cluster. The average size of these clusters was measured as 7.6 (±2.6) atoms per cluster. Along with the very similar values for Xe^+ irradiation at the same conditions, these values represent the lower end of the range for the various ion species studied, suggesting that the effects of implantation or clustering in Si are minimized for these heavier ion species.

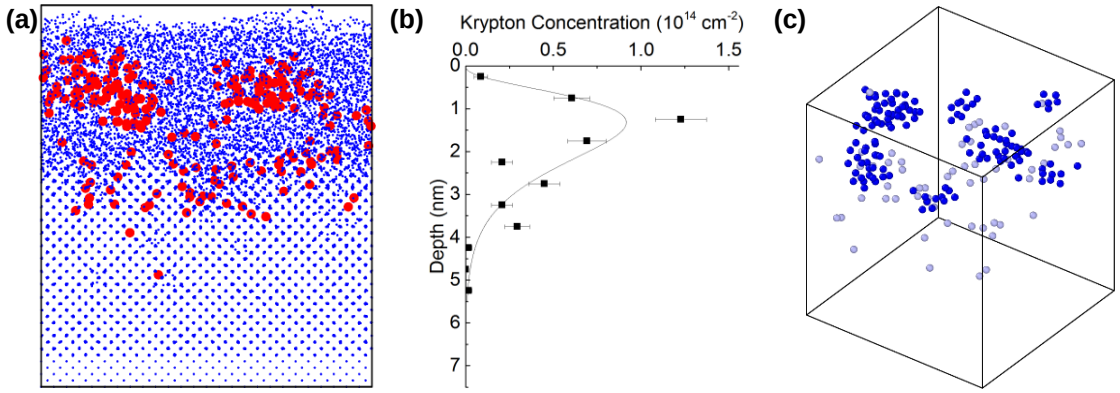

Figure 4.6: Summary of results for ion implantation of 500 eV Kr^+ up to a fluence of 3×10^{15} cm^{-2}. (a) Side view of Kr ions (red) in the Si (blue) matrix. (b) Depth profile of implanted Kr. (c) 3D view of implanted ions, with faded ions being isolated from each other and darkened ions being members of a cluster. Only clusters of six or more ions are darkened.

Finally, the results for 500 eV Xe^+ implantation into Si at normal incidence are shown in **Figure 4.7**. In short, the results are very similar to those for Kr^+ implantation under the same conditions, and in fact are identical when accounting for the uncertainty of the measured values. The quasi-steady state concentration was measured as 3.5×10^{14} ($\pm0.5\times10^{14}$) cm^{-2}. Of the implanted ions, 51% (±10%) were members of a cluster on average. The mean cluster size was found to be 7.9 (±1.8) ions per cluster. As for Kr^+ implantation, these values make up the lower end of the range for the ion species studied, and effects of the implanted atoms would be relatively minimal for Xe^+ implantation as a result. The quantitative data for implantation of all ion species is summarized in **Figure 4.8**. The relatively-greater implantation and clustering of Ne^+ in Si, discussed previously, is easily seen from these graphs.

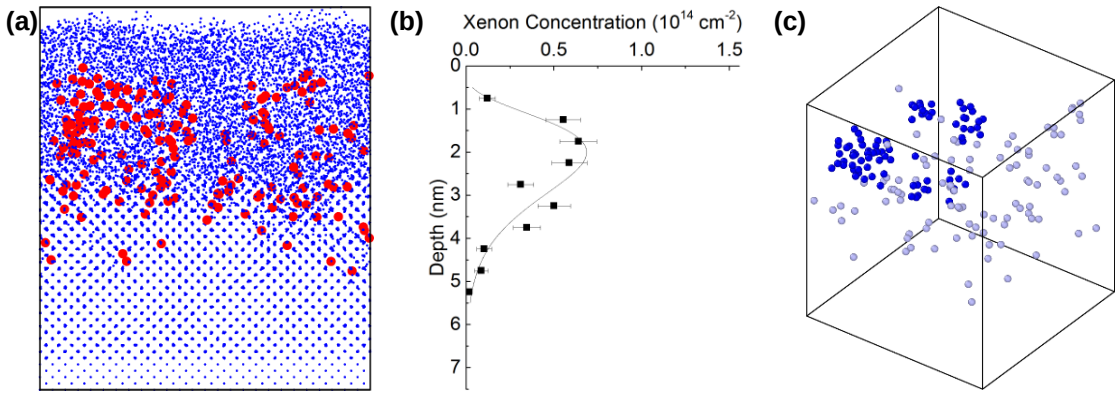

Figure 4.7: Summary of results for ion implantation of 500 eV Xe^+ up to a fluence of 3×10^{15} cm^{-2}. (a) Side view of Xe ions (red) in the Si (blue) matrix. (b) Depth profile of implanted Xe. (c) 3D view of implanted ions, with faded ions being isolated from each other and darkened ions being members of a cluster. Only clusters of six or more ions are darkened.

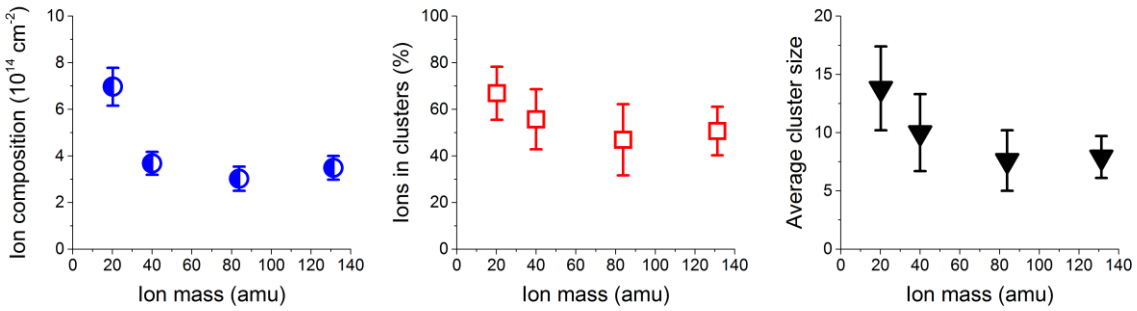

Figure 4.8: Variation of the implanted ion concentration (left), fraction of ions in clusters (middle), and average cluster size (right) with the incident ion mass (i.e. species) at 500 eV and normal incidence.

In addition to the ion mass, the incidence energy and angle were also used to characterize the ion implantation and cluster formation. **Figure 4.9** shows the dependence of the implanted ion concentration, ion clustering percentage, and average cluster size with respect to the incident ion energy for normal incidence Ar^+ irradiation. In general, all of these quantities increase as the ion energy increases. This is expected intuitively, since the low-energy ions will not penetrate as deeply and will remain close to the surface to be sputtered away or desorbed relatively quickly, in addition to being more easily reflected from the surface. However, at the highest simulated energy (1 keV), these quantities all decrease. With regards to toe clustering percentage and average cluster size, this may be attributable to the greater penetration of the high-energy ions leading to a wider distribution of implanted species along the depth axis, leaving fewer ions in proximity to form clusters. Alternatively, the increased sputtering yield at 1 keV (see **Figure 4.2**) may lead to a more rapid removal of implanted ions before the concentration and clustering parameters can reach higher values. Regardless, because of this higher-energy decrease in the relevant values, it appears that 500 eV is the optimal choice of energy to observe clustering phenomena, and therefore this energy was used for the remaining studies.

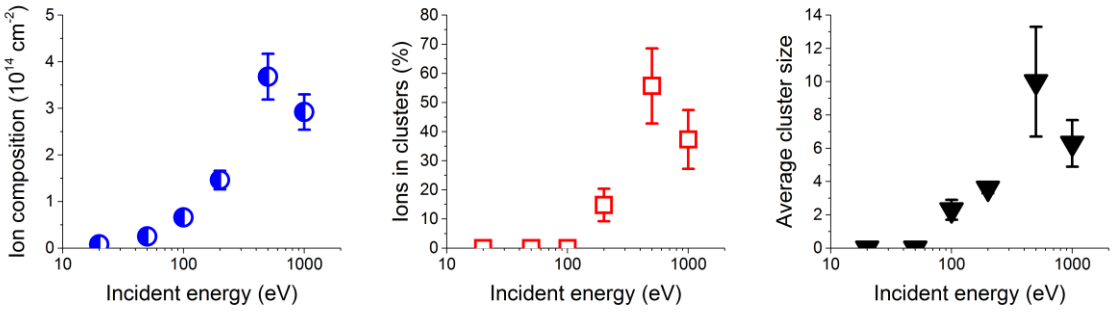

Figure 4.9: Variation of the implanted ion concentration (left), fraction of ions in clusters (middle), and average cluster size (right) with the incident ion energy for normal incidence Ar^+ implantation.

Figure 4.10 shows the dependence of the implanted ion concentration, ion clustering percentage, and average cluster size with respect to the ion incidence energy for 500 eV Ar^+ irradiation. Both

the percentage of ions in a cluster and the average cluster size decrease in a more or less linear fashion as the incidence angle increases. However, the implanted concentration remains fairly steady up to an incidence angle of 40° before dropping off sharply at 45° and higher incidence angles. This latter behavior is intriguing, as the apparent transition angle is close to the experimentally-observed transition angle between 45-50° for which a Si surface under Ar^+ irradiation exhibits the formation of self-organized ripple nanopatterns [90,91]. This in turn suggests that the implanted ions and/or clusters play a key role in the flat-to-rippled transition. Specifically, a greater concentration of implanted species at lower incidence angles would be expected to contribute a stabilizing or pattern-suppressing influence to the ion-surface dynamics.

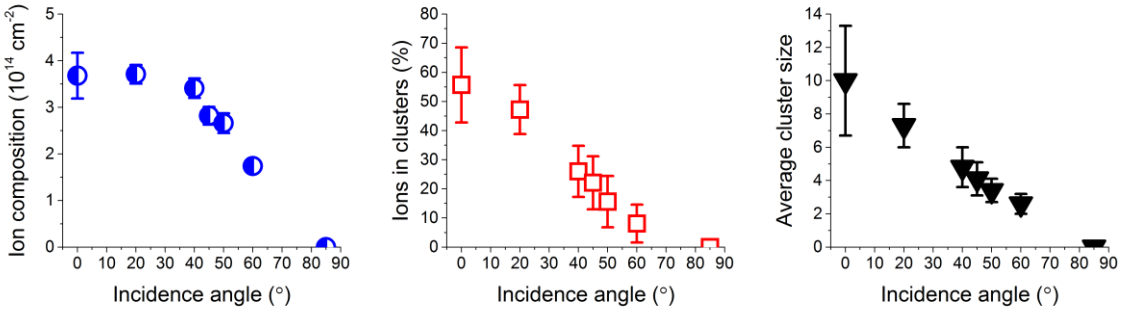

Figure 4.10: Variation of the implanted ion concentration (left), fraction of ions in clusters (middle), and average cluster size (right) with the ion incidence angle for 500 eV Ar^+ irradiation.

Detailed visualization of the surface evolution with fluence shows that the cluster degassing is the mechanism contributing to surface evolution. **Figure 4.11** illustrates how the cluster degassing mechanism interacts with the surface morphology. Once a cluster has formed beneath the surface, the continued ion sputtering of Si causes the surface to recede and eventually exposes the cluster to vacuum. On exposure, the cluster rapidly degasses from the surface, leaving behind a void which is quickly filled by a mass inflow of Si from the surrounding amorphous layer. This results in a topological disruption several nm in diameter spanning the region formerly housing a cluster, which could have the additional effect of eliminating any nascent nanostructures at the surface which might otherwise serve as "seeds" for long-scale nanopattern formation. Thus, this degassing

mechanism provides a likely vehicle for the proposed pattern-suppressing influence of the implanted ions and cluster formation.

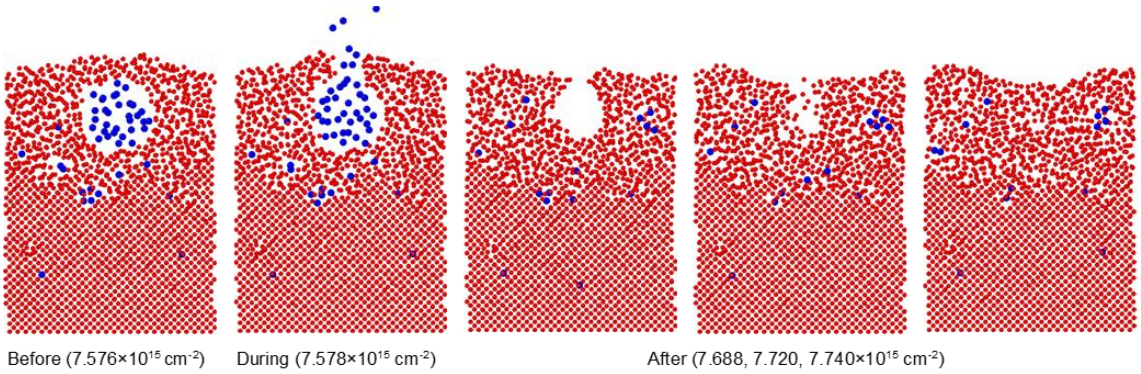

Figure 4.11: Illustration of the cluster degassing mechanism and its effect on the surface, shown by cross-sectional snapshots of the irradiated Si surface at several successive fluences. An implanted Ar cluster is exposed to the vacuum as the Si layer above it is sputtered away, leading to rapid degassing and leaving a void at the surface. Si atoms from the surrounding amorphous region flow into the void, disrupting the topography of the nearby surface.

To develop a complete mathematical or computational model of ion-induced nanopatterning which incorporates the proposed cluster degassing mechanism is beyond the scope of the present work. However, since the prevalence of cluster degassing is directly proportional to the degree of ion implantation and cluster formation, these latter quantities can be related to experimental conditions for which patterns are known to form or not to form. If the highest degree of ion implantation and clustering correlates to experimental parameters for which patterning is not observed, and the lowest degree of ion implantation and clustering correlates to parameters for which patterning is observed, then the proposed degassing mechanism is supported by the correlation.

To this end, **Figure 4.12** shows the evolution of the implanted ion concentration for 500 eV Ar^+ bombardment with respect to fluence, and compares this evolution for various ion incidence angles. It is readily seen that the implanted ion concentration oscillates significantly and rapidly, with sharp drops corresponding to cluster degassing events which occur quite frequently. To highlight the underlying trend in the ion concentration, fitted average curves are plotted in **Figure 4.12** on top

of the simulation data. To interpret these curves, it should be noted that the oscillations in concentration are apparent due to the small size of the MD simulation cell, and that over an entire experiment-scale (~cm^2) surface the spatially-averaged concentration will vary smoothly as indicated by the fitted curves. Thus, these curves indicate that the concentration of implanted ions in the surface will increase linearly at first before reaching an asymptotic value which varies with the experimental parameters such as the ion incidence angle.

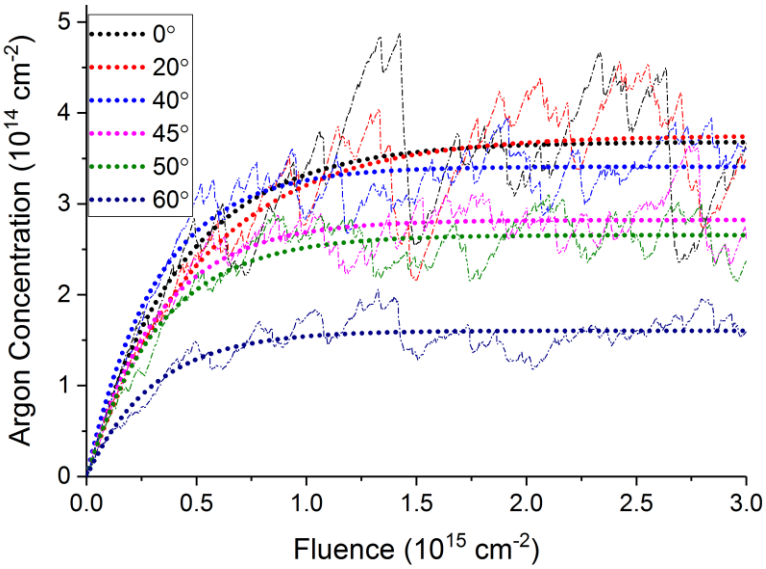

Figure 4.12: Fluence dependence of the implanted ion concentration for 500 eV Ar^+ irradiation of Si at various ion incidence angles. The dotted lines indicate fitted curves showing the estimated average concentration for an arbitrarily-large surface.

Taking this into consideration, **Figure 4.12** provides two notable points of support for the cluster degassing mechanism. First, as discussed previously the concentration of implanted ions is greater for lower incidence angles, remaining fairly high even up to 40° before decreasing significantly at higher incidence angles. Secondly, the magnitude of the sharp drops in the concentration levels is greatest at lower incidence angles and particularly for normal incidence, indicating that the relative effect of cluster degassing on the surface morphology is stronger at lower angles of incidence. The fact that both of these indicators are most prominent at lower angles of incidence, and the correlation with experimental observations that nanopatterns do not form at lower incidence angles,

supports the conjecture that cluster degassing provides a mechanism to stabilize ion-irradiated Si against nanopattern formation by disrupting the "seeds" of those nanopatterns.

Additional support for this stabilization mechanism is found from a closer study of Ne^+ implantation into Si. Unlike the other heavier ion species considered here, Ne^+ does not induce nanopattern formation on Si during low-energy irradiation [96]. In the framework of a cluster degassing mechanism, this would be expected to correlate with an increase in the ion implantation and clustering compared to that observed from other, heavier ion species. As seen in **Figure 4.13** for 500 eV irradiation at normal incidence, this is indeed the case as Ne implants twice as strongly as any of the other ion species considered here. Furthermore, the size of the oscillations in ion concentration are similarly much greater, indicating that the cluster degassing has a substantially greater impact on the local surface morphology compared to that of the heavier species. Thus, the cluster degassing mechanism for surface stabilization offers a reasonably probable explanation for the difficulty of obtaining nanopatterns from low-energy Ne^+ irradiation.

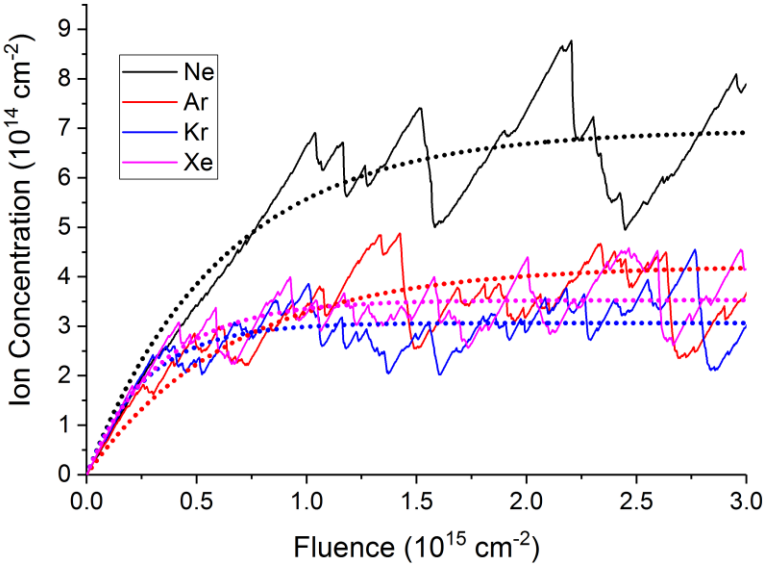

Figure 4.13: Fluence dependence of the implanted ion concentration for 500 eV normal incidence irradiation of Si with various ion species. The dotted lines indicate fitted curves showing the estimated average concentration for an arbitrarily-large surface.

A cursory investigation of the incidence angle dependence of the 500 eV Ne^+ implantation, shown in **Figure 4.14**, further supports this assessment. As seen previously for Ar^+ irradiation (**Figure 4.12**), the implanted ion concentration remains fairly similar for lower angles over a fairly wide range, in this case up to at least 45°, before dropping significantly at the higher incidence angle of 60°. However, even for 60° incidence the quasi-steady-state concentration of implanted Ne is still 4.3×10^{14} cm^{-2}, which is notably greater than the concentration measured for Ar^+ implantation at normal incidence (3.7×10^{14} cm^{-2}). Thus, even up to fairly large angles of incidence, the pattern-suppressing effects of cluster degassing from implanted Ne would still be sufficiently strong to prevent pattern formation, in excellent agreement with the experimentally-observed difficulty of obtaining nanopatterns for the Ne^+ on Si system.

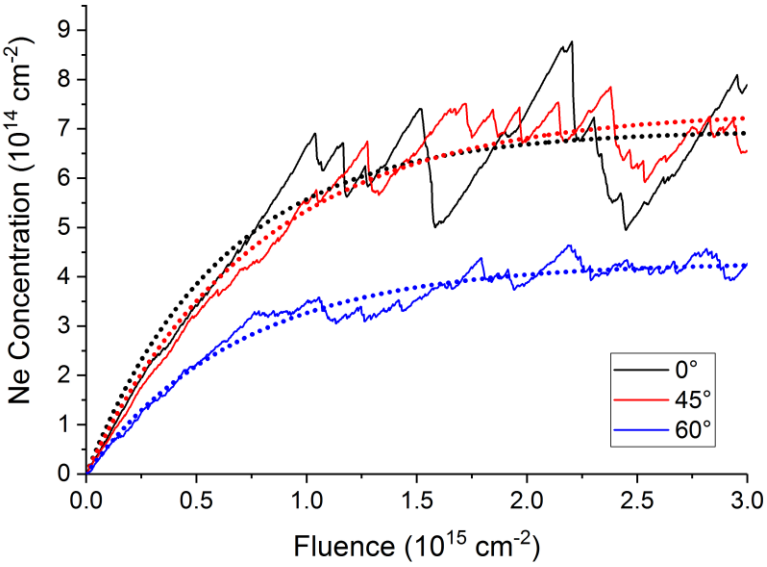

Figure 4.14: Fluence dependence of the implanted ion concentration for 500 eV Ar^+ irradiation of Si at various ion incidence angles. The dotted lines indicate fitted curves showing the estimated average concentration for an arbitrarily-large surface.

4.4 Influence of cluster formation on mechanical properties of Si

The influence of ion bombardment on the mechanical properties of Si, particularly the ion-induced stress and strain profiles, have seen recent interest in light of the development of the so-called

"hydrodynamic" models of ion beam nanopatterning [31,33]. These models rely on a functional form of the ion-induced stress depth profile to drive nanopatterning formation, and thus it is of relevance to determine the accuracy of these functional forms as well as to observe any significant influence from the implanted ion clustering detailed previously.

To this end, shear stress depth profiles were calculated for a few incidence angles of 500 eV Ar^+ bombardment of Si. **Figure 4.15** shows the stress depth profiles for normal incidence under these conditions (note that positive stress is compressive in these figures). Parts **(a)** and **(b)** show representative examples of the stress profiles at two different fluences within the quasi-steady state domain ($>10^{15}$ cm^{-2}). In both plots the stress varies wildly even between adjacent layers, and it is very difficult to see a trend in the stress profile at a given fluence. **Figure 4.15(c)**, however, shows the average stress depth profile computed at numerous individual fluences, and from this average result the trend with respect to depth is made clear. In fact, the shear stress varies in a roughly linear fashion with depth, agreeing with earlier assumptions made in the development of the hydrodynamic model for nanopattern formation [33].

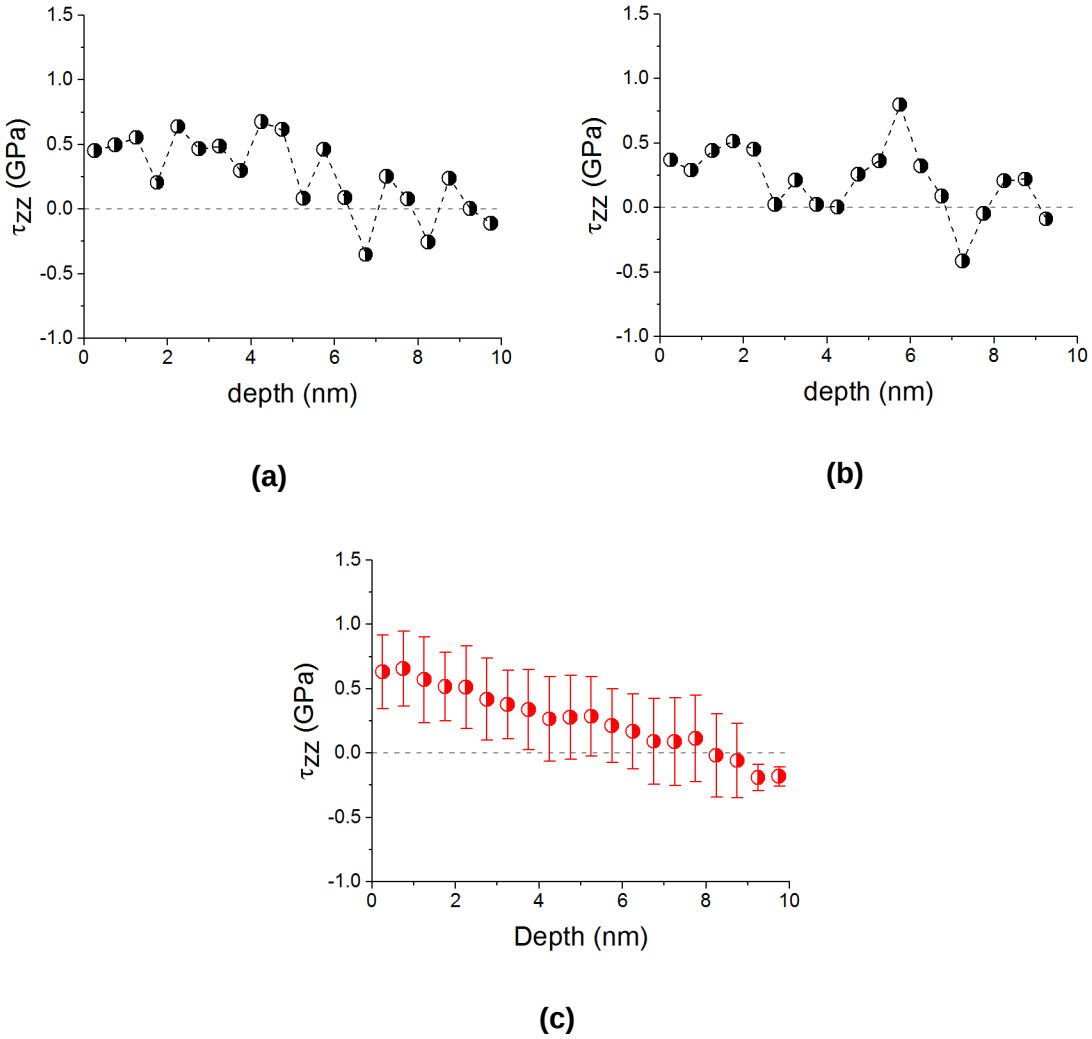

Figure 4.15: Shear stress depth profiles for 500 eV Ar^+ irradiation of Si at normal incidence: **(a)** calculated at a fluence of 1.3×10^{15} cm^{-2}; **(b)** calculated at a fluence of 2.8×10^{15} cm^{-2}; **(c)** quasi-steady state average calculated over numerous fluence steps.

Figure 4.16 shows the same shear stress depth profiles calculated for 45° incidence and otherwise the same conditions. Again, parts **(a)** and **(b)** show representative stress profiles for individual fluence steps. Here, the linear trend with depth is clearer than for normal incidence, but it is still evident that there can be significant deviations from the trend, particularly in cases such as that shown in **Figure 4.16(a)**. The fluence-averaged quasi-steady state data shown in **Figure 4.16(c)** mostly confirms this linear trend, although some small deviations persist in the averaged data.

Compared to the data at normal incidence (**Figure 4.15(c)**), it is worth noting that the stress reaches zero at a depth of only ~7 nm compared to ~9-10 nm for the normal incidence case.

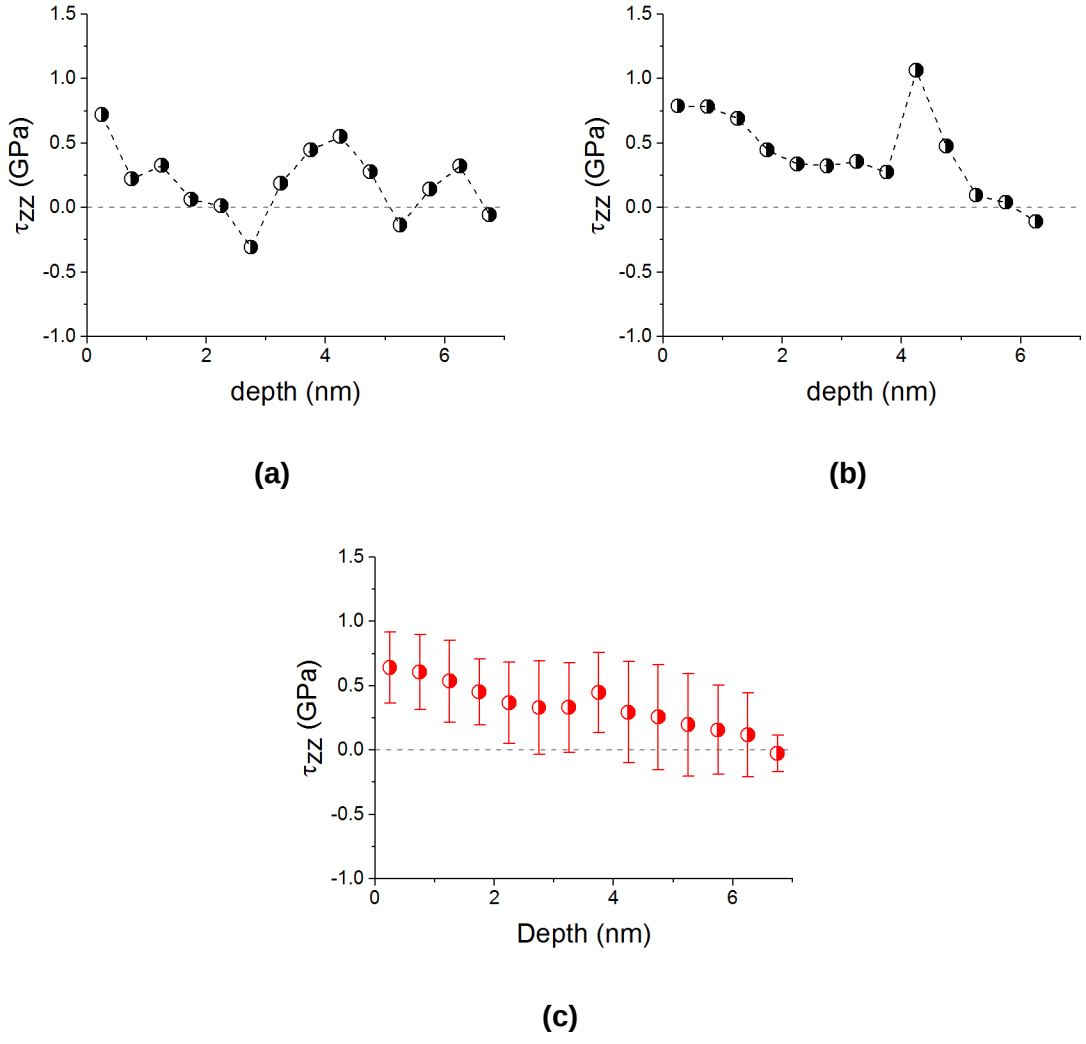

Figure 4.16: Shear stress depth profiles for 500 eV Ar^+ irradiation of Si at 45° incidence: **(a)** at a fluence of 1.3×10^{15} cm^{-2}; **(b)** at a fluence of 2.8×10^{15} cm^{-2}; **(c)** quasi-steady state average over many fluence steps.

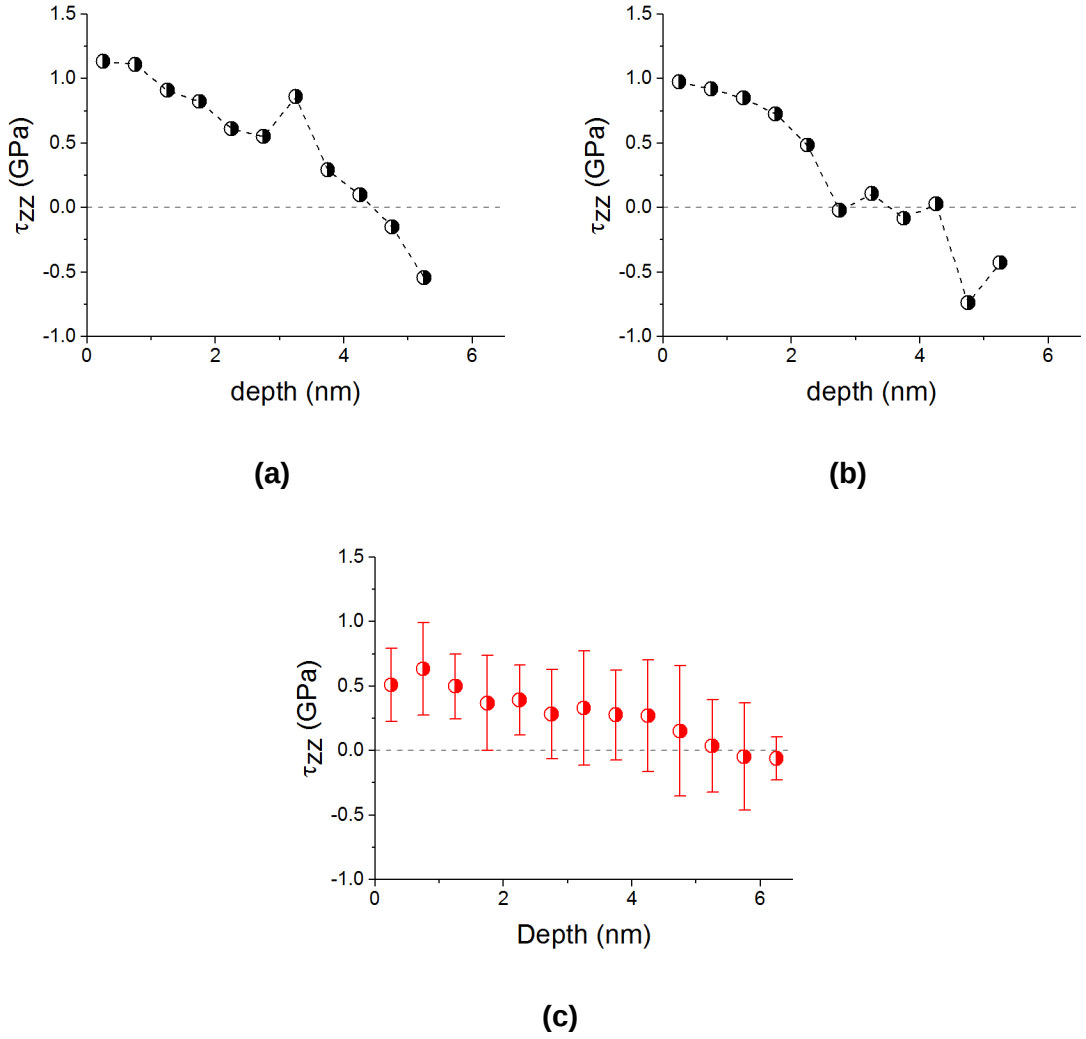

Figure 4.17: Shear stress depth profiles for 500 eV Ar^+ irradiation of Si at 60° incidence: **(a)** calculated at a fluence of 1.3×10^{15} cm^{-2}; **(b)** calculated at a fluence of 2.8×10^{15} cm^{-2}; **(c)** quasi-steady state average calculated over numerous fluence steps.

Finally, **Figure 4.17** shows shear stress depth profiles for irradiation at 60° incidence under the same conditions. The stress profiles for individual fluence steps in parts **(a)** and **(b)** show the clearest adherence to a linear trendline, with only a few significant deviations compared to the stress in samples irradiated at lower incidence angles. Interestingly, the fluence-averaged profile in **Figure 4.17(c)** is actually less linear than the corresponding average profiles at lower incidence angles, but the overall linear decrease in stress with increasing depth is still evident. From this

trend, it appears that the stress reaches zero at a depth of ~5.5 nm, which is a little more than half of the zero-stress depth found for normal incidence.

Comparing the trends across all three angles considered, the most apparent similarity is the linear decrease in (compressive) stress with increasing depth. As the incidence angle increases, two primary differences can be seen between the different conditions. First, the variation of the stress depth profile is much greater for lower incidence angles. Based on the discussion in **Section 4.3**, this may be attributable to a greater amount of clustering at those angles, leading to more frequent and more pronounced local variations in the structure and bond energy within the surface. Second, the slope of the linear trend increases in magnitude as the incidence angle increases, as seen from the decrease in zero-stress depth for successively larger angles. While the overall trend in the shear stress remains the same, the surface thickness which is under compression becomes smaller with increasing incidence angle. This is expected, since ions arriving at glancing angles to the surface will penetrate less deeply than ions incident at near-normal angles, and thus will modify a lesser thickness of the surface.

It is also of some interest to determine the effect of the ion implantation on the elastic modulus of the Si surface, and this has been measured using LAMMPS to perform simple tensile testing. The dependence of the elastic modulus on the ion fluence and implanted concentration is shown in **Figure 4.18**. The dependence on fluence is reasonably clear for the earliest stages, but quickly becomes unpredictable after a short time. On the other hand, when the elastic modulus is functionalized with respect to the implanted ion concentration in the surface, the dependence is very clear and straightforward although some variance still remains between data points.

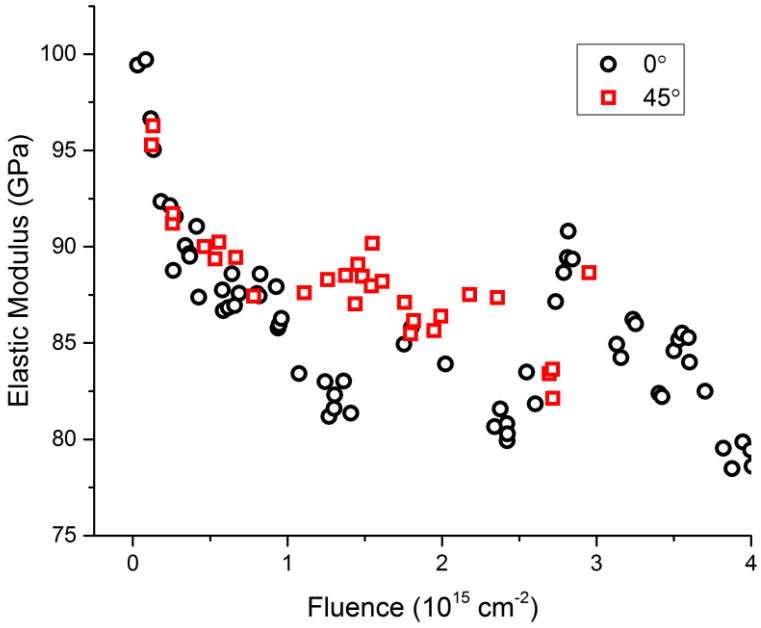

(a)

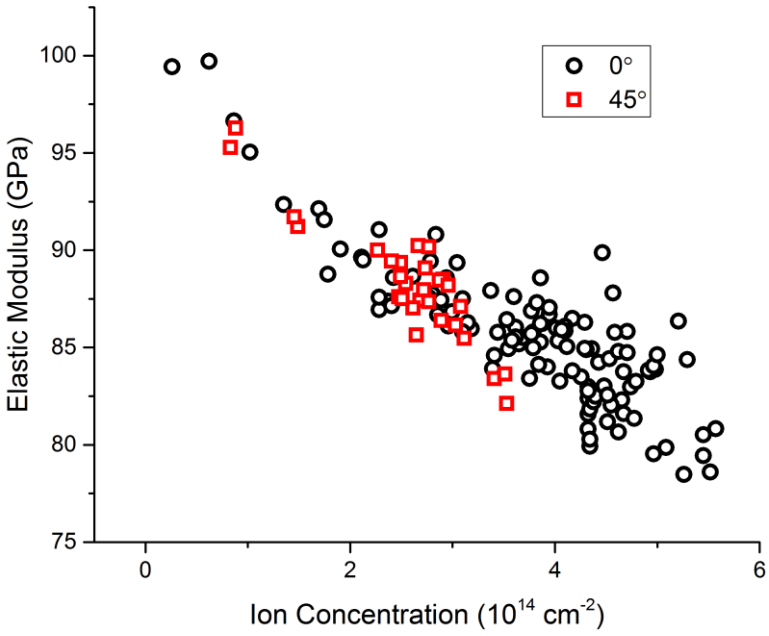

(b)

Figure 4.18: Elastic modulus of Si bombarded by Ar^+ at normal incidence and 500 eV: **(a)** as it depends on the ion fluence, and **(b)** as it depends on the implanted ion concentration.

It is reasonable to conclude that the primary determining factor in the surface elastic modulus is the concentration of implanted species rather than a measure of surface "damage" such as displacements per atom (dpa). This conclusion is further supported by the fact that normalization to implanted concentration largely eliminates the difference in the measured elastic modulus between different incidence angles (such as 0° and 45° as shown). Intuitively, this makes sense, since once the surface is (quickly) amorphized there is little real change in its structure due to additional dpa. However, the presence of implanted ions provides a repulsive force, seen as compressive stress in **Figures 4.15-4.17**, which contributes to "pushing apart" the surface. This would lead to a reduction in the elastic modulus under tensile testing, just as observed in **Figure 4.18**, as the ion concentration in the surface increases.

It was previously suggested that the formation of clusters could be responsible for the significant localized variance in the shear stress profiles of ion-implanted Si. Continuing along this line of thought, it is reasonable to inquire what the effect of clustering might be on measurable properties such as the elastic modulus. **Figure 4.19** presents some calculations to this end, comparing the elastic modulus for as-implanted Si at various ion concentrations to the elastic modulus calculated for a Si surface with some Si atoms replaced at random by Ar atoms. Compared to the as-implanted trend, the elastic modulus is nearly constant for the randomly-inserted Ar surfaces, decreasing only slightly as the Ar concentration increases. This strongly suggests that the presence of implanted ion clusters within the surface is critical for determining the mechanical properties and response of the modified surface, allowing the total effect of the implanted ions to be greater than the sum of their individual effects on the surface properties.

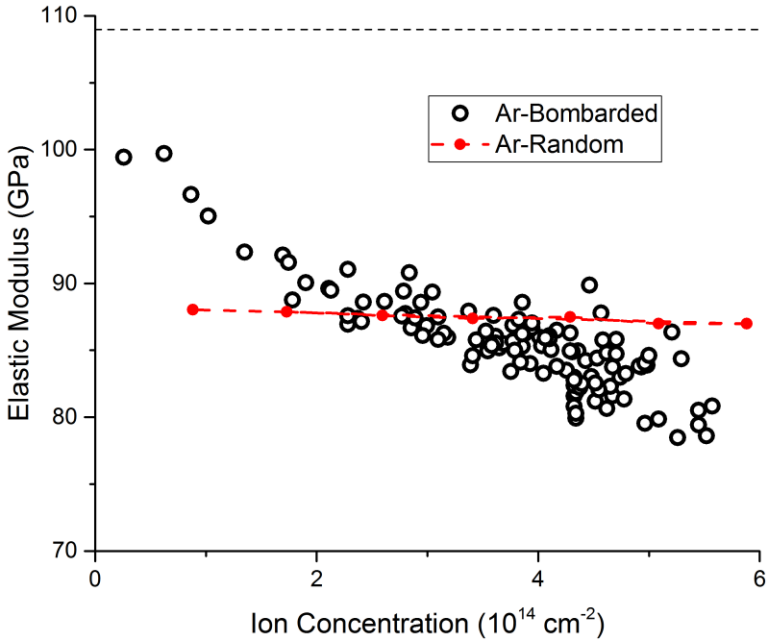

Figure 4.19: Dependence of the elastic modulus on the implanted ion concentration: **(black circles)** for Si bombarded by Ar^+ at normal incidence and 500 eV; **(red line)** for Ar randomly placed into the surface. The gray line at the top of the plot indicates the modulus of undamaged Si for reference.

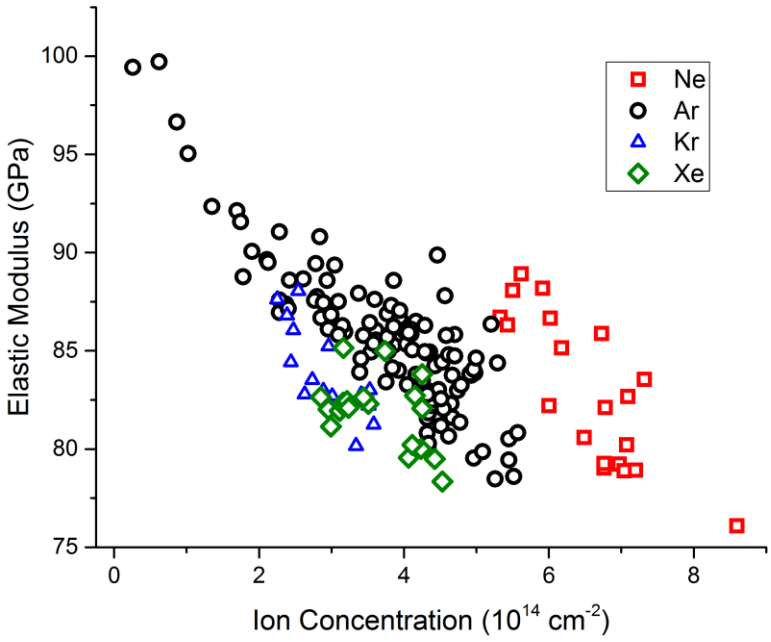

Figure 4.20: Dependence of the elastic modulus on the implanted ion concentration for Si bombarded at normal incidence and 500 eV, for each of Ne^+, Ar^+, Kr^+, and Xe^+.

Finally, the difference in the elastic modulus measured for Si implanted with different ion species is shown in **Figure 4.20**. Compared to the measurements for Ar-bombarded surfaces, the elastic modulus for Kr^+ and Xe^+ implantation is somewhat lower, although fairly similar to that for Ar^+ implantation. This is within expectations, since both of these ion species are larger than Ar and thus exert a greater repulsive force on nearby Si atoms. On the other hand, the elastic modulus for Ne-implanted Si has only been calculated for higher implanted ion concentrations than for the other species. At these high concentrations, the modulus is measured to be about the same, on average, as for Ar-implanted Si at lower implanted concentrations. While additional calculations still need to be done, it is reasonable to expect from the existing trends that Ne-implanted Si will have a higher elastic modulus at the lower implantation levels compared to the heavier ion species. This would be in line with expectations, since Ne is the smallest atom out of all species studied here.

4.5 Implications for multiscale modeling of Si nanopatterning

4.5.1 Relevance of implanted ion clustering to other mechanisms of nanopattern formation

As noted in **Chapter 2**, predictions of the critical incidence angle for pattern formation using models derived from MD data tend to underestimate the experimentally-measured value by ~10°. This problem is not limited to only atomistic computational models. The continuum model by Norris and coworkers [16], which derives all model parameters from MD simulations of single-ion impacts and a few material properties, has a similar underprediction as shown by **Figure 4.21**.

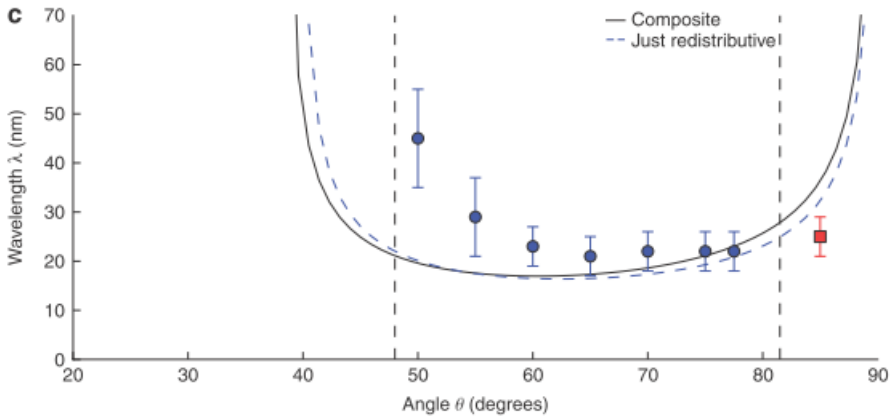

Figure 4.21: Comparison of predicted ripple wavelengths (lines) to experimental data (circles, squares) [90] based on the continuum model of Norris et al. with MD-derived model parameters [16]. The experimental critical angle is 48°, while the model predicts ripple formation at angles of 40° or slightly below.

To address this limitation in existing models, the proposed cluster degassing mechanism could be incorporated to function as a "stabilizing force" which inhibits pattern formation. By acting in conjunction with other mechanisms already contained in those models, the degassing mechanism could lead to a shift in the predicted critical transition angle to a higher value, bringing the prediction in line with experimental results. Further detailed analysis is needed to develop a suitable model for either continuum or kinetic Monte Carlo methods, making this a potentially-fruitful area of future work.

For continuum models, the key angle-dependent parameter is the cluster size and spatial distributions as well as the total implantation rate, while the actual surface modification effect from degassing events is insensitive to the incidence angle directly. Since models thus far have relied on single-impact events [8,16] or ion-induced modifications of the surface properties [33], this represents a new challenge for continuum approaches. On the other hand, for a kMC approach the implementation seems to be straightforward, but a detailed understanding of the tendency of implanted ions to join clusters, beyond simple random implantation into the surface, remains a key area of study if such a mechanism is to be implemented.

4.5.2 Importance of ion-induced stresses and clustering effects on "hydrodynamic" modeling paradigm

The central feature of the "hydrodynamic" models for ion beam nanopatterning is the depth-dependent distribution of ion-induced stress within the surface. The models presented in the literature thus far [31–33] have assumed that the shear stress depth profile has a linear form, is greatest at the very surface, and decreases throughout the amorphous region down to the amorphous/crystalline (a-c) interface. A second assumption, closely related, is that the stress distribution is identical to the distribution at normal incidence after a simple rotation, allowing for a simple rotation matrix to be used in the mathematics rather than a complex functional form. The results thus far have been generally quite good, although dependence on fitted parameters [36] and an inability to predict the formation of grazing-incidence ripple rotation remain outstanding issues.

The stress distribution from the MD simulations presented above generally support these assumptions. The stress dependence on depth indeed follows a general linearly-decreasing trend in each case, and the zero-stress depth decreases with incidence angle as would be expected for a simple rotation of the normal incidence profile. However, there are some incongruities to which attentions should be given. One issue is the mismatch in predicted magnitudes of the shear stress and its derivative with respect to depth. For normal incidence, the results of Moreno-Barrado and coworkers [33] indicate a change in the shear stress of around -800 MPa over ~2.5 nm depth, whereas the results in the present work show an average change in the stress of around -600 MPa over ~9 nm depth. While some of the difference may be due to differences in the ion species and energy (300 eV Xe^+ in [33] versus 500 eV Ar^+ in this thesis), it seems unlikely that this alone would be enough to account for the massive difference in slope and depth, since the change in elastic modulus due to each species in **Figure 4.20** is not nearly so drastic. A possible explanation could

be the difference in potentials (Tersoff in [33] versus S-W in this thesis). The influence of periodic boundary conditions is also a potential source of discrepancy, as the simulation size used in the previous work is only 5×5 nm^2 compared to the 7×7 nm^2 used in this work.

Another discrepancy between the present work and previous literature is that the rotation of the stress profile is not through the same angle as the beam incidence angle, as assumed in previous models. Note that the zero-stress depth for normal incidence (**Figure 4.15**) is around 9 nm, while for 60° incidence the zero-stress depth is around 5.5 nm. If the stress was simply rotated by $\cos(60°)$, the expected value would instead be 4.5 nm. This difference is likely attributable to the lateral spreading range of the incident ions, but must be accounted for in an accurate model of the angle-dependent surface stress distribution.

Finally, it is worth revisiting the points made previously about the potential effect of clusters on the local surface stress distribution. The large point-to-point variations in surface stress, particularly for low incidence angles (**Figures 4.15-4.17**) could have significant effects on the *local* surface evolution due to ion-induced stress, meaning that the morphology, at least in its early stages, would follow a quite *nonlinear* evolution contrary to the expectation of most existing theoretical models. If these localized stress variations are attributable to the presence of implanted ion clusters, significant future work must be dedicated to understanding the connection between the clusters, the resulting stresses, and the resulting impact on the surface morphology.

4.5.3 Additional implications of clustering phenomena

The formation of clusters beneath the surface, as previously mentioned, can be considered as a type of phase formation, allowing the ion/Si system to be treated as a multicomponent system. In this respect, the gas clusters observed in these simulations bear some resemblance to those formed in

GaSb as seen in **Chapter 3**. On the basis of this similarity, a few comments can be made with relevance to GaSb and other III-V systems under ion irradiation:

- Recalling that the formation of Sb protoclusters could not be explained by thermodynamic effects, it may be worth considering that a purely-kinetic process could lead to the accumulation of these clusters. Such a mechanism would account for the fact that the protoclusters are not formed from a single ion impact but in fact result from numerous cumulative impacts, analogously to the formation of the ion clusters discussed in this chapter. However, an understanding of the different natures of bonding between Ga and Sb would be required to explain why Ga clusters do not form by the same mechanism, in this case.
- An additional consideration drawn from ion clustering observations is the possibility to study the behavior of the larger Sb clusters (i.e. those formed by phase separation) as they are exposed to vacuum at the very surface. While degassing would not be expected since Sb is solid at room temperature, other interesting behaviors may be observable such as surface monolayer reconstruction [141].

In any case, the implanted ion clustering observed in the present chapter should provide insight and inspiration for the study of similar mechanisms in other, more complex material systems.

Chapter 5: Conclusions and future work

Computational techniques to characterize the ion-surface interaction mechanisms leading to nanopatterning are a critical need to advance physical understanding surface modification and synthesis with ion beams. The results from atomistic simulations presented in **Chapters 3 and 4** have demonstrated that molecular dynamics can be used at large computational scales to provide a wealth of detailed information about how incident ions can drive surface evolution. What remains to be done is to connect these findings to multiscale theoretical and computational models of ion beam nanopatterning, in order to develop models that can not only explain nanopattern formation, but which can ultimately predict the existence and characteristics of nanopatterns for new material combinations and experimental parameter variations.

It should be noted especially that the results presented in this thesis could not have been obtained from the BCA codes which have seen wide acceptance in the ion beam research community. In order to achieve the high efficiency responsible for their popularity, the BCA codes currently available are unable to provide information about structural changes, compositional phase formation, or the localized variations in the interatomic bonding that plays a critical role in governing the ion-surface interactions. Thus, the present work also demonstrates that MD techniques not only still have a place in the modern world of ion-surface modeling, but in fact that this place is already quite large and in fact must grow even larger to adequately consider the complex nanomaterials which increasingly draw the attention of the ion beam community.

5.1 Conclusions from massive-scale molecular dynamics simulations of GaSb under ion irradiation

MD simulations of a surface with an altered compositional depth profile have demonstrated that a lateral compositional variation can arise due to phase separation of enriched components. This

provides the much-needed connection between experimental characterization of those depth profiles [30] and theoretical models of ion beam nanopatterning on the same surfaces [6,7,23]. This has been done by showing for the first time that an ion-induced lateral compositional gradient can in fact induce a lateral variation which can, potentially, lead to the emergence of pattern-forming surface instabilities. This represents a significant step towards developing a predictive model of ion beam nanopatterning which correctly describes the core mechanisms leading to pattern formation. However, this is still only a single large step, and key knowledge gaps remain open, such as understanding how the compositional depth profile is formed in the first place and how its form is maintained over time.

Further large-scale MD studies have been done to simulate the evolution of GaSb(110) from its initial crystalline state up to an experimentally-relevant ion fluence approaching 10^{16} cm^{-2}. These results have shown that the prompt effects from many ion impacts, even in the absence of significant contributions from diffusional or other "gradual" mechanisms, will lead to compositional changes in the surface. Specifically, the emergence of Sb "protoclusters" surrounded by partial Ga shells was observed, which could potentially provide the "seeds" for the evolution and persistence of the compositional depth profile.

These results bring serious questions against the existing linear continuum models which have previously been used to explain pattern formation by ion beams at GaSb and other compound surfaces. In particular, the complex compositional evolution presents a complex 3D-spatial and temporal problem which is not adequately treated by the "2+1D" linear models, which are unable to consider both the complex compositional depth profile and the localized compositional dependence of the key surface properties on which those models depend. At this point in time, the initiative for modeling of ion beam nanopatterning appears to lie with computational efforts that have already begun to address these issues.

5.2 Conclusions from high-fluence molecular dynamics simulations of noble gas ion implantation into Si

Ion implantation into Si has been simulated with MD for a variety of ion species, incidence angles, and energies up to cumulative fluences of $\geq 3 \times 10^{15}$ cm^{-2}. This broad parameter set by itself already represents a several-times increase in that already explored by previous works [44,48]. These simulations also mark the first time in the literature of ion beam nanopatterning that the formation and behavior of implanted ion clusters has received substantial attention from a modeling perspective, although the formation of clusters had been observed three decades ago experimentally [100,127] and is a critical area of investigation in other fields involving ion-surface interactions [142,143]. From these results, a cluster degassing mechanism has been described and characterized with respect to the simulated parameter set, which can be responsible for the suppression of pattern formation for low angles of ion beam incidence. This pattern-inhibiting mechanism could provide corrections for underprediction of the critical incidence angle for ripple formation in previous models [16,78], and may also provide an explanation for the experimental difficulties in attempting to pattern Si with Ne ion beams.

In addition to this, preliminary investigations of the ion-induced stress distribution in the Si surface have been carried out, which will provide valuable insight to models of nanopattern formation which rely on these stresses. Early assessments of the shear stress depth profiles as well as the elastic modulus of the ion-damaged Si surface have indicated that the presence of implanted ion clusters plays a key role in determining the surface mechanical properties. While this bears further study before any strong conclusions can be made, it is worth noting that the effect of the implanted ion clusters is intrinsically a highly-localized one, and in this case a model describing that effect may be nonlinear by its very nature, in contrast to the linearized models which are usually preferred.

5.3 Proposed future work

There certainly remains significant parameter space which can still be covered as direct continuation of the work presented here. For example, the simulations already carried out for GaSb in **Chapter 3** could be extended to consider other III-V semiconductors, where the pattern formation is known vary from one material combination to the next [29]. However, since the ultimate aim of the MD simulations is to play a key role in the overall development of multiscale models which can predict pattern formation and characteristics, it makes sense that the primary direction of future work based on these results should be directed towards development of such a model.

Already, the framework for a predictive multiscale computational model exists in the form of the hybrid MD/kMC CFTM code discussed in **Chapter 2**. In fact, the design of CFTM is intended to be easily extensible to incorporate additional mechanisms, and in some cases a precedent exists in the literature for the design of a kMC treatment for mechanisms already indicated by the MD simulation results. Thus, to conclude this thesis a few potential additions to CFTM are discussed below based on the key observations from the MD work.

A simplified implementation of a multicomponent surface in CFTM could consist of adding a "component" or "element" variable for every position in the height map. However, to consider the fully three-dimensional nature of the surface composition with this approach, the height map would have to be converted into a three-dimensional representation. Within the surface, the phase separation can be treated by assessing the local bonding state of an atom, e.g. an atom in the subsurface of type A would be characterized in terms of the number of A and B neighbors, with a mix of both being unstable. Subsurface point defect generation and diffusion has already seen a kMC implementation [75] which could be readily adapted, with the crater function being expanded

to include information about defect generation. A potential downside to this approach would be the magnitude increase in computational complexity and thus the time required to run a simulation with CFTM, due to the additional third dimension.

The ion implantation and cluster formation might be less computationally taxing to implement if handled with care. Instead of a complete third dimension, implanted ions can be denoted by the (x, y) grid position under which they fall along with their depth beneath the surface. Clusters could be defined in the code in a few different ways, such as giving all implanted ions in a cluster a pointer variable indicating their membership in that cluster. Then, when one ion in a cluster is exposed to vacuum by the surface erosion, all ions in the cluster can be removed from the simulation to represent a degassing event. Beyond this, modeling the mass flow into the void left after degassing represents a challenge, and the nature of this mass inflow likely necessitates further detailed study of the MD simulation results.

For either of these cases, a core need to advance the model would be a significant amount of additional crater functions. For multicomponent modeling, the need is obvious as the surface composition must be varied in a fully-3D sense, although the necessary parameter space can be reduced through careful application of the knowledge gained from MD and experimental works (for example, surfaces with > 50% Sb might be safe to neglect, at least initially). On the other hand, if ion implantation is considered, a few different parameters with respect to the implanted ions should be considered. The local concentration of the implanted species should be an important variable, particularly since eventually the sputtering yield of implanted species must become significant as the ion concentration approaches a steady-state value. Additionally, the effect of impacts near and far from a subsurface cluster can be expected to differ significantly, introducing another parameter to vary.

It should be noted, in the interest of full consideration, that it is very possible for the number of craters, or the number of parameters for which those craters are parameterized, could very well reach large values impractical for use with a kMC model such as CFTM. If this should become the case, then some new approach or paradigm for modeling must be sought out. However, speculation as to the nature of this hypothetical other model is an entire subject on its own, and as such is well beyond the scope of the present work.

References

[1] M. Navez, C. Sella, and D. Chaperot, C. R. Hebd. Seances Acad. Sci. **254**, 240 (1962).

[2] R. L. Cunningham, P. Haymann, C. Lecomte, W. J. Moore, and J. J. Trillat, J. Appl. Phys. **839**, 839 (1960).

[3] U. Valbusa, C. Boragno, and F. B. De Mongeot, J. Phys. Condens. Matter **14**, 8153 (2002).

[4] S. Facsko, T. Dekorsy, C. Koerdt, C. Trappe, H. Kurz, A. Vogt, and H. L. Hartnagel, Science **285**, 1551 (1999).

[5] G. Ozaydin, A. S. Özcan, Y. Wang, K. F. Ludwig, H. Zhou, R. L. Headrick, and D. P. Siddons, Appl. Phys. Lett. **87**, 163104 (2005).

[6] R. M. Bradley and P. D. Shipman, Appl. Surf. Sci. **258**, 4161 (2012).

[7] S. A. Norris, J. Appl. Phys. **114**, 204303 (2013).

[8] R. M. Bradley and J. M. E. Harper, J. Vac. Sci. Technol. A **6**, 2390 (1988).

[9] D. Chowdhury, D. Ghose, and B. Satpati, Mater. Sci. Eng. B **179**, 1 (2014).

[10] P. Sigmund, J. Mater. Sci. **8**, 1545 (1973).

[11] W. W. Mullins, J. Appl. Phys. **28**, 333 (1957).

[12] G. Carter and V. Vishnyakov, Phys. Rev. B **54**, 17647 (1996).

[13] B. Davidovitch, M. J. Aziz, and M. P. Brenner, Phys. Rev. B **76**, 205420 (2007).

[14] N. Kalyanasundaram, M. Ghazisaeidi, J. B. Freund, and H. T. Johnson, Appl. Phys. Lett. **92**, 131909 (2008).

[15] S. A. Norris, M. P. Brenner, and M. J. Aziz, J. Phys. Condens. Matter **21**, 224017 (2009).

[16] S. A. Norris, J. Samela, L. Bukonte, M. Backman, F. Djurabekova, K. Nordlund, C. S. Madi, M. P. Brenner, and M. J. Aziz, Nat. Commun. **2**, 276 (2011).

[17] R. Gago, L. Vázquez, R. Cuerno, M. Varela, C. Ballesteros, and J. M. Albella, Appl. Phys. Lett. **78**, 3316 (2001).

[18] S. Facsko, T. Bobek, T. Dekorsy, and H. Kurz, Phys. Status Solidi B **224**, 537 (2001).

[19] M. Castro, R. Cuerno, L. Vázquez, and R. Gago, Phys. Rev. Lett. **94**, 16102 (2005).

[20] V. B. Shenoy, W. L. Chan, and E. Chason, Phys. Rev. Lett. **98**, 256101 (2007).

[21] R. M. Bradley and P. D. Shipman, Phys. Rev. Lett. **105**, 145501 (2010).

[22] P. D. Shipman and R. M. Bradley, Phys. Rev. B **84**, 85420 (2011).

[23] S. Le Roy, E. Søndergård, I. S. Nerbø, M. Kildemo, and M. Plapp, Phys. Rev. B **81**, 161401(R) (2010).

[24] R. M. Bradley, Phys. Rev. B **85**, 115419 (2012).

[25] J. Zhou and M. Lu, Phys. Rev. B **82**, 125404 (2010).

[26] R. M. Bradley, Phys. Rev. B **87**, 205408 (2013).

[27] R. M. Bradley, Phys. Rev. B **83**, 195410 (2011).

[28] R. M. Bradley, J. Appl. Phys. **119**, 134305 (2016).

[29] O. El-Atwani, S. A. Norris, K. Ludwig, S. Gonderman, and J. P. Allain, Sci. Rep. **5**, 18207 (2015).

[30] B. J. Holybee, Novel Analytical Method for Investigating Compositional Driven Ion-Induced Nanopatterning of Multicomponent Materials, University of Illinois at Urbana-Champaign, 2016.

[31] M. Castro and R. Cuerno, Appl. Surf. Sci. **258**, 4171 (2012).

[32] S. A. Norris, Phys. Rev. B **86**, 235405 (2012).

[33] A. Moreno-Barrado, M. Castro, R. Gago, L. Vázquez, J. Muñoz-García, A. Redondo-Cubero, B. Galiana, C. Ballesteros, and R. Cuerno, Phys. Rev. B **91**, 155303 (2015).

[34] L. Pelaz, L. A. Marqús, and J. Barbolla, J. Appl. Phys. **96**, 5947 (2004).

[35] T. Kumar, A. Kumar, D. C. Agarwal, N. P. Lalla, and D. Kanjilal, Nanoscale Res. Lett. **8**, 336 (2013).

[36] S. A. Norris, Phys. Rev. B **85**, 155325 (2012).

[37] B. J. Alder and T. E. Wainwright, J. Chem. Phys. **31**, 459 (1959).

[38] T. Diaz de la Rubia and G. Gilmer, Phys. Rev. Lett. **74**, 2507 (1995).

[39] M.-J. Caturla, T. Díaz de la Rubia, L. A. Marqués, and G. H. Gilmer, Phys. Rev. B **54**, 16683 (1996).

[40] M. Kitabatake and J. E. Greene, Thin Solid Films **272**, 271 (1996).

[41] R. Smith, D. E. Harrison Jr., and B. J. Garrison, Phys. Rev. B **40**, 93 (1989).

[42] M. E. Barone and D. B. Graves, Plasma Sources Sci. Technol. **5**, 187 (1996).

[43] J. E. Rubio, L. A. Marques, L. Pelaz, M. Jaraiz, and J. Barbolla, Nucl. Inst. Methods Phys. Res. B **112**, 156 (1996).

[44] M. C. Moore, N. Kalyanasundaram, J. B. Freund, and H. T. Johnson, Nucl. Inst. Methods Phys. Res. B **225**, 241 (2004).

[45] N. Kalyanasundaram, J. B. Freund, and H. T. Johnson, J. Eng. Mater. Technol. **127**, 457 (2005).

[46] N. Kalyanasundaram, M. C. Moore, J. B. Freund, and H. T. Johnson, Acta Mater. **54**, 483 (2006).

[47] N. Kalyanasundaram, M. Wood, J. B. Freund, and H. T. Johnson, Mech. Res. Commun. **35**, 50 (2008).

[48] A. Moreno-Barrado, R. Gago, A. Redondo-Cubero, L. Vázquez, J. Muñoz-García, R. Cuerno, K. Lorenz, and M. Castro, Europhys. Lett. **109**, 48003 (2015).

[49] N. G. Stoffel, J. Vac. Sci. Technol. B **10**, 651 (1992).

[50] A. Kuronen, J. Tarus, and K. Nordlund, Nucl. Instr. Meth. Phys. Res. B **153**, 209 (1999).

[51] K. Gärtner, Nucl. Inst. Methods Phys. Res. B **268**, 149 (2010).

[52] E. Despiau-Pujo, P. Chabert, and D. B. Graves, J. Vac. Sci. Technol. A **26**, 274 (2008).

[53] E. Despiau-Pujo and P. Chabert, J. Vac. Sci. Technol. A **28**, 1105 (2010).

[54] S. A. Norris, J. Samela, M. Vestberg, K. Nordlund, and M. J. Aziz, Nucl. Inst. Methods Phys. Res. B **318**, 245 (2014).

[55] J. P. Biersack and L. G. Haggmark, Nucl. Instrum. Meth. **174**, 257 (1980).

[56] M. T. Robinson and I. M. Torrens, Phys. Rev. B **9**, 5008 (1974).

[57] J. P. Biersack and W. Eckstein, Appl. Phys. A **34**, 73 (1984).

[58] J. F. Ziegler, J. P. Biersack, and U. Littmark, *The Stopping and Range of Ions in Solids* (Press, Pergamon, New York, 1985).

[59] J. F. Ziegler, M. D. Ziegler, and J. P. Biersack, Nucl. Inst. Methods Phys. Res. B **268**, 1818 (2010).

[60] W. Möller and W. Eckstein, Nucl. Inst. Methods Phys. Res. B **2**, 814 (1984).

[61] A. Mutzke, R. Schneider, W. Eckstein, and R. Dohmen, (2011).

[62] W. Möller, Nucl. Inst. Methods Phys. Res. B **322**, 23 (2014).

[63] L. Bukonte, F. Djurabekova, J. Samela, K. Nordlund, S. A. Norris, and M. J. Aziz, Nucl. Inst. Methods Phys. Res. B **297**, 23 (2013).

[64] N. Kalyanasundaram, J. B. Freund, and H. T. Johnson, J. Phys. Condens. Matter **21**, 224018 (2009).

[65] H. Hofsäss, Appl. Phys. A **114**, 401 (2014).

[66] R. Cuerno, H. A. Makse, S. Tomassone, S. T. Harrington, and H. E. Stanley, Phys. Rev. Lett. **75**, 4464 (1995).

[67] A. K. Hartmann, R. Kree, U. Geyer, and M. Koelbel, Phys. Rev. B **65**, 193403 (2002).

[68] I. Koponen, M. Hautala, and O.-P. Sievänen, Phys. Rev. B **54**, 13502 (1996).

[69] I. Koponen, O.-P. Sievänen, M. Hautala, and M. Hakovirta, J. Appl. Phys. **82**, 6047 (1997).

[70] I. T. Koponen, M. Hautala, and O.-P. Sievänen, Phys. Rev. Lett. **78**, 2612 (1997).

[71] E. Chason, W. L. Chan, and M. S. Bharathi, Phys. Rev. B **74**, 224103 (2006).

[72] A. K. Hartmann, R. Kree, and T. Yasseri, J. Phys. Condens. Matter **21**, 224015 (2009).

[73] Y. Ishii, W. L. Chan, and E. Chason, Nucl. Inst. Methods Phys. Res. B **272**, 188 (2012).

[74] R. Kree, T. Yasseri, and A. K. Hartmann, Nucl. Inst. Methods Phys. Res. B **267**, 1403 (2009).

[75] B. Liedke, K. H. Heinig, and W. Möller, Nucl. Inst. Methods Phys. Res. B **316**, 56 (2013).

[76] Z. Yang, M. Lively, and J. P. Allain, Nucl. Inst. Methods Phys. Res. B **307**, 189 (2013).

[77] Z. Yang, Development of a Multiscale Atomistic Code to Investigate Self-Organized Pattern Formation Induced by Ion Irradiation, Purdue University, 2013.

[78] Z. Yang, M. A. Lively, and J. P. Allain, Phys. Rev. B **91**, 75427 (2015).

[79] S. E. Donnelly and R. C. Birtcher, Philos. Mag. A **79**, 133 (1999).

[80] G. Costantini, F. Buatier De Mongeot, C. Boragno, and U. Valbusa, Phys. Rev. Lett. **86**, 838 (2001).

[81] R. C. Birtcher, A. W. McCormick, P. M. Baldo, N. Toyoda, I. Yamada, and J. Matsuo, Nucl. Inst. Methods Phys. Res. B **206**, 851 (2003).

[82] M. P. Harrison and R. M. Bradley, Phys. Rev. B **89**, 245401 (2014).

[83] J. C. Perkinson, E. Anzenberg, M. J. Aziz, and K. F. Ludwig, Phys. Rev. B **89**, 115433 (2014).

[84] S. Plimpton, J. Comput. Phys. **117**, 1 (1995).

[85] G. Hou, The Development of a Dynamic Radiation-Surface Interaction Simulation Code, Purdue University, 2010.

[86] T. Basu, D. Datta, and T. Som, Nanoscale Res. Lett. **8**, 289 (2013).

[87] G. Ehrlich and F. G. Hudda, J. Chem. Phys. **44**, 1039 (1966).

[88] R. L. Schwoebel and E. J. Shipsey, J. Appl. Phys. **37**, 3682 (1966).

[89] R. L. Schwoebel, J. Appl. Phys. **40**, 614 (1969).

[90] C. S. Madi, H. Bola George, and M. J. Aziz, J. Phys. Condens. Matter **21**, 224010 (2009).

[91] C. S. Madi and M. J. Aziz, Appl. Surf. Sci. **258**, 4112 (2012).

[92] M. Castro, R. Gago, L. Vázquez, J. Muñoz-García, and R. Cuerno, Phys. Rev. B **86**, 214107 (2012).

[93] C. S. Madi, B. Davidovitch, H. B. George, S. A. Norris, M. P. Brenner, and M. J. Aziz, Phys. Rev. Lett. **101**, 10 (2008).

[94] M. Joe, C. Choi, B. Kahng, and J. S. Kim, Appl. Phys. Lett. **91**, 233115 (2007).

[95] M. Joe, J.-H. Kim, C. Choi, B. Kahng, and J.-S. Kim, J. Phys. Condens. Matter **21**, 224011

(2009).

[96] F. Frost, B. Ziberi, A. Schindler, and B. Rauschenbach, Appl. Phys. A **91**, 551 (2008).

[97] S. M. Yoon and J. S. Kim, J. Appl. Phys. **119**, 205301 (2016).

[98] R. M. Bradley, Phys. Rev. E **54**, 6149 (1996).

[99] M. Joe, C. Choi, B. Kahng, C. Y. Kwak, and J.-S. Kim, J. Korean Phys. Soc. **52**, 181 (2008).

[100] U. Bangert, P. J. Goodhew, C. Jeynes, and I. H. Wilson, J. Phys. D **19**, 589 (1986).

[101] S. A. Norris, 1 (2014).

[102] D. Chowdhury, D. Ghose, S. A. Mollick, B. Satpati, and S. R. Bhattacharyya, Phys. Status Solidi B **252**, 811 (2015).

[103] S. Facsko, T. Bobek, A. Stahl, H. Kurz, and T. Dekorsy, Phys. Rev. B **69**, 153412 (2004).

[104] O. El-Atwani, J. P. Allain, A. Cimaroli, and S. Ortoleva, J. Appl. Phys. **110**, (2011).

[105] O. El-Atwani, J. P. Allain, and A. Suslova, Appl. Phys. Lett. **101**, (2012).

[106] O. El-Atwani, J. P. Allain, and S. Ortoleva, Nucl. Inst. Methods Phys. Res. B **272**, 210 (2012).

[107] O. El-Atwani, S. Gonderman, and J. Paul Allain, J. Appl. Phys. **114**, (2013).

[108] R. Kelly, Surf. Interface Anal. **7**, 1 (1985).

[109] Y. Yuba, S. Hazama, and K. Gamo, Nucl. Inst. Methods Phys. Res. B **206**, 648 (2003).

[110] H. Bracht, S. P. Nicols, W. Walukiewicz, J. P. Silveira, F. Briones, and E. E. Haller, Nature **408**, 69 (2000).

[111] C. L. Mendes, B. Bode, G. H. Bauer, J. Enos, C. Beldica, and W. T. Kramer, Procedia Comput. Sci. **29**, 198 (2014).

[112] H. J. C. Berendsen, J. P. M. Postma, W. F. van Gunsteren, A. DiNola, and J. R. Haak, J. Chem. Phys. **81**, 3684 (1984).

[113] D. Powell, M. A. Migliorato, and A. G. Cullis, Phys. Rev. B **75**, 115202 (2007).

[114] K. Albe, K. Nordlund, J. Nord, and A. Kuronen, Phys. Rev. B **66**, 35205 (2002).

[115] J. Tersoff, Phys. Rev. B **37**, 6991 (1988).

[116] Y. P. Varshni, Chem. Phys. **342**, 297 (2007).

[117] C. S. Barrett, P. Cucka, and K. Haefner, Acta Crystallogr. **16**, 451 (1963).

[118] L. Brewer, *The Cohesive Energies of the Elements* (1971).

[119] A. Stukowski, Model. Simul. Mater. Sci. Eng. **18**, 15012 (2010).

[120] A. G. Perez-Bergquist, K. Sun, L. Wang, and Y. Zhang, J. Mater. Res. **24**, 2286 (2009).

[121] A. Chroneos and H. Bracht, J. Appl. Phys. **104**, 93714 (2008).

[122] H. A. Tahini, A. Chroneos, H. Bracht, S. T. Murphy, R. W. Grimes, and U. Schwingenschlögl, Appl. Phys. Lett. **103**, (2013).

[123] A. Chroneos, H. A. Tahini, U. Schwingenschlögl, and R. W. Grimes, J. Appl. Phys. **116**, (2014).

[124] W. Hauffe, Phys. Status Solidi A **35**, K93 (1976).

[125] R. M. Bradley and H. Hofsäss, J. Appl. Phys. **120**, 74302 (2016).

[126] H. Hofsäss, K. Zhang, and O. Bobes, J. Appl. Phys. **120**, 135308 (2016).

[127] G. N. A. van Veen, F. H. M. Sanders, J. Dieleman, A. van Veen, D. J. Oostra, and A. E. de Vries, Phys. Rev. Lett. **57**, 739 (1986).

[128] H. A. Filius, A. van Veen, K. R. Bijkerk, and J. H. Evans, Rad. Eff. Def. Solids **108**, 1 (1989).

[129] M. J. Baldwin and R. P. Doerner, J. Nucl. Mater. **404**, 165 (2010).

[130] O. El-Atwani, S. Ortoleva, A. Cimaroli, and J. P. Allain, Nanoscale Res. Lett. **6**, 403 (2011).

[131] O. El-Atwani, A. Suslova, A. Demasi, S. Gonderman, J. Fowler, M. El-Atwani, K. Ludwig, and J. Paul Allain, Appl. Phys. Lett. **101**, (2012).

[132] O. El-Atwani, S. Gonderman, A. Demasi, A. Suslova, J. Fowler, M. El-Atwani, K. Ludwig, and J. Paul Allain, J. Appl. Phys. **113**, (2013).

[133] N. Laegreid and G. K. Wehner, J. Appl. Phys. **32**, 365 (1961).

[134] P. C. Zalm, J. Appl. Phys. **54**, 2660 (1983).

[135] J. W. Coburn, H. F. Winters, and T. J. Chuang, J. Appl. Phys. **48**, 3532 (1977).

[136] J. M. E. Harper, J. J. Cuomo, P. A. Leary, G. M. Summa, H. R. Kaufman, and F. J. Bresnock, J. Electrochem. Soc. **128**, 1077 (1981).

[137] P. C. Zalm, L. J. Beckers, and F. H. M. Sanders, Nucl. Instrum. Meth. **209**–**210**, 561 (1983).

[138] F. H. Stillinger and T. A. Weber, Phys. Rev. B **31**, 5262 (1985).

[139] V. G. Molière, Z. Naturforschg. **2a**, 133 (1947).

[140] A. P. Thompson, S. J. Plimpton, and W. Mattson, J. Chem. Phys. **131**, 154107 (2009).

[141] N. S. Kaijaks, Ion-Scattering Spectroscopy of III – V Semiconductor Surfaces, University of Warwick, 2000.

[142] L. Hu, K. D. Hammond, B. D. Wirth, and D. Maroudas, Surf. Sci. **626**, L21 (2014).

[143] L. Hu, K. D. Hammond, B. D. Wirth, and D. Maroudas, J. Appl. Phys. **118**, (2015).